The Development and Verification of a Centrifugal Compressor Test Bench

by
Daniël Johannes Struwig

Dissertation presented for the degree of *Master of Science in the Faculty of Mechanical Engineering at Stellenbosch University*

Promotors:
Dr. S.J. van der Spuy
Prof. T.W. von Backsröm

April 2014

Declaration

By submitting this thesis electronically, I declare that the entirety of the work contained therein is my own, original work, that I am the sole author thereof (save to the extent explicitly otherwise stated), that reproduction and publication thereof by Stellenbosch University will not infringe any third party rights and that I have not previously in its entirety or in part submitted it for obtaining any qualification.

Date: .....

Abstract

The Development and Verification of a Centrifugal Compressor Test Bench

D.J. Struwig

Department of Mechanical and Mechatronics Engineering,
Stellenbosch University,
Private Bag X1, Matieland 7602, South Africa.

Thesis: MScEng (Mech)

April 2014

Turbomachinery plays an important role in the efficiency of power generation and combustion processes used in the automotive and aerospace industries. The potential for fulfilling future energy needs has been identified in both civilian and military applications, for example micro gas turbines (MGTs) used in unmanned aerial vehicles (UAVs). The goal of this thesis was to build a performance testing facility for small-scale centrifugal compressors, for use in MGTs. The objectives of this study were mainly achieved through experimental work. In addition to the experimental work, numerical simulations using computational fluid dynamics (CFD) software were performed to substantiate the experimental results. The project methodology followed the process whereby a compressor performance map is constructed from experimental data and compared to a map obtained from theoretical data. The test facility consists of a turbocharger fitted with an experimental compressor section. The turbocharger turbine is driven by unheated compressed air. Sensors, data acquisition and ancillary equipment required to perform performance test measurements, were obtained and installed on the test facility. Performance curves at three different rotational speeds were successfully obtained for the experimental compressor. When compared to the CFD results there was good qualitative agreement, although deviations in the results increased with rotational speed. In addition a second impeller design was tested which correlated well with the theoretical data.

Keywords: micro gas turbine, centrifugal compressor, test facility, compressed air, turbocharger, impeller, experimental, CFD.

Uittreksel

Die Ontwikkeling en Verifikasie van 'n Sentrifugale Kompressor Toetsbank

("The Development and Verification of a Centrifugal Compressor Test Bench")

D.J. Struwig

Departement Meganiese en Megatroniese Ingenieurswese,
Universiteit van Stellenbosch,
Privaatsak X1, Matieland 7602, Suid Afrika.

Tesis: MScIng (Meg)

April 2014

Turbomasjinerie speel 'n belangrike rol in die doeltreffendheid van kragopwekking en verbrandingsprosesse wat in die motor- en lugvaartbedryf gebruik word. Die potensiaal om in toekomstige energiebehoeftes te voorsien is in beide burgerlike en militêre toepassings uitgewys, byvoorbeeld mikrogasturbines (MGT's) wat in onbemande vliegtuie (OLV's) gebruik word. Die doel met hierdie tesis was om 'n prestasietoetsfasiliteit vir kleinskaalse sentrifugale kompressors te bou wat in MGT's gebruik kan word. Die doelstellings van hierdie studie is hoofsaaklik deur eksperimentele werk behaal. Daarbenewens is numeriese simulasies met gebruikmaking van sagteware vir berekeningsvloeidinamika (BVD) gedoen om die eksperimentele resultate te staaf. Die projekmetodologie volg die proses om 'n kompressorprestasiekaart uit eksperimentele data op te stel en dit te vergelyk met 'n kaart wat uit teoretiese data bekom is. Die toetsfasiliteit bestaan uit 'n turboaanjaer wat met 'n eksperimentele kompressordeel toegerus is. Die turboaanjaer se turbine word deur onverhitte druklug aangedryf. Sensors, dataverwerwing en bykomstige toerusting, wat benodig is om prestasietoetsmetings mee te doen, is bekom en op die toetsfasiliteit geïnstalleer. Prestasiekrommes is vervolgens by drie verskillende omwentelingsnelhede suksesvol met die eksperimentele kompressor bekom. In vergelyking met die BVD-resultate was daar goeie kwalitatiewe ooreenstemming, ofskoon afwykings in die resultate vergroot het namate die omwentelingspoed toegeneem het. Daarby is 'n tweede stuwerontwerp getoets wat goed met die teoretiese resultate korreleer.

Sleutelwoorde: mikrogasturbine, sentrifugale kompressor, toetsfasiliteit, druklug, turboaanjaer, stuwer, eksperimentele, BVD.

Acknowledgements

I would like to express my sincere gratitude to the following:

- To my Lord and Saviour, who by the Grace of His Holy Spirit, gave me the strength to complete my thesis. Through this tough journey my character was tested and moulded, however I emerged a person who's life has been changed for the better.
- To my wonderful parents, Hannes and Erwine Struwig who provided me with emotional and financial support and motivated me right to the very end. I will for ever be grateful for their love and support which they gave throughout the entire duration of my thesis.
- To my supervisors Dr. S.J. van der Spuy and Prof. T.W. von Backström for their guidance, endless support and perseverance.
- The CSIR, ARMSCOR and the SAAF for funding this thesis which is part of the Ballast project.
- Dr. Glen Snedden from the CSIR for his inputs.
- All the personnel from the workshop who assisted in the manufacturing and assembly of the test bench.
- Last but not least I would like to thank the following colleagues; Mr. Andrew de Wet, Mr. Bosman van der Merwe and Dr. Andrew Gill for their helpful advice and generous input.

Dedications

Hierdie tesis word opgedra aan my ouers; Hannes en Erwine Struwig. Ek is so dankbaar vir julle oneindige ondersteuning en liefde.

Contents

List of Figures

List of Tables

Nomenclature

Symbols

A	Area	$[\mathrm{m}^2]$
a	Sonic velocity	$[\mathrm{m/s}]$
B_{max}	Shannon-Nyquist sampling frequency	$[\mathrm{Hz}]$
b	Blade height	$[\mathrm{mm}]$
C_d	Coefficient of discharge	$[\ ]$
C_p	Specific heat at constant pressure	$[\mathrm{J/kg \cdot K}]$
c	Absolute velocity	$[\mathrm{m/s}]$
D	diameter of larger pipe	$[\mathrm{m}]$
d	diameter of smaller pipe	$[\mathrm{m}]$
F	Fluctuation of measured quantity	$[\%]$
f	Friction factor	$[\ ]$
f_s	Sampling frequency	$[\mathrm{Hz}]$
H	Head of compressor, actual or isentropic	$[\ ]$
h	Specific enthalpy	$[\mathrm{J/kg}]$
i	Sample number	$[\ ]$
j	Measurement number	$[\ ]$
K	Dynamic correction factor	$[\ ]$
L	Pipe length	$[\mathrm{m}]$
M	Mach number	$[\ ]$
m	Meridional length	$[\ ]$
	Experimental measurements	$[\ ]$
M_U	Rotational Mach number,U_2/a_{0t}	$[\ ]$
$\dot{m}$	Mass flow rate	$[\mathrm{kg/s}]$
N	Rotational speed	$[\mathrm{rpm}]$
n	Measurement samples	$[\ ]$
P	Power	$[\mathrm{W}]$
p	Pressure	$[\mathrm{Pa}]$
PR	Pressure ratio	$[\ ]$

R	Gas constant	$[\mathrm{J/kg \cdot K}]$
Re_{d}	Reynolds number (diameter)	[ ]
r	Radius	$[\mathrm{m}]$
Q	Flow rate	$[\mathrm{m^3/s}]$
S	Data sample	[ ]
$\langle S_{\bar{x}} \rangle$	Pooled standard deviation of the means of x	[ ]
s	Specific entropy	$[\mathrm{J/kg \cdot K}]$
T	Temperature	$[\mathrm{K}]$
$t_{99,99}$	Student's t distribution, 99 deg. freedom, 99% prob.	[ ]
U	Blade speed, ωr	$[\mathrm{m/s}]$
w	Relative velocity	$[\mathrm{m/s}]$
W	Specific work transfer	[ ]
x	Measured quantity	[ ]
$\langle \bar{x} \rangle$	Pooled mean of x	[ ]
y^+	Non-dimenional wall quantity	[ ]
y_{wall}	Wall cell width	$[\mathrm{m}]$
Z	Blade count	[ ]

Greek Symbols

α	Fluid relative flow angle	$[\mathrm{rad}]$
	Flow coefficient	[ ]
β	Relative flow angle	$[\mathrm{rad}]$
	Diameter ratio	[ ]
γ	Ratio of specific heats	[ ]
ϵ	Compressibility factor	[ ]
η	Efficiency	[ ]
θ	Blade camber angle	$[\mathrm{rad}]$
μ	Dynamic viscosity	$[\mathrm{kg/m \cdot s}]$
	Work Coefficient	[ ]
ν	Kinematic viscosity	$[\mathrm{m^2/s}]$
ρ	Density	$[\mathrm{kg/m^3}]$
σ	Slip factor	[ ]
ψ	Power factor	[ ]
ω	Rotational speed	$[\mathrm{rad/s}]$

Subscripts

0	Compressor inlet condition (impeller eye)

1	Impeller blade inlet condition (leading edge)
2	Impeller blade outlet condition (trailing edge)
3	Diffuser outlet outlet condition
4	Compressor outlet (pressure station)
5	Compressor outlet (temperature station)
amb	Ambient condition
bm	Bellmouth
c	Compressor
d	Discharge side
m	Machine
p	Probe condition
o	Output
t	Total (stagnation) thermodynamic condition
$t-t$	Total-to-total quantity
$t-s$	Total-to-static quantity
s	Static thermodynamic condition
	Suction side
	Sampling quantity
vo	Volute outlet quantity
x, y, z	Cartesian coordinates

Supercripts

$'$	Blade angle (as distinct from flow angle)
$\bar{}$	Average value
$\dot{}$	Time rate of change
$*$	Sonic/critical condition
	Isentropic condition

Acronyms

ANSI	American National Standards Institute
ARMSCOR	Armaments Corporation of South Africa
ASME	American Society of Mechanical Engineers
BEP	Best Efficiency Point
BS	British Standards
CAD	Computer Aided Design
CFD	Computational Fluid Dynamics

CFL	Courant-Friedrichs-Lewy
CPU	Central Processing Unit
cRIO	Compact Reconfigurable I/O
CSIR	Council for Scientific and Industrial Research
DAQ	Data Acquisition
DC	Direct Current
FNMB	Full Non-Matching Boundary
FPGA	Field Programmable Gate Array
GUI	Graphical User Interface
IAT	Institute of Advanced Tooling
ISO	International Standards Organisation
KKK	Kühnle, Kopp & Kausch
LFE	Laminar Flow Element
MGT	Micro Gas Turbine
NB	Nominal Bore
NMR	Nominal Measuring Range
PL	Part Load
PVC	Polyvinyl Chloride
RPD	Rapid Product Development
SAAF	South African Air Force
SAE	Society of Automotive Engineers
SM	Surge Margin
STL	Stereolithography
SwRI	Southwest Research Institute
TD	Turndown
UAV	Unmanned Aerial Vehicle
VI	Virtual Instrument

Chapter 1

Introduction

1.1 Background

Project BALLAST was created to conduct research in the field of turbomachinery and to increase the knowledge base and expertise in this field in South Africa. This also coincides with the growing trend of developing applications for micro gas turbines (MGTs), (Aus der Wiesche, 2012; Benini and Giacometti, 2007). This thesis was completed as part of project BALLAST which is funded by the South African Air Force (SAAF) through the Armaments Corporation of South Africa (ARMSCOR) and coordinated by the Council for Scientific and Industrial Research (CSIR). The BALLAST project is sub-divided into various sub-projects, each focussing on the development and testing of individual components and systems of a micro gas turbine. This thesis focusses on developing a performance test facility for small-scale centrifugal compressors, for use in micro gas turbines.

1.2 Motivation

There is a global trend to reduce carbon emissions and increase the efficiency of power generation processes while simultaneously having to cope with the demand for more power. The field of turbomachinery is playing an increasingly important role in achieving this goal, especially in the automotive and aerospace industry (Vick *et al.*, 2009). One of the applications in which turbomachinery is being applied, is that of micro gas turbines (Figure 1.1). These small gas turbines are widely considered to have the potential for fulfilling future energy needs (Aus der Wiesche, 2012).

The need for small scale gas turbines that produce less than 10 kW has gained interest in both civilian and military applications. These range from portable power generation, residential and small backup power or co-generation, marine power generation as well as propulsion for unmanned aerial vehicles

(UAV) (Vick *et al.*, 2009). Previous studies on small gas engines for UAV applications were stimulated by commercial developments as well as being a proven military concept during the Gulf War (Lobik, 1995). The propulsion needs of UAVs are usually met by positive displacement engines such as spark ignition, diesel and rotary engines. These engines are attractive in terms of cost, weight, low fuel consumption and high power-to-weight ratios than alternative methods such as batteries, hydrogen stored in cryogenic tanks or solar cells. In spite of all these attractive qualities these engines also have numerous drawbacks such as short service lives ($\pm$100 hrs), frequent tuning by specialist personnel, high noise and vibration levels as well as the inability to work at high altitudes and speeds, the latter being critical to UAV operation (Lobik, 1995; Vick *et al.*, 2009).

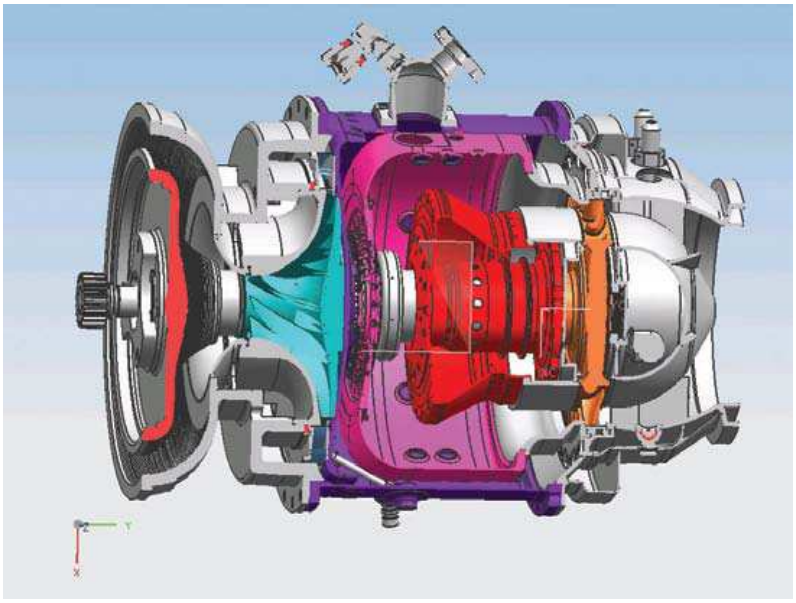

Figure 1.1: Example of a Micro Gas Turbine. (Chinese Academy of Sciences, 2012)

Compared to internal combustion engines, gas turbines offer the potential of increased reliability, longer engine life, less noise and vibration, reduced maintenance and superior compatibility with kerosene-based jet fuels. Initially, fitting UAVs with small gas turbines proved less promising as a result of aerodynamic and machine design problems inherent in the scaling down of gas turbine engines. As a result these engines are plagued by poor performance, such as low efficiency and thrust-to-weight ratios as well as high fuel consumption. Reasons for poor performance in small scale gas turbines include:

1. Reynolds number effects:

   Low Reynolds numbers are inherent at this small scale which results in higher coefficients of friction and therefore lower component efficiencies.

2. Larger relative tip clearances:

   The ratio of tip clearance to the span of the rotor blade is greater in small scale engines compared to full scale engines, therefore the tip losses are proportionally greater.

3. Lower cycle pressure ratio:

   An advantage of centrifugal compressors is that they achieve a higher pressure ratio per stage than an axial machine and are therefore favoured for MGT applications. The disadvantage is that centrifugal compressors have lower efficiencies as a result of friction and tip clearance losses. In order to circumvent this problem a combination of centrifugal (multi-stage), axial and centrifugal or purely axial compressors are required. To achieve a high pressure ratio in axial compressors the blade passage area of each consecutive stage decreases by decreasing the blade height. For the same reason reducing the size of a centrifugal compressor leads to extremely small blade heights especially at the impeller exit. Therefore low efficiencies at high pressure ratio's are unavoidable.

4. Lower peak cycle temperatures:

   Small gas engines cannot accommodate the cooling techniques used in full scale engines because of their small size, thus they are limited to lower peak cycle temperatures.

5. Difficulty of manufacturing:

   Turbine and compressor blades are complex structures of which the performance corresponds to tight tolerances during manufacturing. When scaling down to micro-sized blades, manufacturing becomes extremely difficult which subsequently increases the manufacturing cost.

6. Surface relative roughness effect:

   If the manufacturing processes of turbomachines are similar for both large and small machines then the relative surface roughness is greater and plays an increasing roll regarding losses occurring within the smaller machines. It is therefore important to take this effect into consideration when scaling down.

In spite of all these problems, the inability of internal combustion engines to operate at higher altitudes and speeds have motivated the further development of small gas turbine engines in UAVs (Lobik, 1995).

The ideal thermal efficiency, $\eta_{thermal}$ of a gas turbine engine is related to the pressure ratio and given by the following equation (Sonntag *et al.*, 1998):

$$\eta_{thermal} = 1 - \frac{1}{(p_2/p_1)^{\gamma-1/\gamma}} \tag{1.2.1}$$

where p_1 and p_2 is the pressure at the impeller in- and outlet respectively.

These values may range between 10 % and 20 % for the pressure ratio's under review but due to the non-ideal components in these engines the actual efficiencies are lower. From initial calculations Benini and Giacometti (2007) predicted a thermal efficiency of 12 % for the design of their micro gas turbine. The losses occur as a result of the high rotational speeds and high flow velocities relative to the size of the flow passages. These high rotational speeds also give rise to high frictional losses in mechanical parts. Compressor impellers in MGT's rotate at nominal speeds of about 100 000 rpm because of their small diameters. At these rotational speeds a small diameter gas turbine engine (62 mm to 68 mm) can only produce a relative pressure ratio of around 1.8 to 2. Thus in order to improve the efficiency of these micro gas turbines Ling *et al.* (2007) suggests that the pressure ratio of the compressor has to be increased while running at lower speeds, if possible. The total pressure ratio across the impeller can be related to the rotational speed by expressing it in terms of the impeller tip Mach number (Japikse and Baines, 1994):

$$PR_{t-t} = \left[1 + (\gamma - 1)\eta\mu M_U^2)\right]^{\gamma/(\gamma-1)} \tag{1.2.2}$$

It is therefore essential to increase the performance-to-rotational speed ratio by increasing the impeller diameter to maintain the tip speed while decreasing the rotational speed. This however poses a problem due to the inherent space constraints of micro gas turbines, which leaves the diffuser section as the only source of compromise (Ling *et al.*, 2007). From the evidence presented it is clear that research in optimising the performance of micro gas turbines is required. Test facilities with the capacity to record the detailed thermal performance would be of great value to engineers doing research on micro gas turbines or their various components (Aus der Wiesche, 2012; Smith, 2010).

1.3 Operation of a centrifugal compressor

With reference to textbooks by Aungier (2000) and Dixon (2005) a short description of the operation of a centrifugal compressor is given in this section.

The basic elements of a single centrifugal compressor stage include a rotating impeller to impart energy into the fluid, a vaned and/or vaneless diffuser to recover kinetic energy and a volute or scroll to collect and transfer the fluid to the downstream pipe system (see Figures 1.2a, 1.2b).

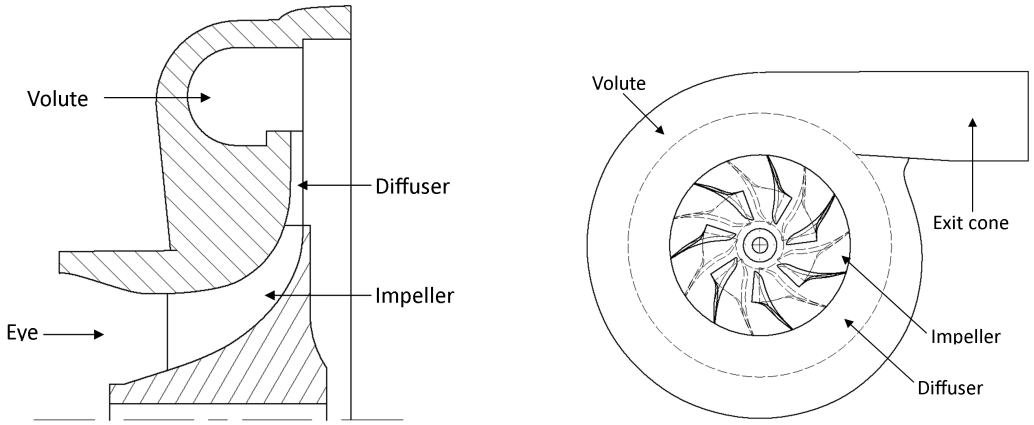

(a) Side view. (b) Front view.

Figure 1.2: Elements of a single stage centrifugal compressor. (adapted from (Aungier, 2000))

The flow through a centrifugal compressor is described by referring to the velocity vector diagrams illustrated in Figure 1.3. Air is sucked in through the inlet casing into the eye of the impeller in an axial direction with an absolute velocity of c_1, unless pre-whirl has been applied. Because of the rotor's rotation the fluid has a relative velocity vector of w_1 into the rotating impeller. The fluid then moves into the inducer section where energy is imparted to the fluid by means of centrifugal kinetic interaction. The fluid is "whirled" outwards, thereby increasing its angular momentum and at the same time the fluid static pressure, as the fluid moves from radius r_1 to r_2. The fluid then departs or exits the impeller with an absolute velocity c_2.

The blades at the outlet of the impeller are primarily radial, therefore it is convention to measure the outlet blade angle (β_2'), from the radial direction. For a purely radial impeller the blade outlet angle will be zero. A slip factor (σ) is introduced to account for the actual relative flow leaving the impeller. The slip factor is a measure of the fluid slip in the impeller of a compressor. As a result the theoretical tangential velocity $c_{\theta 2}'$ is reduced giving an actual tangential velocity $c_{\theta 2} = \sigma c_{\theta 2}'$. The relative velocity w_2 is at an angle β_2 because of slip. In the case of radial impellers when no slip occurs β_2' is zero and equal to the blade angle β_2, resulting in the tangential velocity equalling the absolute blade tip velocity U_2.

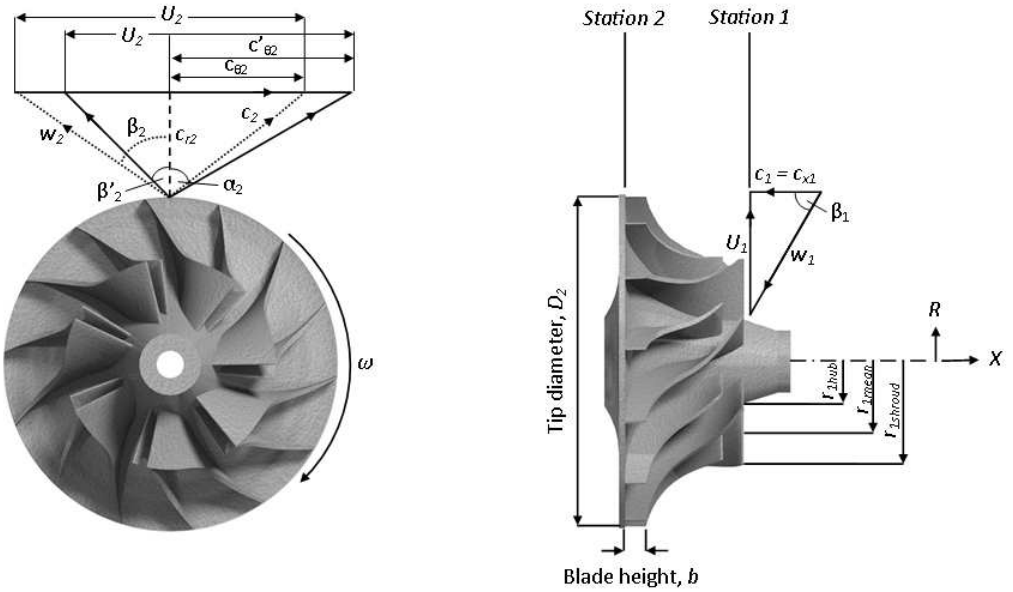

(a) Front view. (b) Side view.

Figure 1.3: Velocity diagrams of a centrifugal compressor impeller.

The performance of a centrifugal compressor is best described in terms of the thermodynamic properties of the working fluid by following the compression cycle on the Mollier $h - s$ chart (Figure 1.4).

At the inlet of the compressor the air is at atmospheric conditions with a total enthalpy of,

$$h_{t0} = h_{s0} + \frac{c_0^2}{2} \tag{1.3.1}$$

The air is accelerated to the impeller leading edge from c_0 to c_1, resulting in a drop of static pressure from p_{t0} to p_{s1}. Since no shaft work is being done and it is assumed that the flow is steady and adiabatic such that the stagnation enthalpy remains constant $h_{t0} = h_{t1}$,

$$h_{s0} + \frac{c_0^2}{2} = h_1 + \frac{c_1^2}{2} \tag{1.3.2}$$

where h_{s0} is the stagnation enthalpy and c_0 the absolute inlet velocity.

Work is done on the flow going through the impeller, resulting in a static pressure and temperature rise. This rise in static conditions is a result of the conservation of rothalpy across the impeller. Rothalpy is defined as,

$$I = h_{0rel} - \frac{1}{2}U^2 \tag{1.3.3}$$

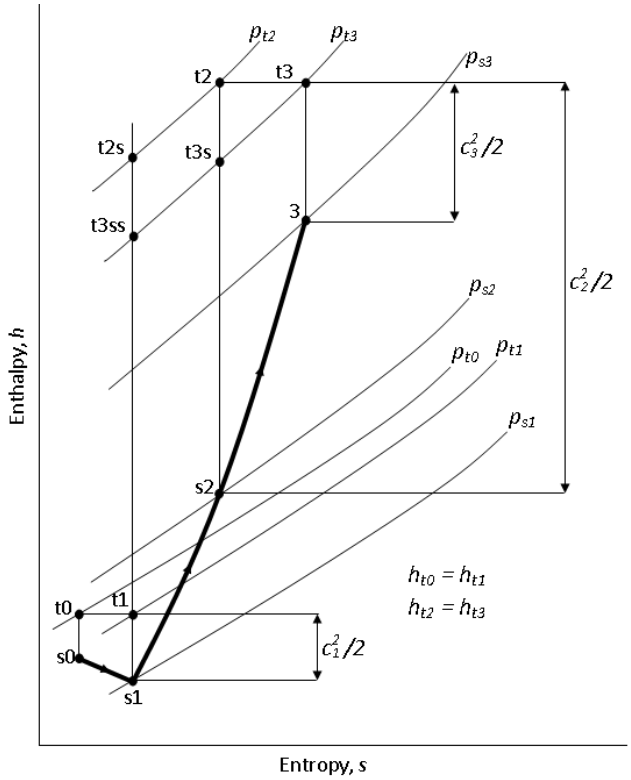

Figure 1.4: Mollier chart for a compression process (adapted from (Dixon, 2005)).

with

$$h_{0rel} = h + \frac{1}{2}w^2 \tag{1.3.4}$$

For the conservation of rothalpy $I_1 = I_2$ so that,

$$h_{s2} - h_{s1} = \frac{1}{2}\left(U_2^2 - U_1^2\right) + \frac{1}{2}\left(w_2^2 - w_1^2\right) \tag{1.3.5}$$

The specific work done on the fluid equals the rise in stagnation enthalpy and is also known as the Euler Work equation,

$$\begin{aligned} \Delta W_c &= h_{t2} - h_{t1} \\ &= U_2 c_{\theta 2} - U_1 c_{\theta 1} \end{aligned} \tag{1.3.6}$$

Now assuming purely axial flow at the inlet of the compressor (Figure 1.3b) so that the flow has zero whirl or angular momentum and $c_{\theta 1} = 0$ then Eqn. 1.3.6 reduces to,

$$\Delta W_c = U_2 c_{\theta 2} \tag{1.3.7}$$

At the impeller outlet the fluid velocity decreases from c_2 to c_3 as it flows through the diffuser, increasing the static pressure from p_{s2} to p_{s3}. This reduction in velocity is attributed to the increase in radius and cross-sectional flow area. Under the assumption of ideal frictionless flow though the diffuser, angular momentum is conserved such that $c_\theta = c_{\theta 2} r_2 / r$. The ratio of inlet to outlet diffuser velocities c_2/c_3 is then approximated by r_3/r_2 since the tangential velocity component c_θ is usually much higher than the radial component c_r. No work is performed on the fluid inside the diffuser, and assuming that the flow is adiabatic the stagnation enthalpy remains constant, $h_{t2} = h_{t3}$. The process from 2 to 3 is however irreversible (because of friction) with a total pressure loss of $p_{t2} - p_{t3}$.

With the flow described through the compressor in thermodynamic quantities, the performance can now be defined in terms of total-to-total isentropic efficiency η_{t-t} and pressure ratio PR_{t-t}. The isentropic efficiency across the compressor can be defined as the ratio of total isentropic enthalpy rise to the actual enthalpy rise at the same total pressure ratio. The isentropic efficiency is given in a more usable form,

$$\eta_{t-t} = \frac{C_p T_{t1} (T_{t3_{ss}} / T_{t1}) - 1}{U_2 c_{\theta 2}} \tag{1.3.8}$$

From isentropic relations the pressure ratio across the impeller is,

$$\frac{p_{t3}}{p_{t1}} = \left(\frac{T_{t3_{ss}}}{T_{t1}} \right)^{\gamma/(\gamma-1)} \tag{1.3.9}$$

Rearranging Eq. 1.3.8 and substituting into Eq. 1.3.9

$$PR_{t-t} = \left[1 + \frac{\eta_{t-t} U_2 c_{\theta 2}}{C_p T_{t1}} \right]^{\gamma/(\gamma-1)} \tag{1.3.10}$$

The performance of a centrifugal compressor is usually described in terms of the following parameters which have been normalised to the ambient temperature and pressure as well as the rpm,

- Corrected mass flow, $\dot{m}\sqrt{T_{t1}}/p_{t1}$,
- Corrected rotational speed, $N/\sqrt{T_{t1}}$,
- Total-to-total pressure ratio, PR_{t-t},

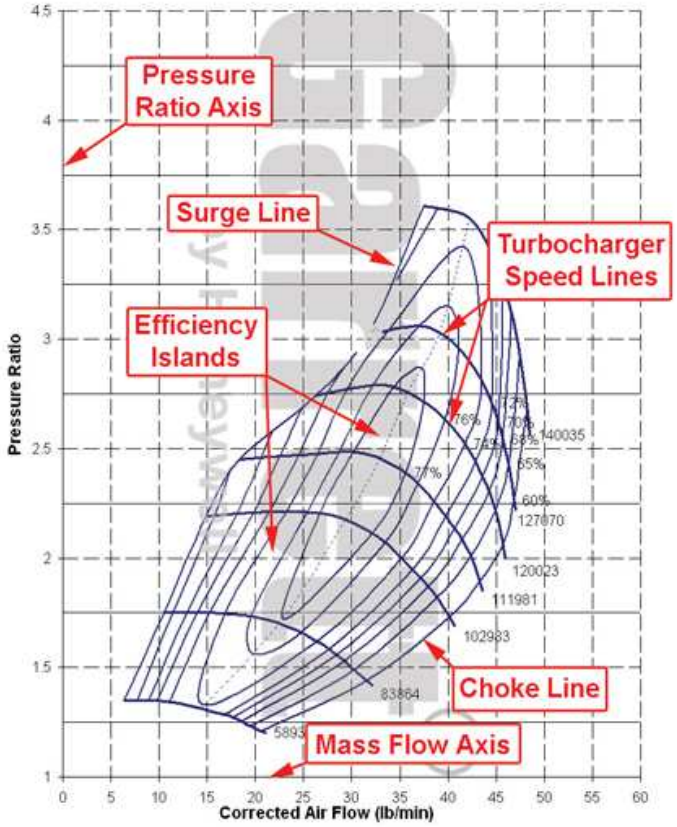

Figure 1.5: Typical compressor performance map of a Garrett turbocharger. (Garrett Turbochargers, 2012*a*)

- Total-to-total isentropic efficiency, η_{t-t}.

These parameters are contained in a series of curves of pressure ratio vs. mass flow on fixed speed intervals as shown for example in the manufacturers performance chart of a Garrett turbocharger in Figure 1.5. The various aspects of a centrifugal compressor performance map include the pressure ratio and mass flow axes, the constant speed lines, efficiency contours and lastly the surge and choke lines. As a matter of importance only surge and choke are discussed. A detailed description of these phenomena can be found in texts by Dixon (2005) and Sayers.

Surge is a highly dynamic phenomenon that occurs at low flow conditions which limits the safe operating region of a centrifugal compressor. Surge is often preceded by an aerodynamic effect known as rotating diffuser stall which induces aerodynamic vibrations and further limits a compressors' operating range. During surge the flow has been reduced below a critical point such that there is a sudden drop in discharge pressure which in turn will further reduce

the flow. At this point the flow field within the compressor has essentially collapsed and the compressor is said to be operating in an unstable region. When the discharge pressure has been reduced sufficiently, positive flow is re-established which results in an increase in flow and discharge pressure until the restricted mass flow is reached at which point the process is repeated.

In severe cases surge has the potential to cause failure of the compressor and it is with this thought in mind that determination of the surge point is conducted with extreme caution. A compressor limit of safe operation is indicated on a performance map by as solid line joining all the points at which surge occurs at various fixed speeds and is know as the surge line. Brun and Nored (2006) provide two methods for the determination of a compressors' safe operating range, namely compressor turndown and surge margin. Turndown is defined as a compressors' allowable operating range in terms of flow rate (Q) between the design point and surge line at any speed for a fixed pressure ratio and follows:

$$TD\% = 100.|\frac{(Q_{design} - Q_{surge})}{Q_{design}}|_{Head=constant} \tag{1.3.11}$$

The surge margin gives an indication of how close the compressor' design point is to surge at any fixed speed.

$$SM\% = 100.|\frac{(Q_{design} - Q_{surge})}{Q_{design}}|_{Speed=constant} \tag{1.3.12}$$

The process known as choke occurs when the flow is increased to such a point where a further increase is not possible. This is an indication that sonic conditions have been reached at some point within the compressor passages. These sonic conditions limit the maximum mass flow rate possible through the compressor. Choke can occur at three locations of a compressor namely; at the inlet, within the rotating impeller or within the diffuser passages.

1.4 Objectives

The objectives of this thesis will be achieved mainly through experimental work. In addition a numerical analysis of the compressor will be performed from which the results will be used to substantiate the experimental approach used in this project. Specifications received through email correspondence (Snedden, 2010) regarding the desired operating point of a centrifugal compressor for a typical micro gas turbine are shown in Table 1.1.

Table 1.1: CSIR centrifugal compressor specifications

Pressure ratio	4.72
Mass flow rate	0.325 kg/s
Rotational speed	121 000 rpm
Efficiency (Isentropic)	79.8 %
Efficiency (Polytropic)	83.6 %

These performance values must be achieved by a specific compressor configuration (the rotor and diffusing system) within the operational envelope of the test facility. The objectives of this project are summarised into the following subtasks:

1. Design and build a compressor test bench to accurately measure the performance of a centrifugal compressor.
    a) Acquire and install suitable measurement and data acquisition instrumentation.
    b) Characterise any auxiliary systems or components that will be used in the test bench, i.e. high pressure air supply, compressor inlet bellmouth etc.
    c) Formulate a suitable test procedure.
    d) Implement suitable methods of test automation.
2. Define the test envelope of the facility.
    a) Using analytical calculations.
    b) Using numerical simulations.
3. Create a compressor performance map from experimental and numerical data and study the correlation between the obtained results. A compressor map is constructed using the following performance parameters:
    a) Total-total pressure ratio, $[PR_{t-t}]$
    b) Total-static pressure ratio, $[PR_{t-s}]$
    c) Total-total efficiency, $[\eta_{t-t}]$
    d) Mass flow rate, $[\dot{m}]$
    e) Rotational speed, $[N]$
4. The performance of the test bench will also be assessed in terms of its operational use. Conclusions about the user friendliness, stability and repeatability of the measurements, safety as well as maximum operating range will be made.

The experimental approach followed in creating a compressor performance map involves the measurement and calculation of the performance parameters along a constant speed line from choke to surge. This is achieved by keeping the rotational speed fixed and varying the mass flow rate by restricting the flow at the outlet of the compressor. In order to determine the performance parameters the following values are measured at their respective locations:

- Static pressure:
    1. Inlet of the impeller.
    2. Outlet of the impeller.
    3. Outlet of the diffuser.
    4. Outlet of the volute exit cone.
- Differential pressure:
    1. Across the plane of the flow measuring device at the suction side of the compressor.
- Total temperature:
    1. Before the flow measuring device.
    2. Outlet of the volute exit cone.
- Rotational speed of the turbocharger at the inlet of the compressor eye.

The numerical approach follows a similar strategy, where the performance map is created by performing simulations along a constant speed line at various mass flow rates between choke and surge.

Chapter 2

Literature Study

2.1 Centrifugal compressor test facilities

The actual conditions at which micro gas turbines operate are difficult to replicate since the operating environment is not as ideal as that found in research or production facilities. As a result measurement uncertainties play an important role in determining the correct performance. Brun and Nored (2006) state that when the basic rules of test procedures and standards are violated, the uncertainties pertaining to the performance of these turbomachines can be unacceptably high.

Brun and Nored (2006) have written a guideline in which they give suggested best practices for testing gas turbines and centrifugal compressors. They also pay special attention to calculating test uncertainties in order to determine the quality of the tests. Their guideline serves as a reference for the testing of turbomachines in which the controlled factory environment differs from that of actual operating conditions. Guidelines such as the one presented by Brun and Nored (2006) as well as studies by individuals such as Lobik (1995); Smith (2010) etc. refer to performance test codes from standards organisations such as the International Standards Orginisation (ISO), Society of Automotive Engineers (SAE) and American Association of Mechanical Engineers (ASME). These performance test codes are written to provide test procedures that will ensure high levels of accuracy. The ASME test codes provide guiding principles in terms of planning, the type of tests and the instrumentation to be used to name a few. The test codes also go into detail in describing the instrumentation and methods of measurement for various test facility configurations. Methods of computation and sample calculations of different test types are also presented in the test codes.

In the process of developing a test facility for a centrifugal compressor various types of test facilities were investigated. From the test facilities presented

in the literature it was found that the configurations were influenced by; the type of test, impeller size and mode of drive. Of these mentioned, the mode of drive has probably the most significant impact on the configuration of the test facility. From literature three methods for driving the compressor were identified;

1. Driven by electric motor.
2. Driven as a complete micro gas turbine.
3. Driven as a complete turbocharger unit.

Driven by electric motor Test benches used by Lim *et al.* (2011) and Hagelstein *et al.* (2000) both utilised electric motors to drive the compressor. The motors used by Lim *et al.* and Hagelstein *et al.* was a high-speed induction motor rated for 125 kW at 30 000 rpm and a 1.35 MW DC motor at 1800 rpm respectively. Hagelstein *et al.*'s motor was coupled to a gearbox with a ratio of 1:16.2. Although Lim *et al.* and Hagelstein *et al.* both used electric motors to drive their compressors, they performed different type of tests.

Lim *et al.* specifically designed a test bench to investigate a novel method for controlling compressor surge. They present an innovative method whereby the impeller tip clearance is axially actuated using active magnetic bearings in order to control the onset of surge. The compressor surge test facility consisted of three sections, the driver (induction motor), driver equipment and supporting system (piping and motor accessories). The motor was directly coupled to the compressor and is controlled with a variable frequency drive. Inlet air was taken from the atmosphere and filtered upstream of the compressor inlet to provide clean air.

The scale of the installation is reflected in the size of the compressor. The length of the exhaust piping stretches for 7 m which then returns towards the inlet. Pressure, flow and temperature measurements were acquired along the length of the inlet and exhaust piping. In addition high-bandwidth Kulite pressure transducers were used to measure time dependent pressure distributions to provide insight into the transient effects of surge. Data acquisition was performed using National Instruments™ LabVIEW™ software and high-speed data acquisition and signal processing cards.

The test facility used by Hagelstein *et al.* (Figure 2.1) was the large compressor test facility at the Institute of Turbomachinery in Hannover and was used to investigate an outward rectangular cross section volute and to gain further knowledge about the flow structure and loss mechanisms in the volute. The main components of the test stand consisted of the compressor, inlet and

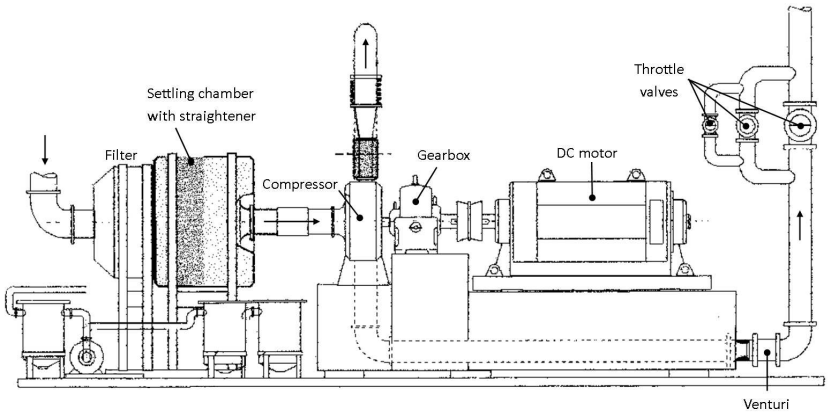

Figure 2.1: Test facility used by Hagelstein *et al.* (2000).

exhaust piping and DC motor with gearbox. Atmospheric air was sucked into the compressor through a suction chamber which has a fine air filter and flow straightener. Inlet conditions consisting of temperature and static pressure were measured in the suction chamber. On the outlet side the compressor, total temperature, static and total pressure were measured.

To gain a better understanding of the impeller-volute interaction measurements of total pressure, flow angle and total temperature were taken near the diffuser exit. These measurements were obtained by three different types of probes namely Cobra, Kiel and total temperature probes. In addition pneumatic five-hole probes were used to conduct flow field measurements to gain a better understanding of the flow mechanism in the volute. The flow rate was also measured on the outlet side with the use of a venturi. The flow rate was controlled with three parallel arranged throttle valves. The test facility was fully automated with the control and measurement conducted from an isolated control room.

In both studies industrial sized compressors were used with impeller sizes of 300 mm for Lim *et al.* (2011) and 400 mm for Hagelstein *et al.* (2000). The large impeller diameters limit the maximum attainable rotational speed as a result of increased blade tip velocities. At these high tip velocities sonic conditions are likely to occur and material strength limitations have to be taken into consideration. These operating speeds fall far below those required by micro gas turbines thus motors capable of operating at speeds consistent with micro turbines are sought after.

Electric motors such as brushless DC permanent magnet motors have been widely used in the aerospace industry and have been used for high speed appli-

cations (up to 100 000 rpm). These electric motors have numerous advantages over other types, however they are very expensive and require greater motor drive complexity. Although not specifically aimed at aerospace or automotive applications, a study was performed by Soong *et al.* (2000) to investigate the design of a high-speed induction motor for commercial centrifugal compressors in industrial cooling applications. The goal was to replace conventional compressors used in these cooling applications with a small high speed centrifugal compressor. Therefore a commercially viable electric motor was sought to drive the compressor.

Firstly Soong *et al.* performed a trade-off study to select the correct motor technology. Here they compared brushless DC permanent magnet, induction and switched reluctance motors. From the results of the trade-off study the induction motor was selected. The selection was based on critical speed, motor efficiency and relative cost. Test results from several pre-prototypes were successful in which a maximum speed of 60 000 rpm was achieved. This speed however is not sufficient for the design speed at which the proposed centrifugal compressor is specified to operate.

Driven as complete micro gas turbine Test facilities developed by Lobik (1995), Aus der Wiesche (2012) and Krige (2012) utilised commercial micro gas turbines where Benini and Giacometti (2007) designed and tested their own micro gas turbine. Lobik investigated the use of micro gas turbines for UAV applications. At the time that the study was conducted he performed a survey to determine the state of the art in UAV propulsion. As a result a JPX-240 micro gas turbine from JPX, France was selected. His selection was based on his survey of performance trends. In addition a review of engine performance codes was conducted to determine which would accurately represent the performance of the test engine.

Lobik's test facility was a permanent installation. An I-beam was welded to a attachment plate and bolted to the wall of the laboratory. The gas turbine was then suspended from the I-beam by a spacer, cradle and thrust beam. A hole was drilled in the wall to accommodate an outlet duct for the exhaust gas. The data acquisition used in his study is now obsolete and of no concern. In contrast to this design Aus der Wiesche, Krige and Benini and Giacometti designed portable test benches.

The test facility by Aus der Wiesche (Figure 2.2a) was designed specifically to be low cost and ensure wide distribution. In addition they present a novel method of performance prediction by means of a thermal measurement approach as a way of bypassing the need for special electrical environments. In the design Aus der Wiesche refer specifically to the ASME PTC 22 test code

(a) Test facility by Aus der Wiesche (2012). (b) Test facility by Benini and Giacometti (2007).

Figure 2.2: Micro gas turbine test facilities

which applies to gas turbine engines but also mention that modifications were required to accommodate the use of a micro gas turbine. The gas turbine used on the facility was a SPM5 engine from JetCat, Germany. The test facility is mounted on a portable table and contains all auxiliary systems (computer, engine control unit, fuel tank, cooling system) needed for correct operation. Because a thermal brake was used there was no need to connect to an electric network to dissipate the gas turbine power.

Krige used a Baird Micro Turbine (BMT 120 KS) for his test bench in which he aimed to evaluate the engine performance and subsequently increase the thrust by redesigning the vaned diffuser of the centrifugal compressor. His test bench is a simple design which consisted of two U-shaped aluminium frames of different size which fit into one another. The larger frame was fixed to a base frame which was secured to the laboratory floor. The gas turbine was secured to the back of the smaller frame to allow for a bellmouth and circular inlet duct. The smaller or runner frame as defined by Krige, was placed inside the larger frame and fixed to ball bearing runners placed on the inside of the larger frame. This allowed the runner frame to move an in axial direction so that thrust could be measured.

The test facility constructed by Benini and Giacometti (Figure 2.2b) was defined and developed for micro gas turbine for research purposes. The design specifications were focussed on producing a low-cost, lightweight system capable of producing 200 N of thrust. Every engine component namely the compressor, combustion chamber, turbine, nozzle and assembly was designed from scratch by following basic thermodynamic and mechanical principles. Initially a thermodynamic analysis of the entire system was performed by means of a Brayton-Joule cycle after which they described the design and manufacturing

processes of each engine component. The initial thermodynamic analysis was subject to numerous constraints regarding the operating conditions, various component efficiencies and the fuel/air mixture.

Driven as complete turbocharger Smith (2010) performed a study to compile the specifications needed for the development of a test facility for micro gas turbine development. He discusses the challenges needed to be overcome regarding the development of micro gas turbine test facilities and presents numerous tables of calculations of theoretically achievable performance figures. In his study he identified various problems and design challenges regarding the high speed operation of micro gas turbines. Smith's performance calculations were based on atmospheric conditions at sea level and efficiencies of various components from design norms of micro gas turbines.

For the geometry of the various gas turbine components he uses average measurements based on four known designs to be manufactured in South Africa. The parameters used for the centrifugal compressor was an isentropic efficiencies of $\eta_c = 0.79$ and impeller tip diameter of $D_2 = 80\,\text{mm}$. From the calculated results, Smith defines measurement ranges for the temperature and pressure that need to be recorded by instrumentation. For the compressor a maximum outlet pressure of 325 kPa and outlet temperature of 430 K is given.

His calculations have shown that an increase in pressure ratio and turbine inlet temperature (1300 K) will have a great influence on the generated thrust, however the only limitations in achieving these required levels of thrust is the ability of the materials to maintain structural integrity. In the development of his proposed test facility, Smith discusses the common features of commercially available turbocharger test facilities. Commercial test facilities by TQC Automation and the Southwest Research Institute (SwRI) are orientated vertically and horizontally respectively (shown in Figure 2.3a and 2.3b).

The test facility proposed by Smith differs from the commercial turbocharger facilities since it has the ability to measure thrust. He opted for a vertical layout such as the one used by TQC Automation & Test Solutions. The compactness of the design is emphasised by the fact that the intake is situated directly beneath the bench. Air enters through a bellmouth, flow straightener and a laminar flow element to correct and eliminate any turbulent flow.

Speed measurement is done with a laser sensor, which looks directly up the inlet through the laminar flow element (LFE) and reflects off the blades of the centrifugal impeller. The compressor module is constructed in a similar way to that of a micro gas turbine's, but without the inclusion of a combustor. Air is radially diffused through a vaned or vaneless ring. The radial flow is redirected

(a) Test facility at TQC Automation & Test Solutions (2012).

(b) Test facility at the Southwest Research Institute (2012).

Figure 2.3: Commercial turbocharger test facilities

through a large annular space and throttled through a simple cone which exits to the atmosphere in an axial direction. The drive turbine used is the same as that of conventional turbocharger units. In this instance pressurized air enters the turbine horizontally and exits vertically through a pipe and silencer hood. The rotational speed is controlled by throttling airflow at the exhaust with coarse and fine shunt valves. The vertical stacking of components ensures that the facility is accurately assembled.

Smith further describes how the test facility may be modified to incorporate an axial flow turbine similar to those used in micro gas turbines. He suggests that an independent combustor be used to achieve realistic levels of performance. The facility must also be modular and easily modifiable to accommodate the fitting of components such as an axial flow turbine, inlet guide vanes, turbine exit nozzle, etc. In conclusion Smith recommends the current vertical format for the test facility as it has many advantages in terms of ease of modification and accuracy of assembly. In spite of suggesting the use of a pre-heat burner he selects cold pressurised air to drive the turbine because of safety issues regarding the use of pre-heat burners. Other safety concerns that need to be addressed is the addition of a disc burst and noise suppression associated with high rotational speeds. Therefore he recommends the design of a cover with the capacity to absorb a disc burst and the use of silencers to suppress noise.

A white paper by Garrett Turbochargers (2012*b*) gives a good overview regarding the safety issue of a disc or wheel burst. The type of disc burst is defined as well as the causes for such an event to occur. The most likely type to occur is that of a blade burst. This occurs when centrifugal forces at speed

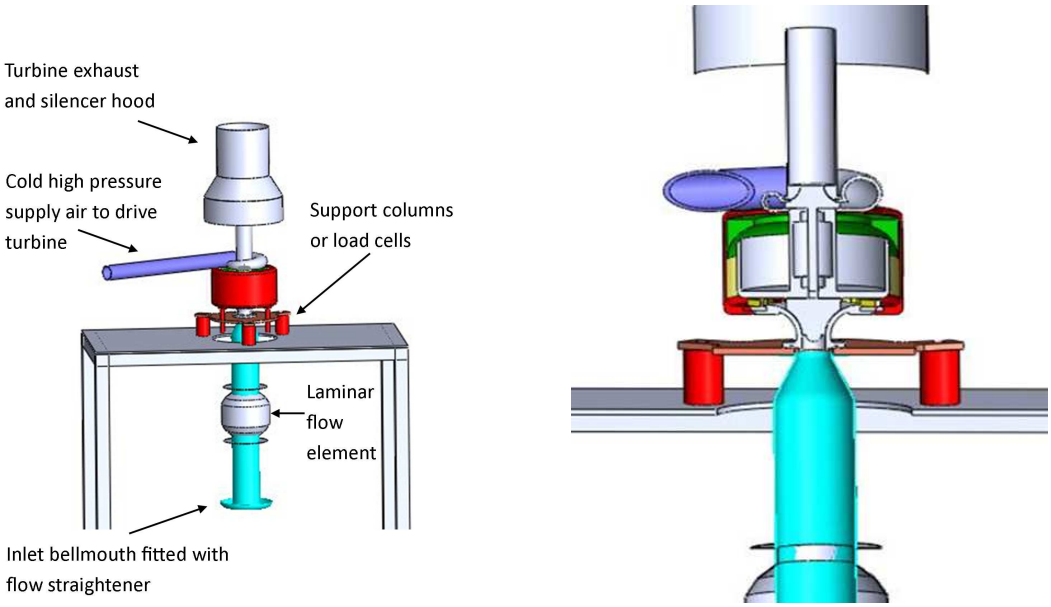

(a) Test facility. (b) Cross section view of test facility.

Figure 2.4: Proposed test facility by Smith (2010).

overcome the mechanical strength of the blade root section which connects the blades to the hub. The second and most extreme case is called a hub burst, which also has the highest potential for causing damage to the housing. This occurs when the ultimate strength of the main hub to which all the blades are attached is exceeded and therefore breaks apart into several pieces. The causes for a disc burst are as a result of low cycle fatigue, foreign object damage and reduced material strength through the combination of high speed and high temperatures. Continuous references are made to failures occurring due to excessive abuse under operating conditions. The examples used to illustrate the conditions for a disc burst are extreme and none of which will be exerted on the test compressor in question.

2.2 Numerical analysis of centrifugal compressors

Computational fluid dynamics has been successfully used for turbomachinery flow analysis either for performance prediction or to gain better understanding of various flow phenomena that occur within these machines. Numerical analysis has been included as part of the scope and serves as a supplementary study to the main focus of the project. Insight about the use of numerical modelling and the validity of comparing simulated and experimental data was

sought.

Ling *et al.* (2007) performed a numerical investigation on a small gas turbine compressor with the aim to increase the performance and efficiency. They utilised a KJ66 gas turbine engine fitted with a KKK2038 compressor impeller coupled to a wedge-type diffuser as a benchmark study. The compressor had a tip diameter of $D_2 = 66\,\text{mm}$. The original compressor stage was simulated and performance and efficiency values were mapped at operating speeds of 80 000, 100 000 and 120 000 rpm and compared to that of the manufacturer. ANSYS®, Inc. Turbogrid™ and CFX® -mesh was used to create the flow domain of the impeller and diffuser section respectively with the flow domain solved by the CFX solver.

According to Ling *et al.* (2007) the results from the CFD simulations correlated well with that of the engine specification, however only the simulated results are presented. As part of the design process Benini and Giacometti (2007) performed a numerical analysis of the centrifugal compressor which they designed and utilised in their micro gas turbine engine. An iterative procedure was followed in obtaining the final compressor design. The predicted performance results from the numerical analysis was compared to a first-cycle analysis and redesigned until satisfactory convergence was achieved. The final predicted performance results of the compressor are presented as well as those from experimental test runs, but were not explicitly compared.

The study by De Wet *et al.* (2010) demonstrated the accuracy of CFD by comparing two well known compressor cases found in literature, namely the Eckardt O-Rotor and the "Radiver" open CFD test case. The reason for verifying the two test cases was to validate the redesign of a locomotive turbocharger compressor using CFD (the compressor rotor had a diameter of 400 mm). De Wet *et al.* models and simulates the two test cases using specialist software by NUMECA™ International, namely the FINE™/Turbo package. De Wet *et al.* compared the CFD and experimental results of both validation cases upon which he found good agreement. For the case of the Eckardt O-Rotor, there was good correlation between the measured and numerical data, especially at the stall and choke conditions. His results showed a maximum error in pressure ratio of 0.043 and total-to-total efficiency of 1.99 % at a mass flow of 5.31 kg/s. In addition the verification of the O-Rotor diffuser measurements produced a maximum static pressure error of 1.38 %.

The study by Kim *et al.* (2011) is another example where a numerical investigation was verified with experimental results. They numerically investigated the effects of blade angle distribution on the performance and loss generation of centrifugal compressor impellers. Four different blade profiles were investigated, which included the original profile used by the author in a previous

study. The experimental results from the previous study were compared to the corresponding numerical results for verification purposes.

According to Kim *et al.* there was good quantitative and qualitative agreements over a majority of the operating ranges. Hagelstein *et al.* (2000) investigated the flow in a compressor volute experimentally and numerically. For the numerical analysis they used a three-dimensional Euler code in which the wall-friction term and a tuned artificial dissipation term accounted for the viscous effects. Reasonable agreement was achieved between the experimental and numerical results which helped in gaining detailed knowledge about the flow and loss mechanisms of a centrifugal compressor volute.

Chapter 3

Experimental Testing

The test facility is installed in the Gas Dynamics Laboratory (Mechanical and Mechatronic Department Building, Room 143) at the engineering faculty of Stellenbosch University. Where applicable the test facility was designed in accordance with the ASME PTC 10 Performance Test Codes on Compressors and Exhausters (ASME, 1997) and follows the methodology proposed by Smith (2010). The decision to drive the test facility with cold compressed air is motivated by the fact that the required rotational speeds are not attainable with a direct electric drive (motors of this nature would be expensive); the preheating of air with hydrocarbon fuel holds an inherent safety risk and a compressed air system is available which is able to supply the test facility with compressed air. Figures 3.1a and 3.1b illustrate the general layout of the test facility (dimensions in mm).

3.1 The test facility

Layout The test bench is driven by compressed air which is supplied by the existing compressed air installation at the Mechanical Engineering Department. The installation has the capacity to provide compressed air at a maximum pressure of 1 MPa. The air is treated to remove excess moisture by passing through two parallel coupled air driers. The treated air is then stored in two separate receiver tanks with a combined capacity of 88 m^3. From the receiver a supply header, rated at 1.4 MPa is fed directly to the Gas Dynamics Laboratory where the test bench is located. The supply to the laboratory is controlled via a manually operated ball valve which is situated at the wall where the supply header enters the laboratory. Inside the laboratory the header is equipped with several air supply points. A system pipeline diagram describing the layout of the test facility within the laboratory is shown in Figure 3.2.

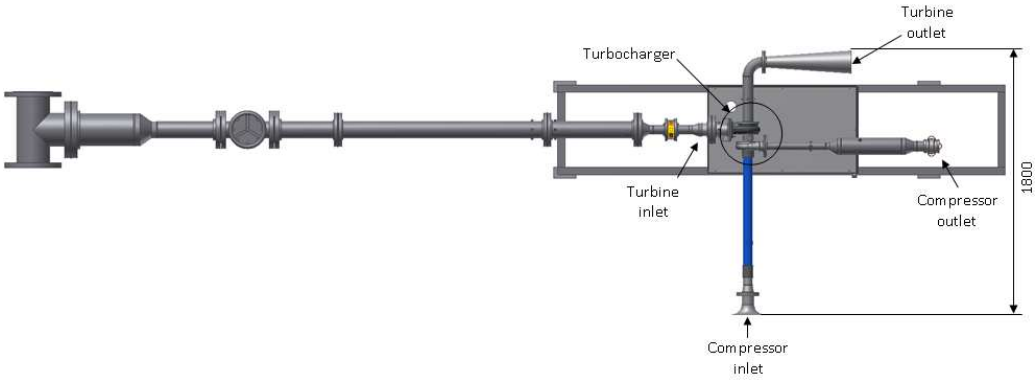

(a) Top view.

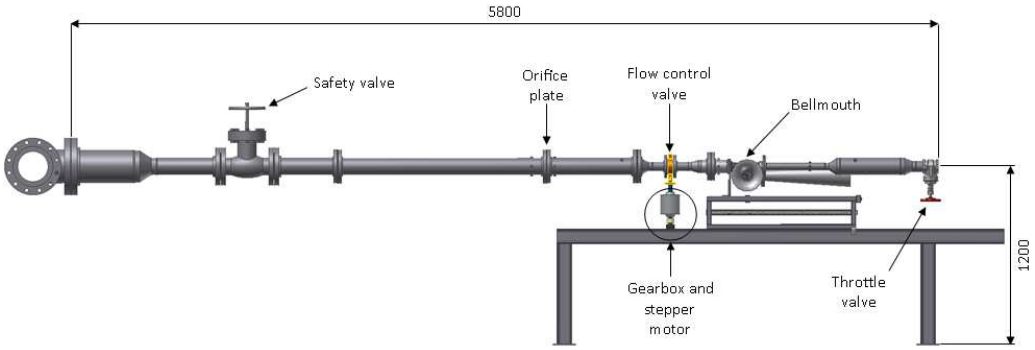

(b) Side view.

Figure 3.1: Compressor test facility.

Turbine side The pipe network leading to the turbine inlet branches from the header supply. It is reduced from 200 mm to 100 mm nominal bore (NB), to accommodate a manually operated safety shut-off ball valve. Downstream of the shut-off valve is a flow measurement section to measure the flow capacity through the turbine side of the turbocharger. The flow measurement is performed with an orifice plate. Downstream of the flow measurement section the pipe is reduced from 100 mm to 50 mm NB to accommodate a butterfly flow control valve. This valve is connected to a gearbox and stepper motor and is used to regulate the flow through the turbine. All piping used on the turbine inlet side is ANSI (American National Standards Institute) rated schedule 40 with wall thickness's varying from 8.18 mm for 200 mm NB to 3.91 mm for 50 mm NB. Air at the turbine outlet is exhausted to atmosphere through a 90° bend connected to a conical diffuser.

Compressor side On the compressor inlet side air enters through a bellmouth and a straight section of PVC tubing. The NB of the PVC tube corresponds to the compressor casing inlet diameter. The inlet to the bellmouth is covered with a meshed grid to prevent any foreign matter from being sucked

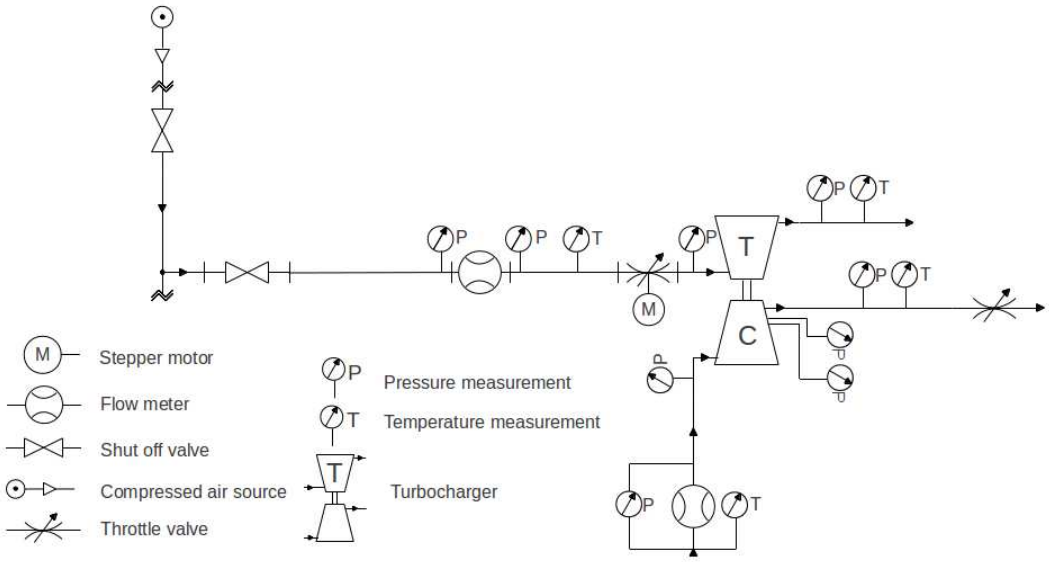

Figure 3.2: System pipeline diagram of test facility.

into the compressor during operation. The volute exit cone has a sudden expansion from 40 mm to 60 mm. A bushing was manufactured with an internal diameter equal to 40 mm and fitted within the exit cone to keep the inner diameter uniform and prevent pressure variation due the area enlargement. The air is discharged through a straight pipe section with an NB equal to the bushing internal diameter. Downstream of this section the pipe NB is enlarged from 40 mm to 100 mm to accommodate thermocouples used for measuring the exit temperature. A gate valve is fitted at the outlet of the pipe to adjust the operating point of the compressor by throttling the flow.

Mounting frame The turbocharger, data acquisition electronics and instrumentation are all mounted on or located beneath a rectangular frame made from 50 mm mild steel square tubing. This frame is mounted on a larger frame which is fastened to the laboratory floor for stability. The upper frame has the ability to slide back and forth on the fastened frame to allow adjustment of the test set-up. The turbocharger is fastened to a plate cover on top of the upper frame with slotted brackets which allows for slight height adjustments.

3.2 Turbocharger selection

The sizing of the turbocharger was performed using an indirect method proposed by Brun and Nored (2006) and the project specifications from the CSIR Snedden (2010) (Table 1.1). Brun and Nored (2006) give four methods for determining gas turbine power. Two methods involve direct measurements of torque and power which yield the lowest uncertainty. The remaining two

methods have a higher uncertainty and indirectly determine the gas turbine power though driven centrifugal shaft power measurements and gas turbine heat balance measurements. None of the above mentioned methods were possible, however by applying the method of driven centrifugal shaft power and making a few assumptions an estimate is possible. Firstly the estimated power required to drive the compressor was calculated. Following that, the estimated size of the compressor impeller was calculated from Dixon (2005).

3.2.1 Compressor power

The power that has to be generated by the turbine in order to drive the compressor is determined by estimating the power absorbed by the compressor P_c, using the isentropic head (H^*), density and flow rate(Brun and Nored, 2006):

$$P_c = P_o \eta_m \approx \rho_s Q_s H^* \tag{3.2.1}$$

The density (ρ_s) and flow capacity (Q_s) are taken at the suction side of the compressor. It is assumed that the mechanical efficiency (η_m) of the machine is 0.9. According to Brun and Nored the actual enthalpy change must be used, however in this case it is assumed that the enthalpy change is isentropic since no actual enthalpy data is available. Assuming ideal gas conditions the isentropic enthalpy or work done per unit mass is left to be determined.

$$H^* = h_d - h_s = h(p_d, s_s) - h(p_s, T_s) \tag{3.2.2}$$

The enthalpy on the discharge side (h_d) of the impeller is associated with the entropy on the suction side (h_s) since the entropy change in an isentropic process is zero. From thermodynamic properties of dry air at 293 K the enthalpies are calculated as follows:

$$h_s = C_{p_s} T_s \tag{3.2.3}$$

$$h_d = C_{p_s} T_s \left(\frac{p_d}{p_s}\right)^{\frac{\gamma-1}{\gamma}} \tag{3.2.4}$$

Substituting equations 3.2.2 - 3.2.4 into 3.2.1, the estimated power absorbed by the compressor is calculated to be:

$$\begin{aligned} P_c = P_o \eta_m &\approx \rho_s Q_s H \\ &\approx 48\ kW \end{aligned} \tag{3.2.5}$$

3.2.2 Compressor sizing

When estimating the size of the compressor impeller the following assumptions where made:

- the compressor has radial vanes ($\beta_2 = 0°$).
- no whirl is imparted at the eye ($c_{\theta 1} = 0\,\mathrm{m/s}$).
- a typical slip factor $\sigma = 0.9$.
- power input factor $\psi = 1.035$.

The specifications received from the CSIR such as the pressure ratio (4.72), isentropic efficiency (79.8 %) and rotational speed (121 000 rpm) were used in the calculation. The estimated impeller size is calculated from:

$$\frac{p_{t3}}{p_{t1}} = \left(1 + \frac{\eta_c \psi \sigma U_2^2}{C_p T_{t1}}\right)^{\frac{\gamma}{\gamma - 1}} \tag{3.2.6}$$

and rearranged to solve for U_2 so that:

$$U_2 = \sqrt{\frac{C_p T_{t1}}{\eta \psi \sigma}\left[\left(\frac{p_{t3}}{p_{t1}}\right)^{\frac{\gamma}{\gamma - 1}} - 1\right]} \tag{3.2.7}$$

also from $U_2 = \omega r_2$ and $\omega = N\frac{\pi}{30}$ such that:

$$\omega = 121\,000\frac{\pi}{30} = 12\,671.09\,\mathrm{rad/s} \tag{3.2.8}$$

$$r_2 = \frac{U_2}{\omega} = 37.09\,\mathrm{mm} \tag{3.2.9}$$

The estimated impeller outlet diameter is calculated to be $D_2 = 74\,\mathrm{mm}$. This diameter size correlates well with the average impeller size used in the study by Smith. The turbocharger with an compressor outlet diameter closest to the estimated calculations was a Kühnle, Kopp & Kausch (KKK) turbocharger (Table 3.1) with an impeller outlet diameter measured at $D_2 = 81\,\mathrm{mm}$:

Table 3.1: KKK K27 turbocharger identification information.

KUNDE-NR	-
GRÖSSE	27
ALT-NR	KA 50128532 00096
AUSF-NR	5327 988 6206

3.3 Instrumentation and hardware

The following section discusses the instrumentation and data acquisition utilised on the test facility.

3.3.1 Pressure measurement

Several pressure transducers where used to monitor the static and differential pressure of the compressor at various locations stipulated by the ASME test codes, indicated in Figure 3.5. These locations are:

1. across the bellmouth, perpendicular to the plane of flow. (p_0)
2. upstream of the compressor inlet, (p_1).
3. at the impeller outlet, (p_2).
4. at the vaneless diffuser outlet, (p_3).
5. downstream of the compressor outlet, (p_4).

At each pressure station there are four pressure taps spaced 90° apart. An Endress+Hauser PMD70 differential pressure transducer was used to measure the pressure across the bellmouth with a maximum differential pressure range of 3 kPa. HBM P8AP absolute pressure transducers were used to measure the pressure at all other pressure stations. These transducers have a maximum operating range of 1 MPa. All pressure transducers were used in conjunction with HBM AE301 strain gauge measuring amplifiers. The measuring amplifiers were scaled according to the estimated maximum pressure to be measured at the various stations in order to obtain the best measuring resolution. The calibration curve (with corresponding equation) for each transducer is shown in Appendix A.1. To measure the static pressure at the impeller and diffuser outlet radial pressure taps where inserted in the compressor backplate (Figure 3.3).

The pressure taps were manufactured as brass inserts each with a 1.5 mm diameter hole and press fitted into the compressor backplate. Four pressure

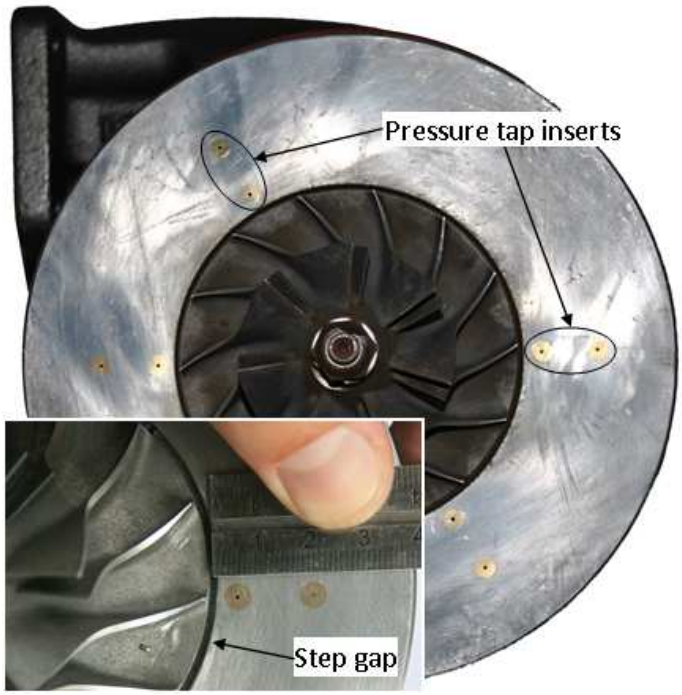

Figure 3.3: Impeller and diffuser pressure tap locations.

taps were fitted at each station. From Figure 3.3 one can see that the impeller outlet pressure taps are not situated exactly at the impeller outlet radius. This is because of a circumferential gap that exists between the impeller and diffuser and the diameter of the inserts limit the location of the centre of the pressure tap. This however was not the case at the diffuser outlet radius. The pressure distribution conditions through the turbine were also monitored at the following locations:

1. across the orifice plate, perpendicular to the plane of flow.
2. at the turbine outlet.

3.3.2 Temperature measurement

For the temperature measurements J-type thermocouples from Unitemp Pty (Ltd) were used to measure the temperature. The locations are:

1. at the bellmouth inlet, (T_0).
2. at the compressor outlet, (T_5).
3. at the turbine inlet.
4. at the turbine outlet.

As stipulated by the ASME test codes, four thermocouples per station were used for the compressor, (Figure 3.5). For the turbine only one thermocouple per station was regarded as sufficient. The thermocouples at the bellmouth inlet were fixed to the safety grid at a distance equal to the bellmouth throat diamter from the inlet and spaced 90° apart. These measure the inlet total temperature and are used for calculating the mass flow through the compressor. Temperature is not measured at the inlet of the compressor and is calculated iteratively using the mass flow, measured inlet total temperature and compressor inlet static pressure. It was assumed that the process representing the air flowing from the bellmouth to the compressor inlet was adiabatic. In order to reduce heat loss to the environment and ensure adiabatic conditions insulation was added to the outlet piping. The temperature at the compressor outlet was measured with half-shielded probes.

The measurement of total temperature in an ideal moving fluid by an idealised probe is based upon the assumption of an isentropic process of deceleration i.e. the stagnation condition is adiabatic and reversible. However in the context of practical thermometry (a real probe immersed in a real moving gas) this isentropic assumption becomes invalid due to real gas and probe effects. The process is diabatic as a result of heat transfer to and from the gas and probe. The stagnation of fluid on the probe is not quasi-static and therefore not reversible. Also boundary layer-effects such as viscosity and thermal conductivity conflict with this isentropic assumption. In addition impact effects associated with Mach and Reynolds numbers also affect the measurement of a real probe. Therefore in practice a real probe will indicate an equilibrium temperature which differs from the total temperature measured by an idealised probe in an ideal gas.

A dynamic correction factor K is introduced to correct the measurement of the real probe. From Benedict (1977) the total temperature measured by the real probe is expressed as:

$$T_t = T_p + (1 - K)\frac{c^2}{2C_p} \tag{3.3.1}$$

The dynamic correction factor determines the impact of the dynamic temperature on the total temperature. From experimental results published in Benedict (1977) it was found that the half-shielded probe with a value of $K \approx 0.96$, (Figure 3.4) is the least sensitive to the aforementioned real gas and probe effects and was therefore the most suitable type of probe.

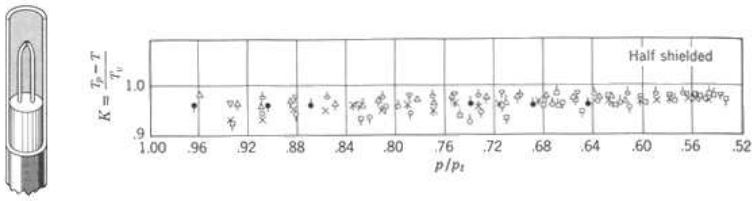

Figure 3.4: Half-shielded thermocouple probe.

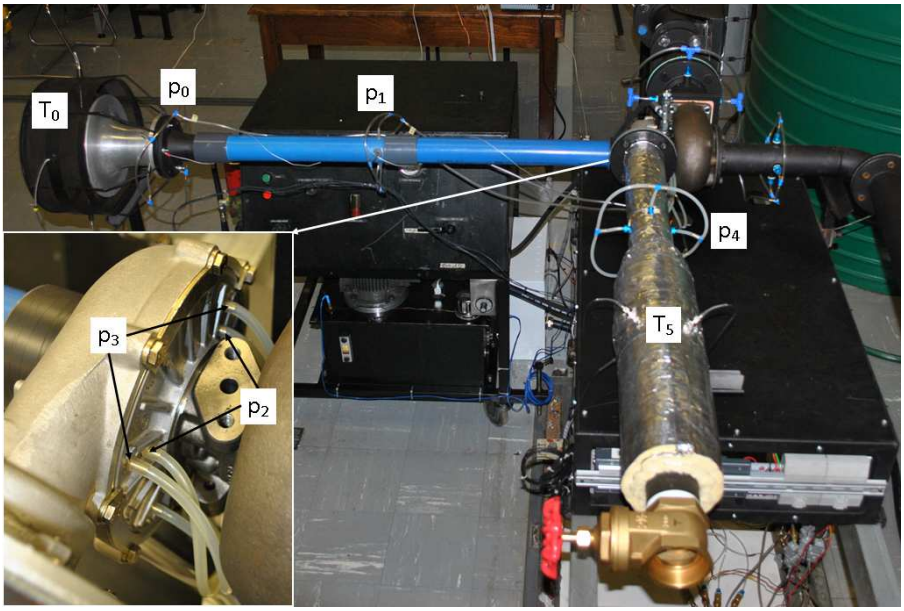

Figure 3.5: Compressor pressure and temperature measurement locations.

3.3.3 Flow rate measurement

Flow rate is measured through the compressor and turbine and calculated with Bernoulli's flow obstruction theory. The governing equation describing the flow through an obstruction flow meter is:

$$\dot{m} = C_d E \epsilon \frac{\pi}{4} d^2 \sqrt{2 \Delta p \rho_1} \tag{3.3.2}$$

The flow rate through the compressor is measured on the inlet side with a bellmouth (Figure 3.5). The bellmouth had to be calibrated in the Heat Transfer Laboratory of the Mechanical and Mechatronic Department Building using a method similar to that of Smith (1985). The mass flow measurement was implemented in accordance with ASME PTC-10, where applicable. As previously mentioned the pressure difference across the bellmouth is measured with a differential pressure transducer. The high pressure side of the transducer measures the ambient pressure. The low pressure side measures the throat static pressure from four static pressure taps spaced at 90° around the throat

of the bellmouth. The bellmouth calibration resulted in a discharge coefficient, C_d value asymptotic to 1. The calibration curve is shown in Appendix A.2

Flow rate through the turbine is measured with an orifice plate and designed in accordance with the BS (British Standard) 1042 standard (BSI, 1981). Due to the lack of information regarding the operation of the turbine an estimate of the flow was made when the orifice plate was designed. The diameter ratio β was calculated using the maximum operating pressure and design pressure drop and estimated mass flow rate. For a supply pressure of 1 MPa, pressure drop of 20 kPa and mass flow rate of 1 kg/s, a diameter ratio of $\beta = 0.526$ was calculated. The sample calculations are shown in Appendix E.1.

3.3.4 Speed measurement and control

Speed Measurement Rotational speed measurement is typically accomplished by proximity, magnetic, or inductive sensors. These sensors have to be mounted in close proximity to the shaft or any rotating part of the machine. In the context of this test facility this proved difficult to implement as there were limited locations for mounting the sensors. Since a complete turbocharger unit was used, the only possible access to any rotating surface was at the inlet of the compressor. Because of the manner in which these sensors operate and the need for the inlet flow to remain undisturbed, these sensors were therefore not adequate to measure the rotational speed.

Another method of measuring the angular speed is by means of optical reflection. These sensors typically use an infra red or high concentration light beam that reflects off a rotating part of the machine (shaft or blade). The advantage of these sensors over those previously mentioned is the ability to be located at a reasonable distance from the reflective surface, thereby eliminating the problem of flow disturbance. Two important aspects determine the choice of the reflective sensor namely; the switching frequency and the reflective range. The sampling frequency f_s is governed by the Nyquist-Shannon sampling theorem which states that for a signal to be perfectly reconstructed it must be sampled at greater than twice the maximum sampling frequency of B_{max}, which in this case is the frequency at maximum rotating speed of the shaft:

$$f_s = 2B \tag{3.3.3}$$

For an estimated maximum rotational speed of 121 000 rpm:

$$\begin{aligned} B_{max} &= \frac{rpm}{60} \\ &= 2\,\text{kHz} \\ &\approx 2.02\,\text{kHz} \end{aligned} \tag{3.3.4}$$

therefore the minimum required sampling frequency is $f_s = 4.04\,\text{kHz}$.

After considering the possible mounting locations and various factors regarding reflective sensors it was decided to use an infra-red sensor reflecting through the side of the inlet pipe coupling perpendicular to the direction of flow. The sensor reflects off a flat cut away section which has been machined from the hub protruding in front of leading edge shown in Figure 3.6. By mounting the sensor in this way the inlet flow is left undisturbed.

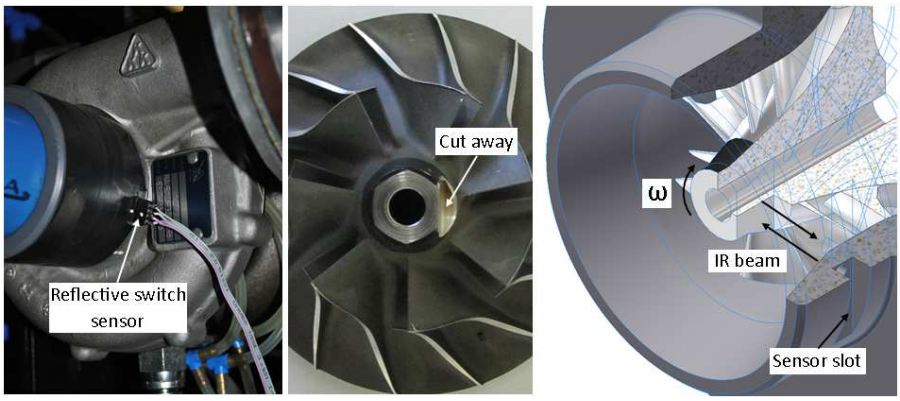

Figure 3.6: Location and mounting of the tachometer.

An infra-red OPB732 Long Distance Reflective Switch from OPTEK Technology was selected because of its reflective range and small size. The sensor consists of an infra red diode and photo-transistor. Essentially the transistor acts like a switch whenever the infra red beam is reflected. The sensor output is an AC voltage signal, ideally a square wave, with a frequency that is directly proportional to the speed of the rotating impeller. The output is rarely perfect, since electrical "noise" distorts the shape of the wave, therefore signal conditioning and scaling was implemented to extract the frequency and convert it to a rotational speed.

Speed control The rotational speed of the compressor is controlled by varying the flow rate through the turbine. The flow rate is adjusted with a control valve situated upstream of the turbine inlet. The control valve is actuated by a stepper motor via a gearbox (Figure 3.7). The stepper motor was controlled with an Arduino Uno micro controller via a McLennan Servo stepper drive (Figure 3.8). The valve was remotely controlled by manual push button

switches. The speed measurement was used as feedback for the operator and stepper controller. Positional control on the valve was not implemented, instead limit switches were used to indicated the complete open/closed position of the valve.

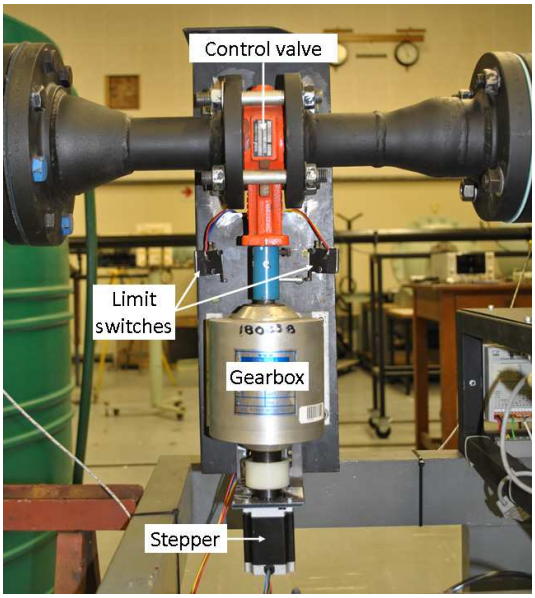

Figure 3.7: Flow control valve with gearbox and stepper motor.

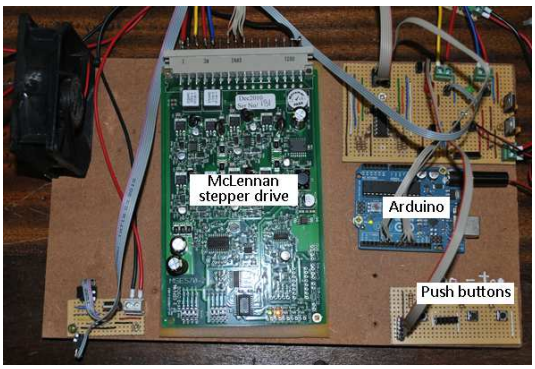

Figure 3.8: Stepper motor drive and Arduino micro controller.

3.3.5 Lubrication system

The lubrication of a turbocharger is crucial to the function of the entire system. Oil is needed to lubricate and cool the bearings. The oil for the turbocharger was supplied by a lubrication system based on a design by Nieuwoudt (1987) (Figure 3.9). The bearing system of the K27 turbocharger consisted of two

radial journal bearings and an end thrust bearing which can freely rotate on a thin film of oil (Figure B.2). The bearings have a set of small holes through which the oil can flow to reach the shaft. Care should be taken to ensure that the oil will penetrate these holes in order to prevent failure of the bearings and cause possible damage to other components of the turbocharger. This type of failure will occur as a result of blockage caused by abrasion between the bearings and shaft. This occurs due to improper lubrication when the oil is too viscous for sufficient penetrating through these holes. Another reason for failure of the bearings is caused by the accumulation of fine particulate (found in the oil) within these holes prevents the oil from reaching the shaft. These problems are avoided by correct heating and filtering of the oil.

For the purposes of this test bench modifications were made to the monitoring of oil pressure and temperature. The oil was pumped from a 20 l reservoir with a gear pump capable of delivering 16 l/min at 1460 rpm and was driven by a motor rated at 0.75 kW and 5 A. Nieuwoudt (1987) had specified the pump to deliver 4 times the flow rate needed for his turbocharger at a pressure of 200 kPa to 400 kPa. Information regarding the flow rate and oil pressure needed for the K27 turbocharger was unattainable from the manufacturers. However the flow rate provided by the pump was considered to be sufficient for the lubrication of the K27 turbocharger, based on a comparison to the turbocharger used by Nieuwoudt (1987).

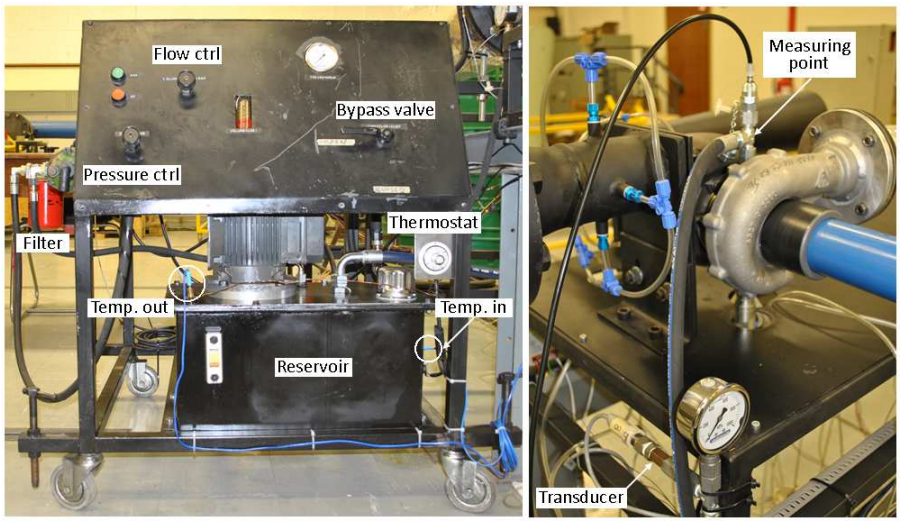

Figure 3.9: Lubrication system.

Oil pressure and flow rate could be adjusted with the pressure- and flow-control valves. The oil pressure was originally monitored only at the oil pump with an analogue pressure gauge. This was replaced with a new analogue gauge

with an extra gauge fitted at the inlet of the turbocharger bearing housing. The reason for monitoring the oil pressure at the turbocharger was to indicate the pressure drop across the piping and therefore the actual oil pressure entering the turbocharger. This pressure drop was measured to be at most 100 kPa during steady operation. As an added safety measure the oil pressure at the turbocharger was monitored with a pressure transducer with the reading being displayed on the data acquisition program to give real-time feedback to the test operator.

The heating of the oil plays an integral part in the correct operation of the turbocharger as it ensures that the oil reaches and maintains the right viscosity needed for optimal lubrication. Nieuwoudt (1987) implemented a 2 kW low intensity electrical heating element to heat the oil to the correct temperature without burning the oil. The oil temperature limit was manually set with a thermostat. In addition the oil temperature was measured with T-type thermocouples at two locations; at the oil return side after passing through the turbocharger where it was heated by the element and secondly on the intake side of the pump. This was to ensure that the oil maintained a uniform temperature throughout the system. A copper coil tube was used by Nieuwoudt (1987) as a heat exchanger to additionally regulate the oil temperature. This however was not needed and subsequently removed as the temperature remained constant and within safe limits during operation.

The type of oil used was Fuchs 15W40 heavy duty multigrade engine oil, as recommended by the suppliers of the turbocharger, Turbo Exchange, and proved to be successful. The bypass valve allows the system to be operated without the need for oil to flow through the turbocharger. Prior to testing, the oil was heated to the correct temperature by circulating it through the system and bypassing the turbocharger. The reason for this was to prevent overloading of the motor by pumping cold oil through the turbocharger. The motor was protected by a 5 A overload circuit. The final operating parameters of the lubrication system are presented in Table 3.2.

Table 3.2: Lubrication operating conditions.

Pressure	600 kPa
Temperature	60 - 70 °C
Flow Rate	4 l/min

3.4 Data acquisition system

Data acquisition (DAQ) was performed using the National Instruments™' (NI) CompactRIO (cRIO) and LabVIEW™ 2011 graphical development environment. The cRIO is a reconfigurable embedded control and data acquisition system consisting of an embedded controller for communication and processing, a reconfigurable chassis hosting the user field programmable gate array (FPGA) and various hot-swappable I/O modules. The cRIO system is programmed with LabVIEW™ and LabVIEW™ Real-Time application software. A schematic of the data acquisition system is illustrated in Figure 3.10. The data acquisition hardware was mounted on the test facility frame beneath the turbocharger shown in Figure 3.11.

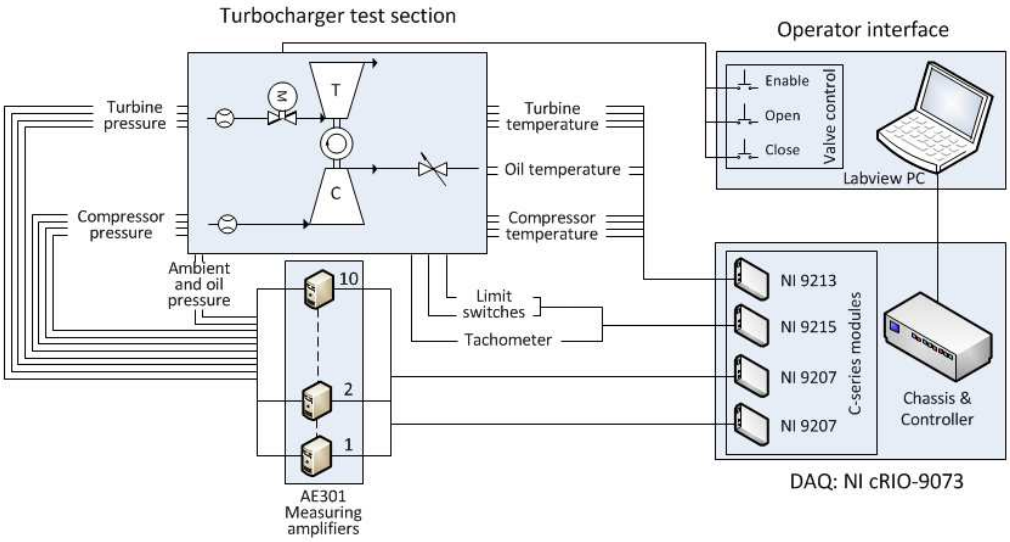

Figure 3.10: Data acquisition system schematic.

The DAQ system was designed by following a *Host and Target Application Architecture* for a real-time application (National Instruments, 2010*a*,*b*). The host application contains the user interface and is run from the host (laptop) computer and communicates with the real-time application on the target (NI-cRIO) computer. For the test facility, a cRIO-9073 was used which has a 266 MHz real-time processor, an FPGA chip and eight expandable C-Series module slots. These modules are data sampling cards and were connected to the various sensors. The modules used were:

1. Two Combination 8-Channel Voltage (±10 V) and 8-channel Current (4-20 mA) Analogue Input modules (NI-9207).

2. One 16-channel Thermocouple module (NI-9213).

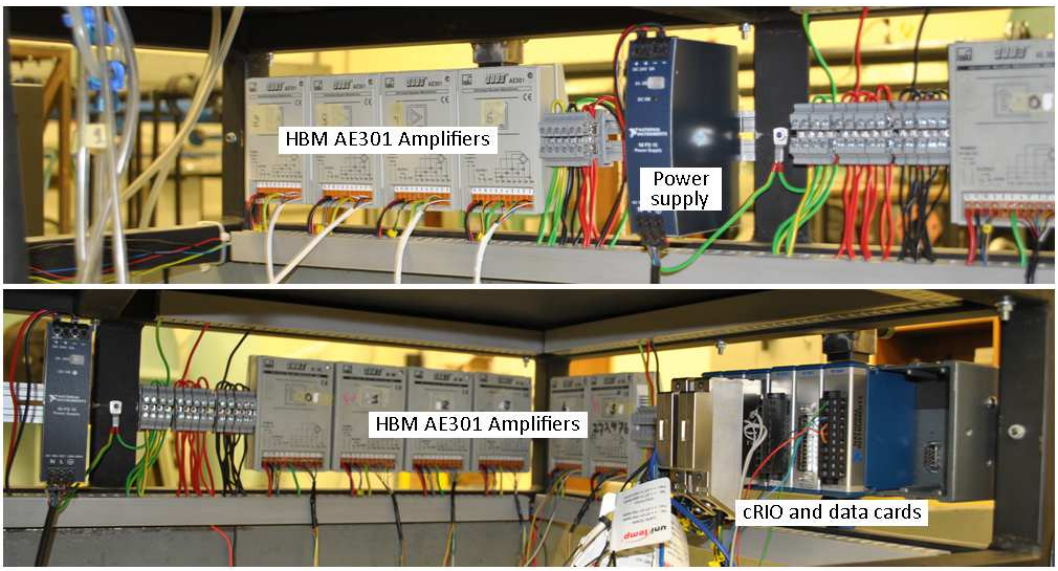

Figure 3.11: Data acquisition components.

3. One 4-channel 100 kS/s, 16 bit, ±10 V Simultaneous Sampling Analogue module (NI-9215).

3.4.1 Sensor measurements

All measurements were addressed through the cRIO-9073. The pressure measurements were sampled with the NI-9207 modules. The measuring amplifiers were calibrated to provide 0 - 10 V full scale output for each pressure measurement. The sampled signals were converted from voltages to the equivalent pressures in real-time using the respective equations obtained from the calibration curves. The temperature measurements were sampled with the NI-9213 of which each channel was configured to the type of thermocouple at the respective measuring station. Labview™provides tables and polynomial functions that convert the thermocouple voltage to temperature. The polynomial function were chosen by default and are shown in Appendix C.1.3. The temperatures were measured in Kelvin.

Regarding the accuracy of the temperature measurements, the NI-9213 has a built-in cold-junction compensation to correct for the contact between the thermocouple and module terminal. In addition further offset errors are eliminated by measuring an autozero channel at the start of each scan. Similarly to the pressure and temperature measurements the compressor flow rate is computed and displayed in real-time. The sampling of the NI-9207 and NI-9213 modules were moderate at rates of 500 Hz and 1.2 kHz (aggregated) respectively. These sample rates were sufficient as the measurements were focussed on steady state conditions.

The speed measurement was sampled with the NI-9215 module. The sampling rate of 100 kHz per channel exceeds the required sampling rate calculated in §3.3.4 and is therefore well suited for the speed measurement. The rotational speed was determined by measuring the frequency of the tachometer (optical switch) signal and scaling it to rpm. The frequency was determined by measuring the period of the sampled signal either from a rising or falling edge trigger. The measurement range and sensitivity could be adjusted by specifying a signal offset and hysteresis. The virtual instrument (VI) block diagram code for the various measurements is shown in Appendix C.1.

3.4.2 Program operation

The target application consists of the FPGA chip and real-time processor embedded in the cRIO chassis and controller. The cRIO's FPGA was used in conjunction with the real-time processor to ensure parallel and deterministic data acquisition. All the raw measurements were sampled and processed through the FPGA. Four separate acquisition loops were used for each of the data cards. The FPGA allows the sampling speed to be set individually for each loop, therefore allowing the speed measurement to be processed at a faster rate without affecting the sampling integrity of the pressure and temperature data. The raw data from the FPGA is transferred to the real-time processor where the sampled measurements are scaled and converted to SI units. In addition the activation of the limit switches are monitored by means of boolean logic. The FPGA and real-time applications were treated as separate VI's.

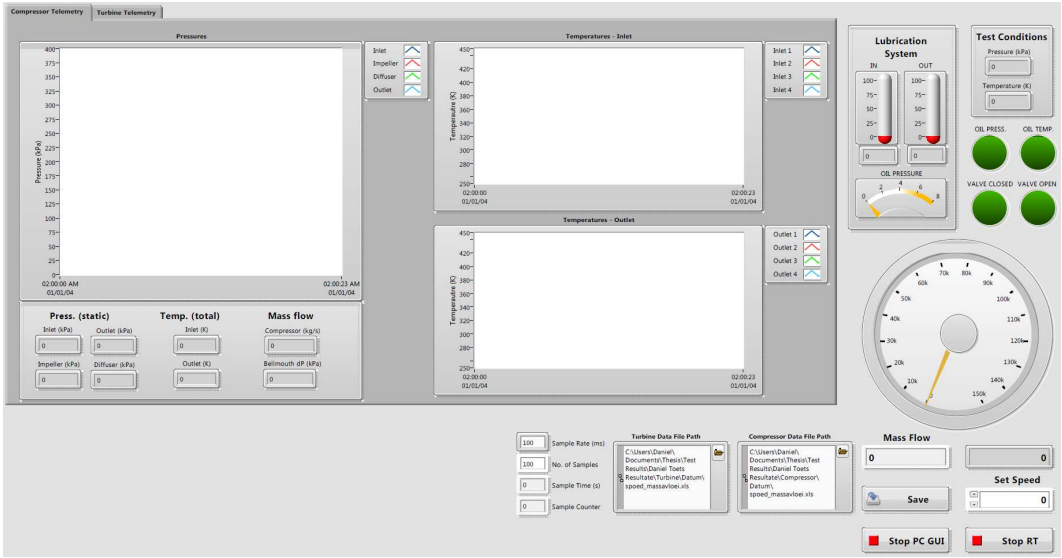

Figure 3.12: Data acquisition GUI.

The host application is the graphical user interface (GUI) of the measurement system and is operated from a personal computer by the test operator (Figure 3.12). It allows the monitoring and storage of data of all sensors coupled to the test bench. Two tabs were created for the compressor and turbine in which to view the respective pressures and temperatures during operation. Furthermore the lubrication system is also monitored with information about the oil temperature and pressure being displayed to the operator. A number of warning indicators alert the operator in the event of a problem. The operator is warned if the oil pressure and temperature are not within safe operating limits and indicates whether the flow control valve is either fully closed or open thereby preventing any damage occurring to any part of the flow control assembly. Other telemetry displayed include the test ambient conditions, compressor flow rate and operating speed. The user has a choice of setting the sampling rate, sample time and file location on the GUI. The compressor and turbine data are stored separately in Microsoft Excel™ .xls format.

3.5 Test method and data reduction

At first preliminary tests were done to verify the operation of the test bench and to determine the capabilities in comparison with the recommended test procedures prescribed in ASME PTC-10 and Brun and Nored (2006). From these tests, values for the number of test points, time duration at a specified speed and total test time could be determined. External factors that would have an affect on the operation of the test bench were the minimum allowable air receiver pressure required by other facilities within the faculty and the time for the receiver to refill to full capacity. The minimum allowable receiver pressure during normal working hours was 6 MPa therefore allowing a receiver pressure drop of 4 MPa during tests. This pressure drop was extended to 6 MPa after working hours.

Two sets of preliminary tests were performed, each consisting of test runs at 60 000, 80 000 and 100 000 rpm with the number of operating points ranging from four to seven at each speed. The total test time for each set was 4 and 4.5 hrs respectively which included time spent on measurement (an average of 30 min) and refilling of the compressed air receiver which took 3.5 and 4 hrs. The rate at which the receiver refilled was dependent on its usage by other facilities. A sample rate of 10 S/s for a duration of 10 s was used. The number of measurements that could be taken during each test run was dependent on the rotational speed. On average three different test points could be measured at 100 000 rpm with a maximum of eight points at combined speeds of 60 000 and 80 000 rpm. The interval between each measurement ranged from 1 to 4 min.

For steady-state operation Brun and Nored (2006) suggests that the compressor be operated for at least 30 min to guarantee a complete heat soak. This is to ensure that the temperature probes can reach equilibrium. If not then steady-state conditions may be considered if readings have stabilised for an interval of at least 10 min prior to taking measurements. From the preliminary tests it was clear that the suggested heat soak time was infeasible but steady-state operation was achieved within the intervals between successive measurements. The 10 min interval also proved to be infeasible as the air receiver would need to be refilled more often and thereby extending the total test time.

On average the intervals between successive test points lasted 1.5 min during which the operating point was adjusted until the required mass flow had been attained and measured temperature stabilised. The steady-state conditions were verified from the telemetry displayed on the program GUI. As a general rule the test unit was set to idle at a speed of 20 000 rpm at the start and end of each test run for a period 3 min to 5 min. This was performed to ensure proper heat penetration and thermal equilibrium of the lubrication throughout the machine bearing and shaft assembly. For the actual test runs a total of four sets of readings were taken at each test point with a total of six test points at a constant speed to complete a performance curve. The test points were evenly spaced from choke to the onset of surge. The detailed testing procedure and check list is presented in Appendix F.

Following the completion of the test an uncertainty analysis was performed to validate the integrity of the measured data. From the theory of pooled statistics a better statistical estimate is obtained from the measured quantities by combining m replicated measurements of n samples per measured quantity. In determining the precision interval about the pooled mean a normal distribution with a student-t weighting of t_{99} was used. For a total of $m = 4$ replicated measurements each consisting of $n = 100$ samples, the distribution of each measured quantity about the pooled mean is given by (Figliola and Beasley (2006)):

$$x = \langle \bar{x} \rangle \pm t_{99,99} \langle S_{\bar{x}} \rangle \ (99\%) \tag{3.5.1}$$

where the pooled mean and pooled standard deviation of the mean are respectively defined as:

$$\bar{x} = \frac{1}{mn} \sum_{m}^{j=1} \sum_{n}^{i=1} x_{ij} \tag{3.5.2}$$

$$\langle S_{\bar{x}} \rangle = \frac{\sqrt{\frac{1}{m}\sum_{m}^{j=1} S_{x_j}^2}}{\sqrt{mn}} \tag{3.5.3}$$

For the calculation of the compressor performance the pooled average of each quantity was used. Regarding the temperature measurements, since four independent readings were taken at each station, the average of the pooled averages were used. The deviation between the individual temperature measurements at each station were all within the prescribed limit of accuracy shown in Table 3.3, thus there was no need to discard any of the values.

The stability of the compressor operation is determined by the fluctuation of the measurements when operating at steady conditions. Permissible fluctuations are provided by ASME PTC-10 and Brun and Nored (2006) shown in Table 3.3. The fluctuations referred to by the ASME PTC-10 codes are calculated as the difference between the minimum and maximum test sample divided by the sample average (Eq. 3.5.4). Fluctuations of three test points namely surge, best efficiency and choke are presented in §5.2.

$$\Delta F = \frac{100(x_{max} - x_{min})}{\frac{1}{n}\sum_{i=1}^{n} x_i} \tag{3.5.4}$$

Table 3.3: Compressor stability criteria.

Quantity	ASME	Brun
Inlet temp.	0.5 %	±1 °C
Outlet temp.	0.5 %	±1 °C
Inlet press.	2.0 %	±1 % of average value
Outlet press.	2.0 %	±1 % of average value
Speed	0.5 %	±10 rpm
Flow	0.5 %	±1 % of average value

Calculation of the compressor performance followed a refined method given in ASME PTC-10 for calculating the total conditions at the compressor outlet using air as an ideal gas. The effects of humidity as well as dry and wet bulb temperature were not accounted for as no sensors were installed to measure these quantities. The method is iterative and starts by letting the initial static temperature be equal to the measured temperature, $T_s = T_p$. Next the static properties of the air namely density (ρ), specific heat at constant pressure (C_p)

and ratio of specific heats (γ) are calculated at the compressor outlet using the ideal gas law and measured quantities of temperature and pressure. The specific heat at constant pressure was calculated as a function of temperature (Cengel and Boles, 2006);

$$\bar{C_p} = 28.11 + 0.1967 \times 10^{-2} + 0.4802 \times 10^{-5} - 1.966 \times 10^{-9} \tag{3.5.5}$$

Following that the absolute velocity and Mach number of the air is calculated. Where the Mach number exceeded 0.3 an average value of specific heat and specific heat ratio at the total and static temperatures were used. The total temperature is then calculated using Eq. 3.3.1 from which a new static temperature is calculated.:

$$T_s = \frac{T_t}{1 + \frac{(\gamma-1)M^2}{2}} \tag{3.5.6}$$

This new static temperature is compared to the initial value upon which the process repeated until an acceptable difference error was reached. The total pressure was then calculated from;

$$p_t = p_s \left[1 + \frac{(\gamma - 1)M^2}{2}\right]^{\frac{\gamma}{\gamma-1}} \tag{3.5.7}$$

The total conditions calculated using the method described refer to the location of the pressure measurement station at the compressor outlet which is located a distance of 300 mm from the outlet of the volute exit cone. To ensure the correct comparison of data between the experimental and numerical results, the total and static conditions at the volute outlet were calculated from the known data at the measurement stations using compressible adiabatic duct flow with friction (Fanno flow) (White, 2005). For this type of flow the cross-sectional area, stagnation enthalpy and mass flow remains constant except for momentum which is affected by fiction. The adiabatic assumption is substantiated by the fact that heat loss and addition to the outlet piping is reduced by the added insulation. Critical to this type of flow is the fluid Mach number which is to be calculated at the volute exit cone from which the total conditions at that point are determined. The governing equation relating the fluid Mach number and pipe friction is given by:

$$\frac{\bar{f}L^*}{d} = \frac{1 - M^2}{\gamma M^2} + \frac{\gamma + 1}{2\gamma} \ln \frac{(\gamma + 1)M^2}{2 + (\gamma - 1)M^2} \tag{3.5.8}$$

Usually the required pipe length needed to accelerate/decelerate flow to sonic conditions from known upstream conditions is determined from:

$$\bar{f}\frac{\Delta L}{d} = \left(\frac{\bar{f}L^*}{d}\right)_{upstream} - \left(\frac{\bar{f}L^*}{d}\right)_{downstream} \tag{3.5.9}$$

In this case the upstream conditions are to be determined therefore Eq. 3.5.9 is rearranged to:

$$\left(\frac{\bar{f}L^*}{d}\right)_{upstream} = \bar{f}\frac{\Delta L}{d} + \left(\frac{\bar{f}L^*}{d}\right)_{downstream} \tag{3.5.10}$$

Eqn. 3.5.10 is solved with the known pipe dimensions $(\Delta L, d)$ and the fluid Mach number at the plane of the outlet pressure measurement station. The result is then substituted into Eq. 3.5.8 and solved iteratively to obtain the Mach number at the volute exit. The total and static conditions are then solved by compressible flow ratio's. Sample calculations are presented in Appendix E.2.

Chapter 4

Numerical Simulation

4.1 Introduction

This chapter describes the modelling and simulation of the KKK K27 compressor. The CFD analysis was performed with NUMECA FINE™/Turbo v8.9-1 and FINE™/Open v2.11-2, the major difference being that Turbo solves structured and Open unstructured meshes. The FINE™/Turbo solver was selected as it is specifically suited for turbomachinery applications such as centrifugal compressors. The use of FINE™/Open was later included when it was necessary to analyse the impeller-volute interaction. The mesh generation and post-processing was done with modules included in the solver software; namely Autogrid5™ (structured grid generator), HEXPRESS™ (unstructured grid generator) and CFView™ (post-processing viewer).

4.2 Approach

A three-dimensional model of the impeller and volute was required for the numerical analysis. No geometrical data for the compressor was available, therefore the physical models of the impeller and volute (Figures 4.1a, 4.1b) had to be translated into three-dimensional CAD models.

Initially only the impeller and vaneless diffuser were simulated and were treated independently from the volute. The volute was later included to account for flow interaction between the impeller, diffuser and volute (Hagelstein *et al.*, 2000; Van den Braembussche, 2006). The approach followed in both analyses were similar except where an investigation into various impeller geometries were done, which was limited to the impeller-diffuser analysis. Firstly a computational grid validation was performed where the global parameters of pressure ratio and efficiency of three grid densities were compared. In addition the convergence and y_1^+ values were checked to see whether acceptable

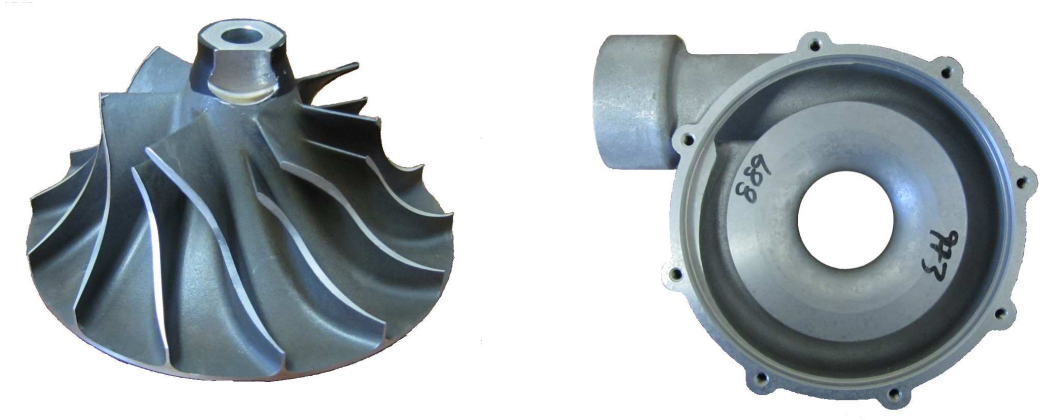

(a) Impeller rotor. (b) Impeller volute.

Figure 4.1: K27 compressor components.

levels have been achieved. Following the mesh validation, an investigation was done to determine the best impeller geometry to be used with the volute. Two areas of concern regarding this matter were identified; namely the hub fillet at the root of the blades and a small stepped gap between the interface of the impeller and diffuser. The impact of these features on the accuracy of the CFD results were investigated. Four different meshes were analysed of which one was selected for the impeller-volute analysis. Lastly performance curves of pressure ratio and efficiency were constructed with the selected mesh at the applicable rotational speeds and mass flows.

4.3 Impeller computation

This section describes the CAD and mesh generation of the impeller. Furthermore the parameters related to the numerical computation are also discussed.

4.3.1 Geometry

The geometric modelling of the compressor impeller was done by Van der Merwe (2012). A brief description of his modelling procedure is discussed. The grid generator requires a native *.geomTurbo file in which the impeller geometry is defined in order to generate a structured mesh of the computational domain. The *.geomTurbo file contains coordinate information about the hub, shroud and blade profiles as well as periodicity and inclusion of the splitter blades. Van der Merwe used a combination of data from geometric scans, various CAD software (Rhinoceros3D® and PowerSHAPE®) and custom code to digitally recreate the blade profiles of the K27 impeller. The meridional parameters and main blade specifications are presented in Figure

4.2 (dimensions in mm) and Table 4.1.

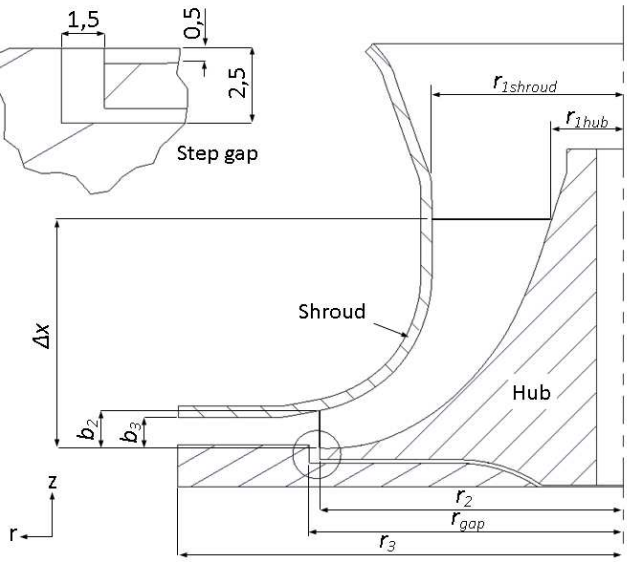

Figure 4.2: K27 impeller geometrical configuration and parameters.

Table 4.1: K27 geometrical parameters.

Blade number, Z	14
Inlet hub radius, r_{1hub}	10.1 mm
Inlet shroud radius, $r_{1shroud}$	25.5 mm
Inlet angles, β_{1hub}, β_{1tip}	58°, 30°
Outlet radius, r_2	40.4 mm
Blade height, b_2	5.0 mm
Outlet angle, β_2	30°
Step gap radius, r_{gap}	41.9 mm
Diffuser radius, r_3	59.4 mm
Diffuser passage height, b_3	4.0 mm
Axial length, Δx	28.8 mm
Tip gap, d_{tip}	0.45 mm

4.3.2 Computational domain

The computational domain of the CFD model starts at the inlet of the compressor and extends to the outlet of the vaneless diffuser, shown in Figure 4.3.

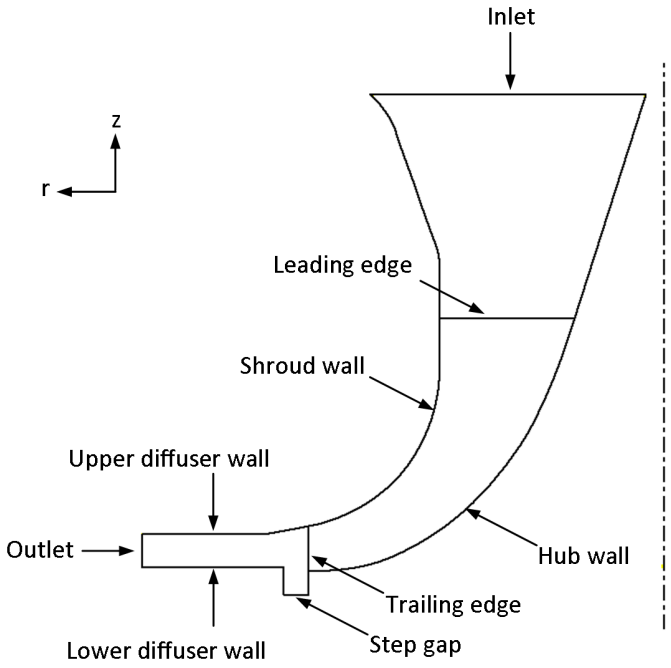

Figure 4.3: Meridional view of computational domain.

The inlet of the domain is located 20 mm upstream of the leading edge of the impeller main blade. This is roughly the distance at which the end of the compressor shaft is located. The inlet is modelled as a plane perpendicular to the z-axis. The impeller outlet is extended to include the vaneless diffuser section. The outlet of the domain is located at a constant radius r_3 which coincides with the outlet of the vaneless diffuser. The walls of the diffuser passage are parallel. The small stepped gap exists at the interface of the impeller outlet and diffuser inlet (r_2 to r_{gap}). This gap is a result of the manufacturing tolerances of the impeller backplate.

4.3.3 Mesh generation

The impeller mesh was generated using NUMECA's automatic structured mesh generator, Autogrid5™. Meshes are generated through conformal mapping between the three-dimensional Cartesian space and the cylindrical surface of the two-dimensional blade-to-blade space $(dm/r, \theta)$. Autogrid™ allows the user to choose the level of involvement in the mesh generation process by means of *Wizard* and/or *Expert* modes. The *Wizard* mode was used to create an initial mesh after which the quality was improved by fine-tuning parameters available in *Expert mode*.

The impeller was modelled as a single blade row consisting of one main and one splitter blade. By principle of symmetry the blade row is located about

the z-axis with a periodicity of 7. A constant tip gap of $d_{\text{tip}} = 0.45\,\text{mm}$ was specified from the leading to the trailing edge. In addition a hub fillet with radius of 1.85 mm was specified. The addition of a hub fillet complicated the meshing process as it had a negative effect on the mesh quality, resulting in orthogonalities lower than 20°. The mesh quality is discussed in §4.5. Because of the structured mesh philosophy adopted by Autogrid5™ the same number of cells on the shroud plane have to be accommodated on the hub plane (0 % span). The presence of a hub fillet reduces the blade-to-blade area at the hub plane. As a result the cells are 'squeezed' into this smaller area resulting in distorted cells especially at the blade leading edge shown in Figure 4.4a.

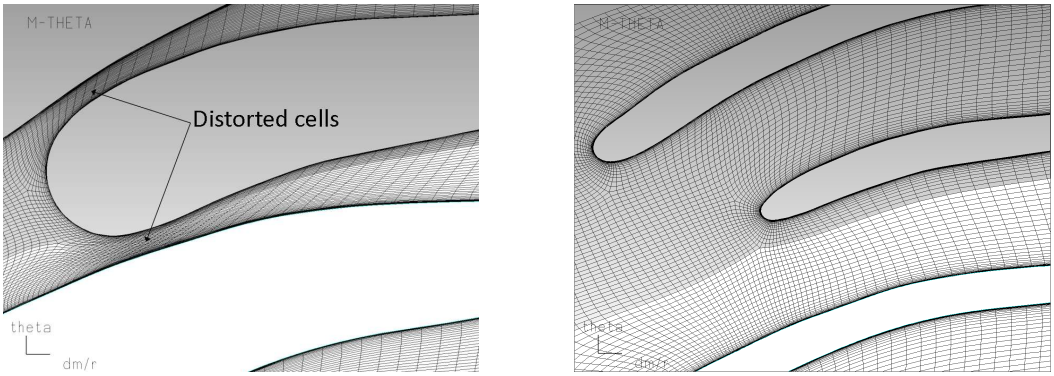

(a) Filleted. (b) Unfilleted.

Figure 4.4: B2B view of leading edge at 0 % span.

Following the initial blade row set-up, the meridional flow paths were created. These flow paths are created by projecting the surfaces of revolution i.e. the hub and shroud onto the meridional plane $(z - r)$. These flow paths are distributed along the blade height from root to tip and in the gap between the blade and shroud. The number of flow paths are defined by the spanwise grid points of which a default value of 73 grid points were used. The flow paths are shown in Figure 4.5.

In addition the wall cell width (y_{wall}) of the impeller surfaces was specified to ensure that the correct range of y^+ was attained on the impeller surfaces. The value for y_{wall} was calculated by using a truncated series solution of the Blasius equation for turbulent flows (NUMECA International, 2010*a*):

$$y_{wall} = 6 \left(\frac{V_{ref}}{\nu} \right)^{-7/8} \left(\frac{L_{ref}}{2} \right)^{1/8} y^+ \tag{4.3.1}$$

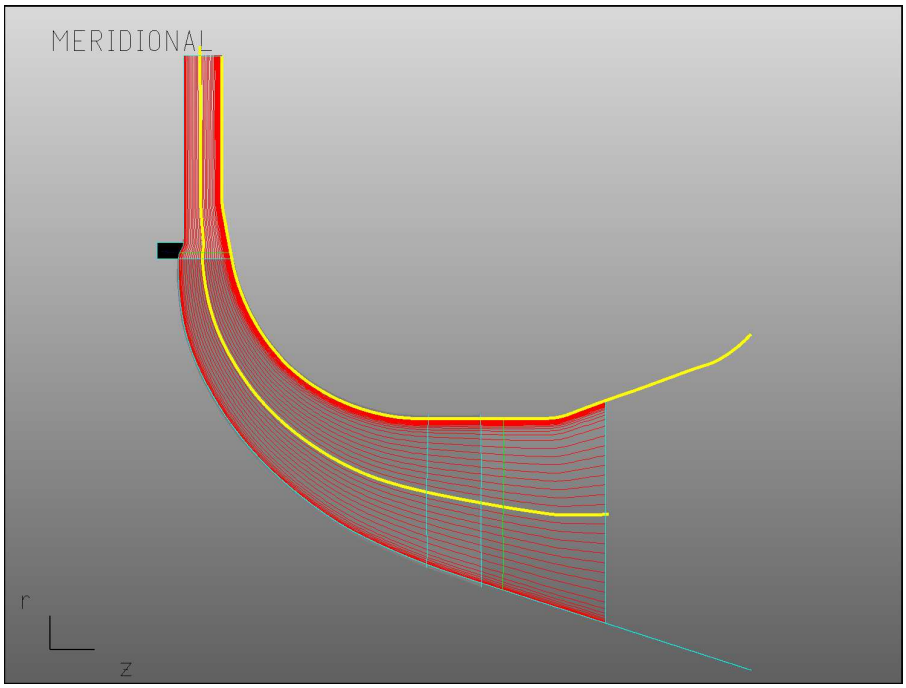

Figure 4.5: Flowpath layers in the meridional view.

Where the reference velocity V_{ref} was taken as the average inlet velocity, the reference length L_{ref} was calculated from the meridional blade length. For low-Re turbulence models a y^+ value ranging from 1-10 is desired (NUMECA International, 2010*a*; Versteeg and Malalasekera, 1995). The wall cell width was calculated such that a y^+ close to 1 could be achieved.

In the following step blade-to-blade meshes are created in the $(dm/r, \theta)$ space, by projecting two-dimensional meshes on the flow path surfaces of the meridional plane. This is an important step as the mesh quality is greatly affected by the changes made in the bade-to-blade space. The number of grid points in the blade-to-blade mesh is specified by selecting a desired grid level. An initial grid level of -7 equated to a total number of 1 040 860 grid points. This changed due to the modification of the blade-to-blade mesh topology.

An H&I topology was used which is well suited for multi-blade purposes such as a compressor impeller with splitter blades. The area around each blade is described by four blocks namely an Inlet-, Outlet-, H- and Skin-block, which constitutes the H&I topology (Figure 4.6). The blue lines indicate the block boundaries. The Inlet block is preceded by an extra Inducer block to account for the inlet section of the computational domain. It has 29 grid points in the streamwise direction. The Outlet block is extended with an extra Discharge block to account for the vaneless diffuser outlet and has 21 grid points in the streamwise direction.

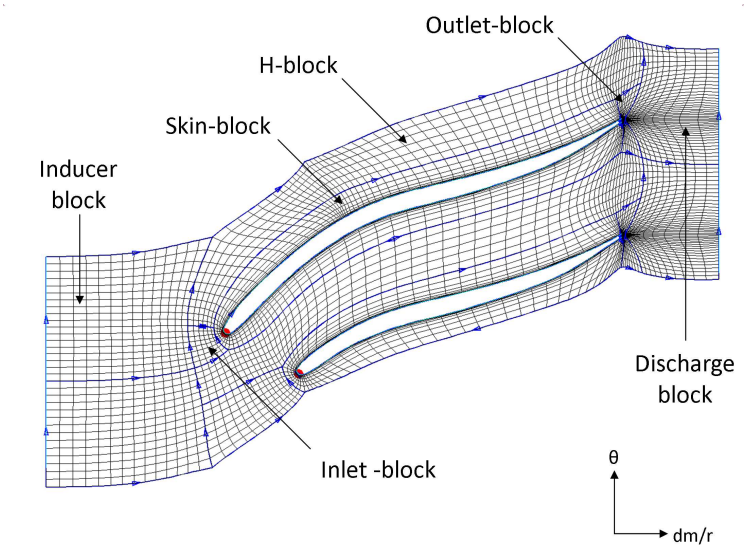

Figure 4.6: Blade-to-blade view of the main and splitter blade (grid level 2).

By adjusting the number of nodes of the mesh blocks the number of cells in the final three-dimensional mesh could be altered. Subsequently this had an effect on the mesh quality and therefore had to be done carefully. The final blade topology showing the number of node points of the main and splitter blades are shown in Figures 4.7 and 4.8.

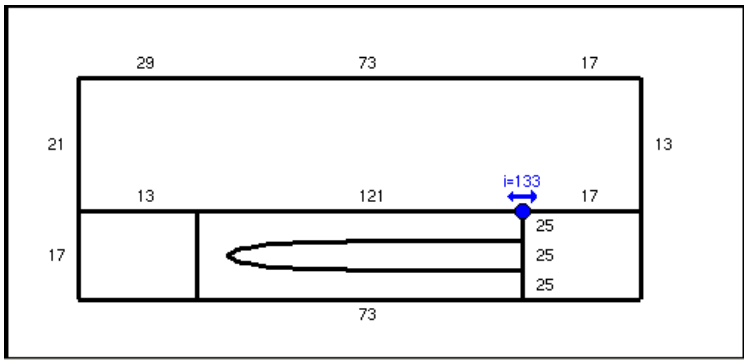

Figure 4.7: Mesh grid points of main blade topology.

In order to replicate the step gap found at the interface of the impeller and diffuser, a *z-r effect* was added to the computational domain. The interface between the rotating impeller and step gap was a full non-matching periodic interface which was modelled as a volume consisting of 7 periodic sections.

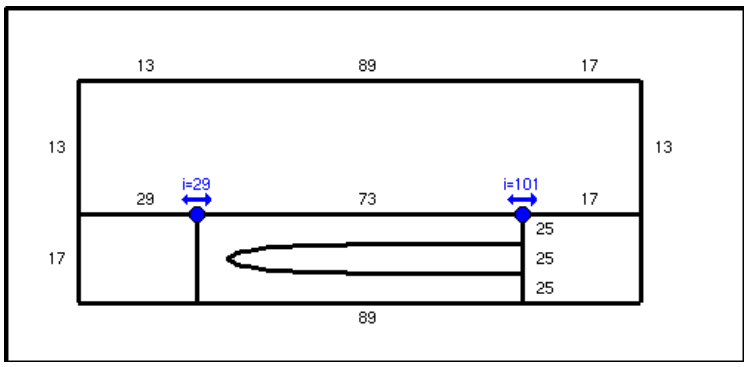

Figure 4.8: Mesh grid points of splitter blade topology.

The meridional mesh of the step gap is shown in Figure 4.9.

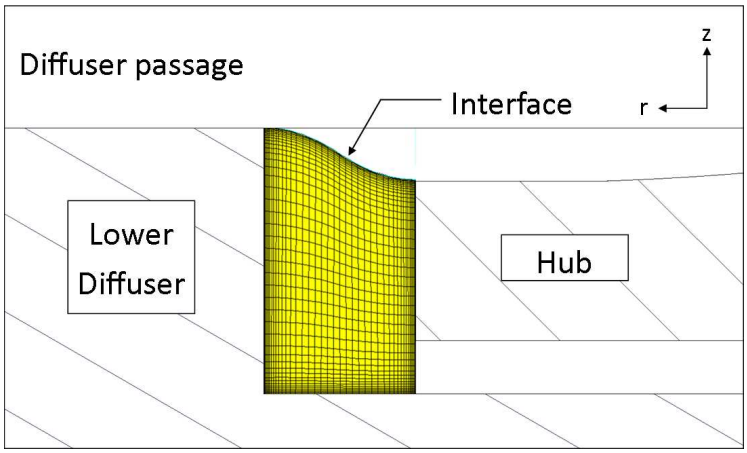

Figure 4.9: Meridional view of the step gap mesh.

Once all the mesh parameters in the previous steps were set and an acceptable blade-to-blade mesh quality achieved, a three-dimensional mesh was generated. The three-dimensional mesh is created by stacking the blade-to-blade meshes onto the surfaces of revolution created by the flow paths. The final mesh consisted of 1 846 597 cells divided into 17 blocks. For an impeller of similar size and performance to the K27, the total number of cells is consistent with the studies by Ling *et al.* (2007) and Kim *et al.* (2011) where the investigation of secondary flows are not important and thus fall outside the scope of this project. Figure 4.10 shows a single blade row of the final three-dimensional mesh.

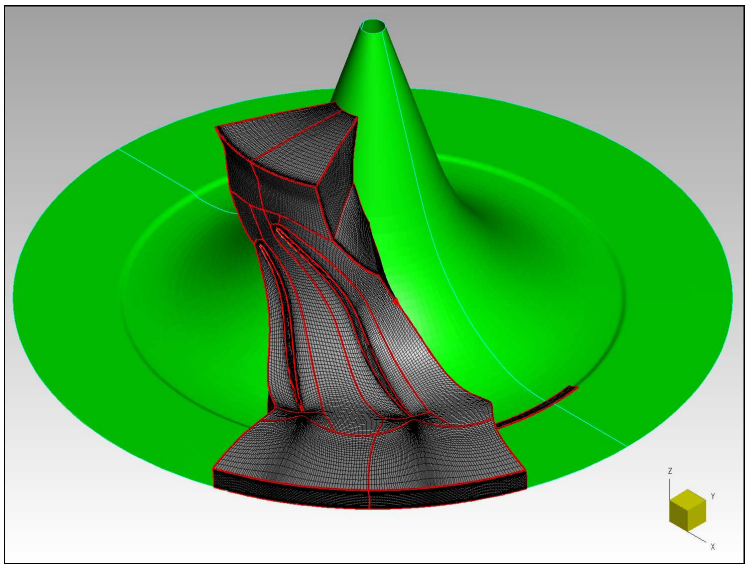

Figure 4.10: Three dimensional block mesh of the K27 compressor impeller (single blade row).

4.3.4 Computational parameters

This section describes the various parameters pertaining to the physical configuration, boundary conditions, numerical schemes, etc. of the computational parameters for the impeller mesh.

4.3.4.1 Physical configuration

Fluid model The selected *working fluid* was atmospheric air which was modelled as a real gas. The real gas model is more thermally precise than a perfect gas since the quantities C_p and γ are dependent on temperature.

Flow model The experimental measurements were conducted under steady-state conditions and the computational flow model was specified accordingly. The *flow solver* of choice was the Turbulent Navier-Stokes solver. In numerous studies involving CFD analyses of centrifugal compressors a three-dimensional Reynolds-averaged type Navier-Stokes solver was utilised, either commercial or in-house, (Benini and Giacometti, 2007; Hagelstein *et al.*, 2000; Kim *et al.*, 2011; Van der Merwe, 2012).

Characteristic values of length, velocity and density were used to estimate the Reynolds number of the flow which provided useful information in choosing the appropriate *turbulence model*. The length is defined as the camber length of the main blade and the velocity as the compressor average inlet velocity. The density was calculated from a reference temperature and pressure of 289.5 K and 100.5 kPa respectively which corresponded to the average at-

mospheric conditions for the duration of the experimental tests. Regarding the choice of turbulence model, numerous models have been used for various geometries and operating conditions. Zangeneh *et al.* (2004) and Ling *et al.* (2007) both utilise the Standard $k-\epsilon$ model. Zangeneh *et al.*'s impeller is of an industrial size where as Ling *et al.*'s is small scale. The impeller rotational speeds were 21 218 rpm and 120 000 rpm respectively.

Van der Merwe (2012) compared four different turbulence models namely the Baldwin-Lomax, Spalart-Allmaras, $k-\epsilon$ and $k-\omega$ models. From his results he found that deviations in the resulting pressure ratios and efficiencies at the domain outlet did not exceed 3%. Both the Baldwin-Lomax and Spalart-Allmaras are low-Re models and therefore require a well resolved grid near the wall. These models are well suited for high speed flows with thin boundary layers and are thus typically used in aerospace and turbomachinery applications. Van der Merwe (2012) also found that the two-equations models ($k-\epsilon$ and $k-\omega$) took longer to reach convergence. He finally selected the Spalart-Allmaras model. Krige (2012) used the Spalart-Allmaras turbulence model in his study in which he used an impeller of a similar size and performance. Based on these findings the Spalart-Allmaras model was the selected turbulence model.

Rotating machinery The configuration of the rotating machinery only required the definition of the rotational speed. The impeller was simulated at three rotational speeds, namely −60 000, −80 000 and −100 000 rpm. The rotational speed is specified with a negative sign to ensure that the impeller rotates in the correct direction about the z-axis. This is due to the orientation of the impeller geometry in relation to the global coordinate system.

4.3.4.2 Boundary conditions

The computational domain consisted of four boundary groups, namely the inlet, outlet, periodic and solid wall boundaries. The boundaries are automatically defined in the *geomturbo file, however the conditions at those boundaries had to be specified. In keeping with the axis convention all the boundary conditions are specified in cylindrical coordinates.

Inlet boundary As mentioned in §4.3.2 the inlet boundary plane is located 20 mm upstream of the leading edge of the main blade and perpendicular to the z-axis. The assumption is made that flow is purely axial (negative z-direction) at the inlet during experimental testing. No pre-whirl was induced without any major disturbances. The flow is constrained by selecting the *V-extrapolated* velocity direction. The flow is constrained in the axial direction i.e. perpendicular to the inlet boundary plane, by setting the velocity components in the V_z, V_r, V_θ directions. In addition total quantities of pressure and temperature

were imposed at the inlet boundary, which corresponds to the test conditions. The inlet conditions are shown in Table 4.2:

Table 4.2: Inlet boundary parameters.

Property	**Value**
(|Vr|\V)	0
(|Vt|\V)	0
(|Vz|\V)	−1
Absolute Total Pressure	100.5 kPa
Absolute Total Temperature	289.5 K
Turbulence Viscosity	0.0001 m^2/s

Outlet boundary The outlet boundary plane is located at the outlet of the vaneless space at radius r_3. It extends the entire blade height from the hub to the shroud and is parallel to the z-axis. For the outlet boundary a *subsonic mass flow* condition was imposed. For the low rotational speeds, 60 000 and 80 000 rpm, a *velocity scaling* condition was applied while a *pressure adaptation* condition was applied to the 100 000 rpm. The velocity scaling condition ensures that the imposed mass flow is attained at the outlet by scaling the velocity vectors. In the same way the pressure adaptation condition automatically modifies the outlet pressure such that continuity is maintained. A static pressure is required as an initial value for the full multigrid process which is then extrapolated during each subsequent grid level computation. Another treatment known as *backflow control* was used to control the distribution of total temperature along the outlet plane. This occurs in the case of a radial diffuser as found in the KKK K27, where the flow could re-enter the domain. The re-entering and exiting flows are adjusted to have the same global total temperatures.

Periodic boundary conditions The periodic and connecting boundary conditions were automatically set by the grid generator and the corresponding information was transferred to the solver, therefore no user input was required.

Solid wall boundaries The Navier-Stokes flow model allows thermal and velocity conditions to be defined at the solid wall boundary. The solid boundary was divided into two groups namely; rotating and stationary. The rotating group consisted of the hub, main and splitter blade surfaces while the stationary group consisted of the shroud and step gap surfaces. The thermal condition of the solid boundaries were set as adiabatic. A constant wall rotation velocity was selected for both solid boundary groups with 0 and 60 000 rpm

to 100 000 rpm for the stationary and rotating groups respectively. The pressure was set to be calculated from extrapolation. In addition torque and force values were also calculated on the rotating surfaces.

4.3.4.3 Numerical scheme

The timing configuration has already been discussed in §4.3.4.1. The numerical model defines the numerical aspects of the computation which include the choice of spatial discretisation, CPU (Central Processing Unit) booster, CFL (Courant-Friedrichs-Lewy) number and multigrid parameters. For this computation the default *central* spatial discretisation scheme with a *2nd-order* accuracy was selected. The CPU booster was not activated since it is not compatible with the real gas model. The CFL number was kept at a standard value of three.

FINE™ implements a multigrid method, known as *coarse grid initialisation* to accelerate convergence. It essentially increases the coarseness of the mesh by a process of agglomeration to obtain various grid intensities known as grid levels. The maximum number of grid levels are dependent on the size of the finest mesh and is automatically determined. The user does however have control of which grid level the solution must be solved from. Furthermore the number of iterations performed on each multigrid level could also be specified. Faster convergence of the final solution was achieved by solving the flow problem on each subsequent grid level by using the solution from a previous grid level as an initial solution to the current grid level being solved. The mesh created in AutoGrid5™ is the finest level i.e. a multigrid level of (0 0 0). The values indicate the number of times the grid can be coarsened in each of the grid (i,j,k) coordinate directions. The K27 mesh could be coarsened a maximum of three times, i.e. a grid level of (2 2 2). The multigrid method was used to obtain solutions at the best efficiency point (BEP) of all three speeds. Thereafter the solutions at other operating points of the same speed were solved only on the finest grid level. Further details regarding this matter is discussed in the following paragraph.

4.3.4.4 Initial solution

For the simulations in which the BEP were determined, the initial solution *'for Turbomachinery'* was chosen. This configuration caters specifically for cylindrical rotating machinery by conserving rothalpy along the streamlines of the meridional plane. An estimated static pressure of 100 kPa at the inlet was defined for all three rotational speeds. Other operating points were specified sequentially from the BEP to the surge and choke points. The initial solution for the points other than the BEP were specified from file, which means that a current computation was initialised with the results from a previous compu-

tation. This was also applied when mapping the compressor curves with the *performance curve* module which is discussed later.

4.3.4.5 Output values and computational steering

The output parameters of greatest interest were those that may be compared with the experimental results such as the total and static pressures and temperatures. Furthermore absolute and relative velocities, absolute Mach number and y^+ quantities were selected. The convergence of a solution was subjected to the following criteria (NUMECA International (2010*b*)):

1. An adequate decrease in global residuals (at least 3 orders of magnitude)
2. Stabilisation of the global parameters (at least 100 iterations)
3. A difference error of $< 0.5\,\%$ between the inlet/outlet mass flow

The parameters that were monitored during a simulation were the global residuals, pressure ratio, efficiency and the difference between inlet and outlet mass flows. For the BEP a total of 2000 iterations was sufficient to reach convergence on the finest grid level. The number of iterations at the remaining points varied from 400 to 600 with the latter being chosen closer to the regions of surge and choke where the solution reached the limits of stability and therefore needed more iterations to reach convergence. In some cases a difference error between the inlet and outlet mass flow of as little as $0.004\,\%$ was achieved.

4.3.4.6 Performance curve

A compressor map of the K27 impeller was created with a *performance curve* module dedicated to turbomachinery applications. This module allows the user to perform complete performance curve evaluations with minimal user interaction and accelerates the simulation process by automatically configuring simulations in the stall and choke regions from a specified design point. A design point was specified from which the curve is mapped in the surge and choke directions. The points in the surge and choke directions could either be specified as a percentage of the design point outlet static pressure or mass flow.

For the K27 impeller, the BEPs of all three speeds were specified as the design point. Initially a total number of 15 points (the sum total of the design, surge and choke points) were selected, which extended from the onset of surge to total choke conditions. The number of points in the surge and choke regions varied according to the position of the BEP in relation to the critical surge and choke conditions and were chosen in such a way as to obtain a curve with evenly spaced points. A stall condition in the context of the simulations was

defined as an oscillating variation presented by the mass flow, which shows no sign of stabilising with an increase in iterations. A choke condition is intuitively defined by the fact that no further increase in mass flow is possible at a certain operating point and coincides with a sudden drop in efficiency. Practically it was decided to simulate choke from the BEP until an isentropic efficiency in the region of 60 % was reached. This practice agrees with that implemented by Kim *et al.* (2011) and Van der Merwe (2012).

4.4 Impeller-volute computation

This section describes the CAD and mesh generation of the combined impeller and volute. In addition the parameters utilised in the numerical computation are presented.

4.4.1 Geometry

HEXPRESS™ uses a native *.dom file to generate an unstructured mesh of the computational domain. It accepts three CAD formats from which the computational domain can be created. In this instance the Parasolid™ format (*.x_t) was used. HEXPRESS™ requires the computational domain to be described as a single closed volume. It was important for the model to be "watertight" so that the entire surface model was without any discontinuities. The domain was created by converting the imported Parasolid™ to a domain. The *.dom file, which is a triangulated representation of the CAD model, stores information about the topology and geometry of the computational domain. The volute geometry was obtained by means of Stereolithograpy (STL) scans, illustrated in Figure 4.11.

Geometric scans The volute was scanned at the Rapid Product Development (RPD) Laboratory, Industrial Engineering Department, Stellenbosch University, with the help of Mr P. Hugo of the Institute of Advanced Tooling (IAT). The geometry of interest was the volute cavity which collects the flow exiting the impeller. The Atos1 3D digitiser from GOM™ industries was used to scan the volute. A detailed description of the use of the Atos1 is presented in the thesis of Van der Merwe (2012). An area of concern regarding the capturing of the geometry was the inner wall of the volute cavity (Figures 4.12a and 4.12b) which is situated beneath an undercut created by the presence of the upper diffuser wall. The radius of the undercut increases gradually in a circumferential direction from the tongue to the exit cone. This radius varies from barely nothing to being most prominent between 225° and the tongue intersection.

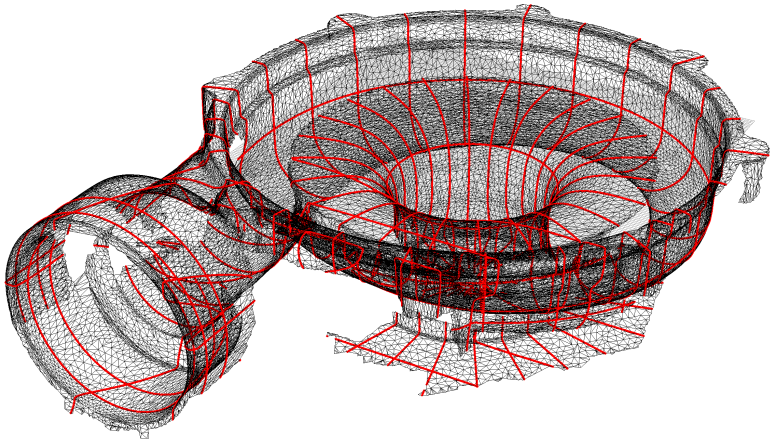

Figure 4.11: Stereolithography scan of the K27 volute.

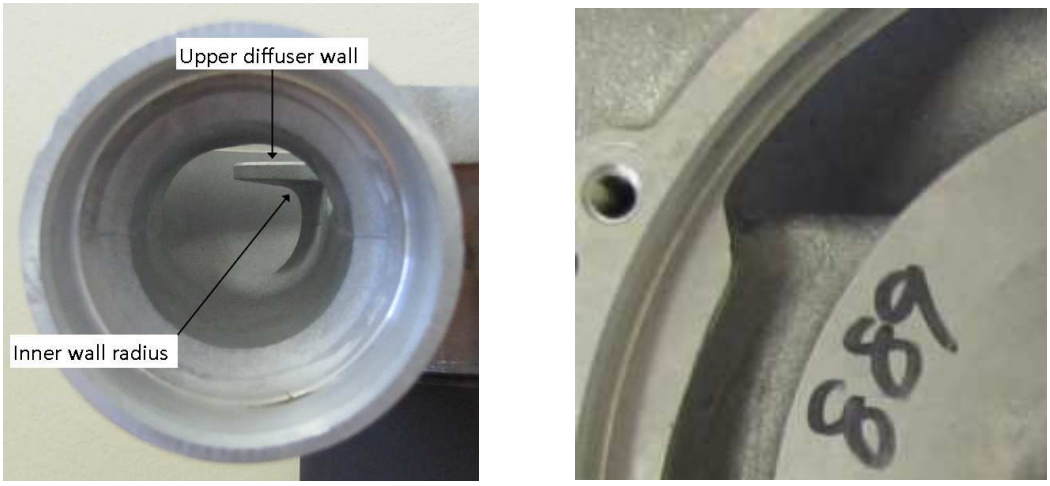

(a) Volute cavity inner wall.

(b) Volute tongue detail.

Figure 4.12: Problematic volute geometry.

The GOM™ scanner captured the entire cavity where possible, but due to geometrical constraints it could not capture the inner wall accurately enough. It was therefore decided to simplify this part of the volute geometry by omitting the radius at the undercut of the inner wall, thereby creating a sharp edge (see Figure 4.15). During post-processing the geometry was cleaned and a reference coordinate system added. The origin was placed parallel to the plane of the upper diffuser wall in the centre of the volute inlet with the positive z-axis pointing upward from the inlet. Twelve cutting planes were added about the z-axis in increments of 15°. These planes provided circumferential cross-section profiles which were used to reconstruct the volute cavity, (Figure 4.11).

CAD model The CAD software used to model the volute cavity was Inventor® Professional (Autodesk, 2012) and PowerSHAPE® (Delcam, 2012). As mentioned previously, it proved difficult to accurately measure the inner wall profile of the cavity. The profile of the curved part of the wall was approximated by superimposing arcs on the profiles of each of the twelve cutting planes. Most of the remaining geometry remained uniform except at the tongue region and from the full-collection plane to the outlet. Finally a surface loft was created by joining the closed profiles from 0° to 360° to create the spiral shape. A separate surface loft was created for the straight section from the full-collection plant to the volute outlet.

Once the general shape was defined, the model was refined using PowerSHAPE®. In PowerSHAPE® the model was manipulated into an accurate wire-frame model of the cavity. Next the wire-frame was covered with surface patches to form three separate "watertight" volumes. The tongue intersection was modelled in greater detail by creating a finer grid of closely spaced profile cuts which were covered with surface patches. Figure 4.13 shows an enlarged area of the tongue region in which the GOM™ scan (red and purple) and modelled volute (grey) are compared. From a visual inspection good agreement can be seen between the scanned and modelled surfaces.

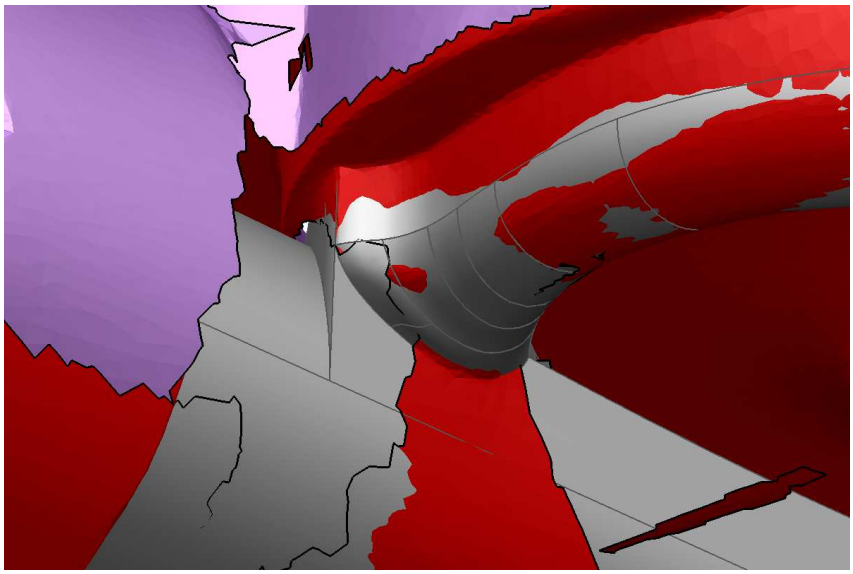

Figure 4.13: Tongue region of the volute.

After the creation of the closed surface volumes they were transformed into individual solid blocks and merged to form a single solid. The final solid model is shown in Figure 4.14.

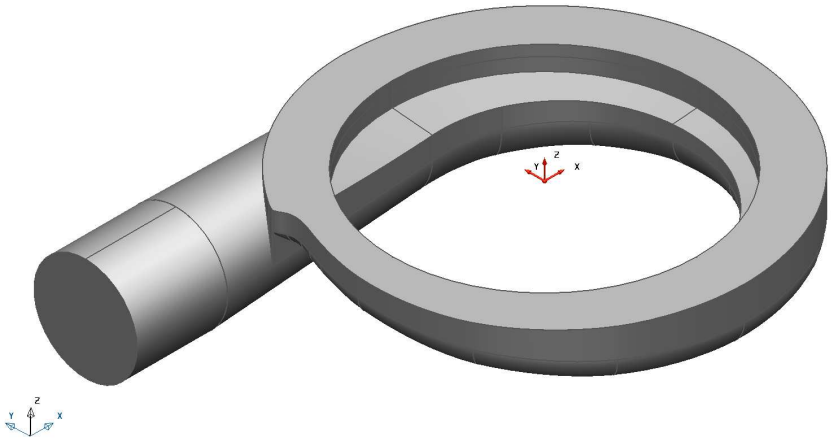

Figure 4.14: Final solid model of compressor volute.

Figure 4.15 shows the cross-sectional profiles of the volute (dimensions are in mm). The flow area is indicated by the hatched pattern. The simplification of the geometry can clearly be seen, namely the sharp edge on the inner wall radius and the circular arcs of the cavity wall. The diffuser outlet and full-collection plane radii are indicated at r_3 and r_{fcp} respectively.

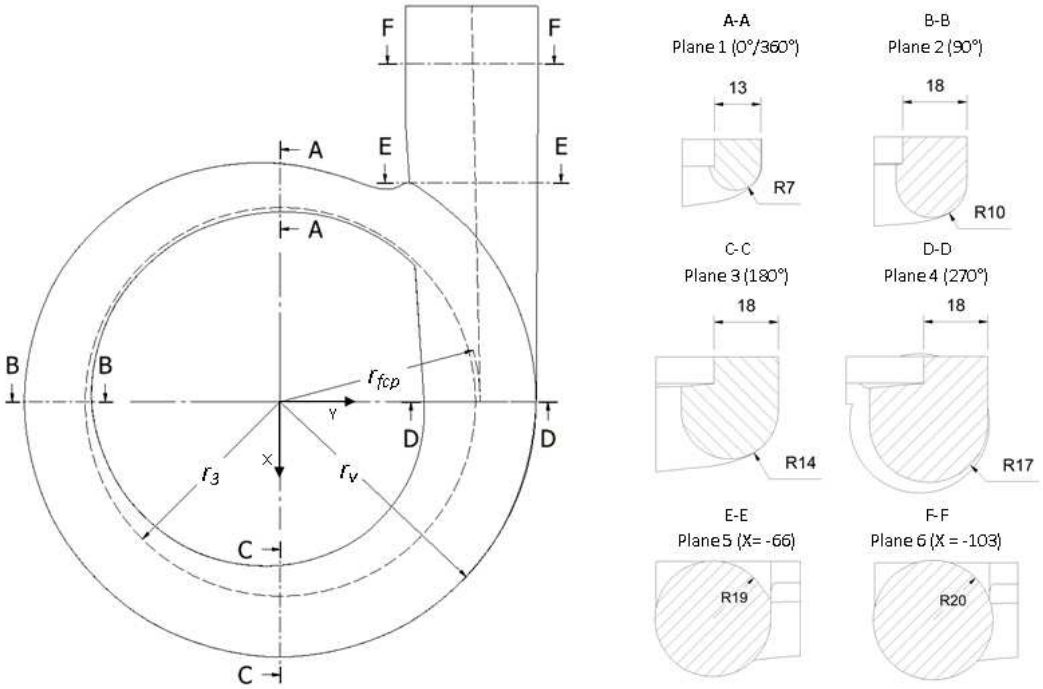

Figure 4.15: Cross-section profiles of volute.

4.4.2 Computational domain

As mentioned in §4.4.1 the *.dom file consists of a topology and geometry part. The topology defines the model as a closed volume in the form of a skeletal framework and provides information on the connection of faces, edges and vertices. The geometry part defines the actual geometry of the model where the faces, edges and vertices are described by triangulation. The faceting parameters and discretised domain are presented in Appendix G.2. The next step was to simplify the discretised domain by retaining entities representing real features or those that may have a significant effect on the flow. This was achieved by merging edges and face entities with a specified minimum angle between them, thereby reducing the total number of edges and faces comprising the domain.

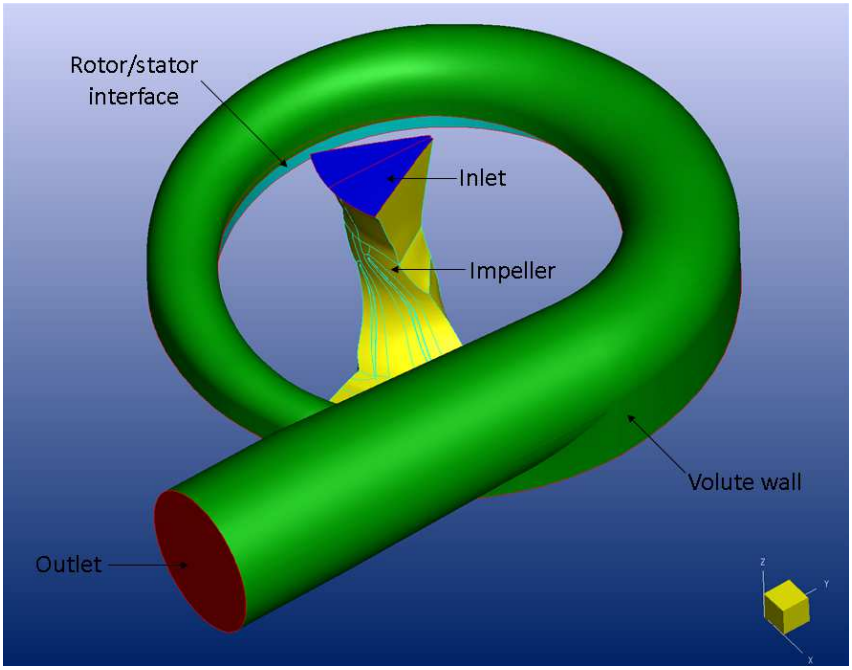

Figure 4.16: Computational domain of the impeller-volute.

The computational domain of the combined impeller and volute retained the same inlet boundary but included a new rotor/stator interface and outlet boundary definition. The domain through the impeller remained unchanged up to the diffuser outlet boundary. Initially the volute inlet boundary was defined on the same plane at a constant radius r_3, however with the inclusion of the impeller domain this boundary was redefined as a rotor/stator interface to account for the flow transition from the rotating to the stationary domain. The walls of the volute cavity correspond to the geometric scans. The outlet

boundary is located at the exit of the volute exit cone and oriented perpendicular to the x-axis. The computational domain is illustrated in Figure 4.16. The specific boundary conditions are discussed in §4.4.4.2.

4.4.3 Mesh generation

HEXPRESS™ is well suited for complex geometries such as a centrifugal compressor volute and uses a step-wise top-down approach to generate high quality meshes.

Initial mesh An initial mesh was created to encompass only the computational domain of the volute. The addition of the impeller mesh is described at a later stage. A bounding box was created by subdividing the domain into equally sized rectangular elements (isotropic cells), the number of which could be specified in each axis direction. The mesh consisted of 9672 cells with $x = 31$, $y = 39$, $z = 8$ cells in the respective axis directions. Good practice suggests to fill areas of less importance with larger cells, and vice versa for areas experiencing larger pressure or velocity gradients. This is important for the analysis of secondary flows such as the strong vortex flow pattern present at the centre of the volute cross-section (Hagelstein *et al.*, 2000). However secondary flow analysis is of less importance to the goals of this study and therefore the size of the initial mesh was considered.

Mesh adaptation Following the generation of an initial mesh it was refined, whereby cells are successively subdivided in one or several directions until a specific geometrical criteria was met. This ensures that the geometry is more accurately represented by the mesh. Four methods exist in which cells may be adapted, namely: Global, Curve, Surface and Box adaptation. In this instance the first three methods were utilised.

The adaptation process was regarded as a critical part of the grid generation process as it had a significant influence on grid quality. The final parameters were obtained through an iterative process. For the Global adaptation a maximum number of three refinements were specified. For Curve adaptation the curve describing the volute outlet was subjected to the Curvature and Target cell size criteria. A maximum number of three refinements were applied. For Surface adaptation all the volute surfaces were selected except for the outlet and inlet (later changed to rotor/stator interface) surfaces. The selected surfaces were also subjected to Curvature and Target cell size criteria. All advanced parameters were kept at the default settings.

Geometry snapping After the adaptation process the majority of the volute body was described by the mesh, except for lower dimensional features such as corners and curves. HEXPRESS™ applies an algorithm to recover these features by projecting the mesh onto the geometry surface. Additional cells are inserted to ensure the mesh conforms to the domain geometry. Mesh smoothing is also applied which moves node points on the surface and within the volume. Mesh snapping parameters were kept at the default settings.

Mesh optimisation After the mesh snapping was completed, the mesh was *optimised* to ensure that any poor quality cells (concave or negative cells) generated during the snapping procedure were converted to convex ones. Through a process of trial and error the following expert parameters were adjusted to obtain the best possible mesh quality. The maximum number of external optimisation loops was increased to 5 and the maximum number of orthogonality optimisation loops and minimal orthogonality threshold were increased to 5 and 20° respectively.

Viscous layer insertion The *viscous layer insertion* process adopted by NUMECA™ to accurately resolve boundary layers, relies on the successive subdivisions of the cells connected to the walls. This is contradictory to other methods which insert layers by way of extrusion from the wall. The viscous layers insertion is controlled by setting Global and individual Surface parameters. A first layer thickness and stretching ratio can be specified to control the thickness of the first layer and thickness ratio of each successive cell normal to the wall. The method of viscous layer insertion can also be chosen, either by way of a fixed or variable first layer thickness. In this case the fixed method was chosen.

The method used in the estimation of the wall cell width of the impeller mesh was applied to the volute. The aim was to achieve global y_1^+ values between 1 and 10. The majority of the y_1^+ distribution is expected to be greater than that of the impeller as the flow velocity decreases with the area change throughout the volute. The first cell width and stretching ratio was applied to all surfaces of the volute. These were applied in the Global parameters. The number of viscous layers varied from surface to surface. The number of layers is calculated empirically by the software based on the first layer thickness and stretching ratio. These were applied in the Surface parameters. Initial simulations were carried out to determine the correct first cell width which resulted in a first cell width equal to that of the impeller mesh of $y_{\text{wall}} = 1\times10^{-5}$. After the viscous layers were inserted the total number of cells for the volute mesh was 904 469.

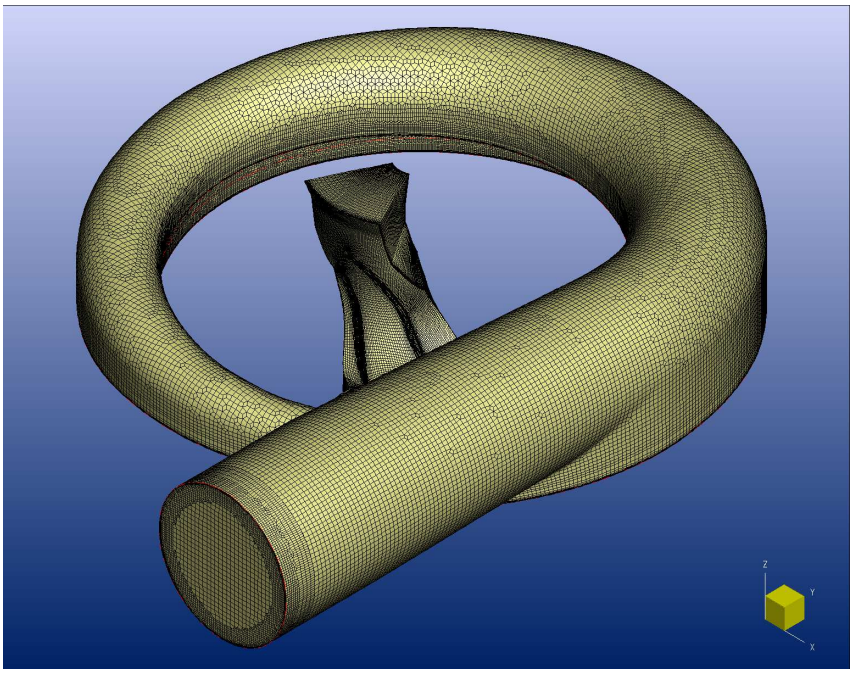

Figure 4.17: Final mesh of the impeller-volute.

Impeller mesh consolidation The final mesh was created by combining the volute and impeller meshes, (Figure 4.17). This automatic process involved the conversion of the impeller from a structured to an unstructured mesh as well as a the definition of a new boundary condition. The impeller mesh was converted on the finest gird level (0 0 0). The final combined mesh consisted of 2 747 087 cells. For the new boundary condition a rotor/stator connection was defined between the impeller and volute at constant radius r_3. A full non-matching boundary (FNMB) connection was defined on this plane which is the interface of the impellers periodic outlet and volute inlet patches. The FNMB connection is automatically calculated and was subject to geometric tolerances between the respective patches.

4.4.4 Computational parameters

Similarly to §4.3.4 this section describes the various parameters pertaining to the physical configuration, boundary conditions, numerical schemes etc. of the computation parameters for the impeller-volute mesh.

4.4.4.1 Physical Configuration

Fluid model From the project specifications provided by Snedden (2010) and the study done by Smith (2010) it was estimated that there would be a temperature difference across the compressor ranging between 130 °C to 205 °C

which equates to a 3 % change in C_p value. On comparing the use of the real and perfect gas model at the 60 000 rpm BEP, it was found that the real gas model was computationally more expensive (600 extra iterations) with only a 0.3 % and 1.0 % difference in pressure ratio and efficiency respectively. For this reason the air was modelled as a perfect gas.

Flow model The same flow and turbulence models were used for the impeller-volute computation, namely Turbulent Navier-Stokes and Spalart-Allmaras. Furthermore the use of the Spalart-Allmaras turbulence model for the unstructured grid is substantiated by Blazek (2001).

Rotating Machinery The configuration of the rotating machinery included both the volute and impeller domains. The same rotating speeds were specified as in §4.3.4.1. As mentioned previously a full non-matching mixing plane was chosen for the treatment of the rotor/stator connection and is a typical choice for steady-state computations. With this approach the flow solution at the interface is azimuthally averaged and the exchange of the information at the interface is dependent on the local direction of the flow. The advantages of this approach includes a single geometric constraint which requires that the rotor/stator patches of the interface lie on the same axisymmetric surface and exact conservation of mass, momentum and energy is guaranteed (NUMECA International, 2011). This treatment also requires a single blade row to be meshed, regardless of the periodicity. The flow direction was specified as moving from right (upstream) to left (downstream).

4.4.4.2 Boundary conditions

The computational domain of the volute-impeller domain consisted of three boundary groups, namely the inlet, outlet and solid boundaries. As with the impeller domain (§4.3.4.2) all boundary conditions were treated in cylindrical coordinates.

Inlet boundary The definition of the inlet boundary remained identical to impeller computation defined in §4.3.4.2.

Outlet boundary With the addition of the volute, the outlet boundary is located at the outlet of the volute exit cone. The outlet boundary is parallel to the z-axis and circular with a diameter of $d_{vo} = 40\,\text{mm}$. The same conditions at the impeller outlet boundary (§4.3.4) were applied to the volute outlet boundary. The required initial static pressure was slightly higher to account for the static pressure recovery through the volute.

Solid wall boundaries The solid boundaries were divided into two groups; stationary and rotating. The stationary group included the volute domain and impeller shroud patches. The rotating group included the impeller hub, blade (main and splitter) and FNMB patches. The rotational speed and thermal conditions were kept identical to those described in §4.3.4.2. Parameters affecting turbulence at the wall such as wall-type remained unchanged.

Initial solution The initial solution of both domains were specified from constant values in the cylindrical coordinate system. The initial solution for the impeller domain remained the same with the exception of the initial velocity. The velocity type was specified as relative with the respective velocity components V_r, V_θ and V_z all set to $0\ m/s$. For the volute domain the estimated initial static pressure coincided with outlet static pressure obtained from the initial impeller computations. The velocity type was specified as absolute with the velocity components V_r, V_θ and V_z equal to the outlet velocity components of the impeller simulation. The outlet static pressure and absolute velocities were obtained from the initial impeller computations.

4.4.4.3 Numerical scheme

The same spatial discretisation scheme and accuracy was used as in the impeller computation. With the multigrid method activated the mesh could be coarsened a maximum of four times. The maximum number of cycles per grid level was set to 400 with an absolute convergence level of -6.

4.4.4.4 Output values and computational steering

The output quantities and convergence criteria remained unchanged for the volute-impeller computation. Not all convergence criteria could be successfully met. At 100 000 rpm the difference between inlet and outlet mass flows were as high as 0.9 % near choke. All other convergence criteria were met.

4.5 Mesh validation

The validity of the computational grids were ensured by assessing the mesh quality, y^+ values and grid independence.

Mesh quality De Wet *et al.* (2010) gives the most important quantities defining a good quality mesh namely *Orthogonality*, *Aspect* and *Expansion ratios*. The mesh qualities along with the respective criteria are presented in Table 4.3. For the unstructured impeller-volute mesh the quality criteria were obtained from correspondence with the NUMECA™ software support group (NUMECA Software Support Group, 2012). Included in the table are the

worst values achieved and the percentage of bad cells in relation to the total number of cell in the mesh. The mesh quality for both grids were considered satisfactory.

Table 4.3: Mesh quality results.

Quantity	Criteria	Worst value	%Bad Cells
Impeller			
Orthogonality	$> 20°$	20.34°	0.00 %
Aspect ratio	< 2100	253	0.00 %
Expansion ratio	< 2.5	2.53	0.01 %
Impeller-volute			
Orthogonality	$> 20°$	15.57°	0.01 %
Aspect ratio	< 5000	206	0.00 %
Expansion ratio	< 3	6.99	0.09 %

Y^+ values A check of the y^+ value was done to ensure that the imposed wall cell thickness was in agreement with the requirements of the Spalart-Allmaras turbulence model. The y^+ scalar average values were examined at the BEP of all rotational speeds. The values for the Impeller and Impeller-volute grids ranged from $2.42 < y^+ < 3.97$ and $2.43 < y^+ < 4.27$ respectively, showing good agreement with the selected turbulence model and confirming that the wall cell thickness was acceptable.

Grid independence A grid independence check was done to ensure that computed results were not dependent on grid size. The global pressure ratio and isentropic efficiencies were compared. For the Impeller computation the global pressure ratio and isentropic efficiencies of three grid sizes were compared. These were obtained from the different multigrid levels. For the Impeller-volute mesh two different grid sizes were compared. The grid size of the impeller mesh remained constant at 1 846 597 while the volute mesh was adapted. The two volute mesh sizes were 545 345 and 904 469 respectively. The results are presented in Table 4.4.

Table 4.4: Grid independence.

	Grid size	**Pressure ratio**	**Efficiency**
	33 153	1.95	0.76
Impeller	229 366	2.05	0.79
	1 846 597	2.09	0.81
Impeller-volute	2 391 942	1.96	0.73
	2 747 087	1.95	0.73

It is evident that in both cases that a further increase in grid density would not yield significantly improved results, therefore the grid independence was considered to be achieved on the finest grids.

Chapter 5

Results

5.1 Introduction

The results of the experimental measurements and numerical analysis will be discussed separately at first after which they will be compared. The x-axes of all graphs represent the mass flow parameter, $\dot{m}\sqrt{T_{t1}}/p_{t1}$. The mass flow of each test point has been scaled with the inlet pressure and temperature to obtain a corrected mass flow value. The rotational speed has been normalised with the inlet temperature and is represented by the speed parameter $N/\sqrt{T_{t1}}$.

5.2 Experimental results

The total-to-static pressure ratios at the impeller, diffuser and compressor outlet are presented in Figures 5.1, 5.2 and 5.3. In addition these figures also indicate the maximum measurement deviation at each test point in the direction of both axes. Looking at the deviations of each of the mean curves one notices that the magnitude remains fairly consistent at speeds of 60 000 and 80 000 rpm, however at 100 000 rpm the deviations increase and are especially visible at the point before choke. This can be explained by the fact that the operating range at 100 000 rpm is smaller with a steeper gradient, therefore giving an opportunity for larger deviations to be measured at a single point. The larger deviations are also an indication of a reduction in stability of the speed measurement as the operating speed increases.

Figure 5.4 indicates the temperature ratio measured across the compressor. As with the pressure ratios the deviation from the mean curve remains relatively small at the lower speeds and increases at 100 000 rpm. Again this can be attributed to the stability of the speed measurement. Furthermore the time taken for sufficient heat soaking of the probes is also a contributing factor towards the variability of the temperature and as discussed in §3.5, is limited by the air supply.

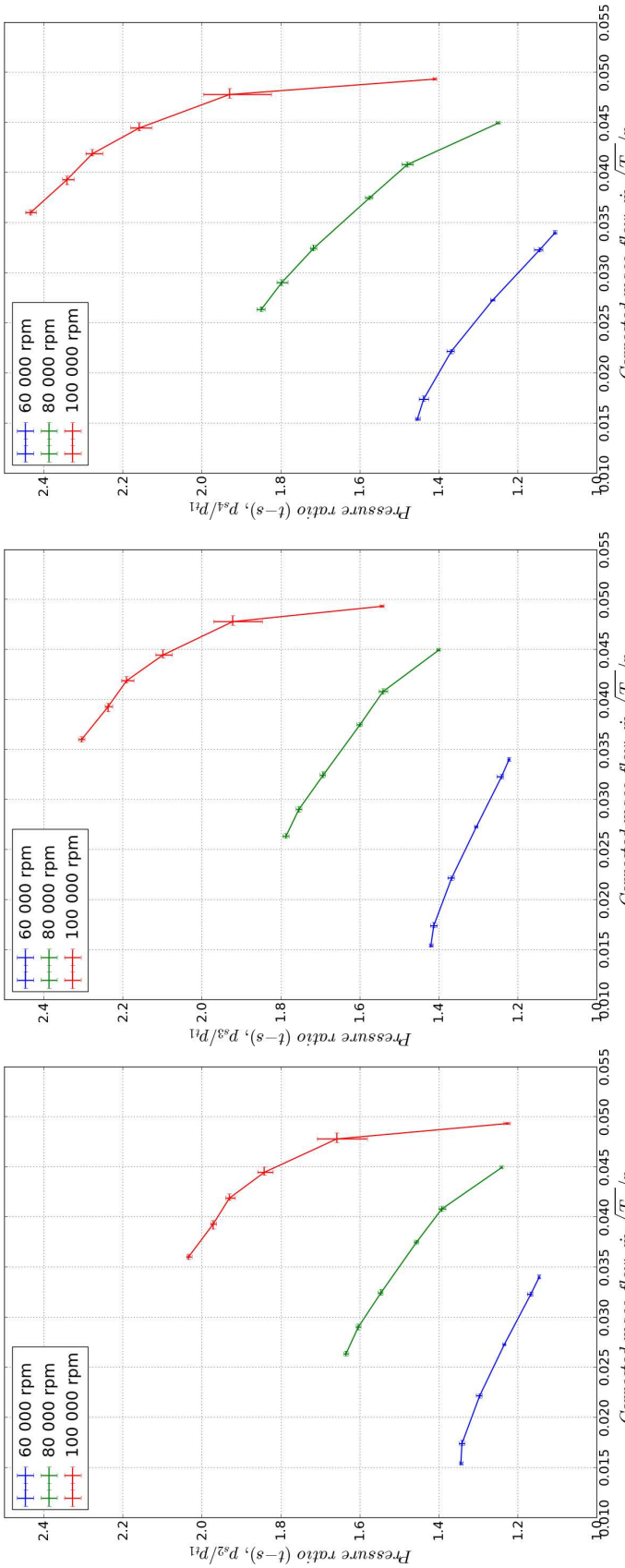

Figure 5.1: Pressure ratio after impeller.

Figure 5.2: Pressure ratio after diffuser.

Figure 5.3: Pressure ratio after volute.

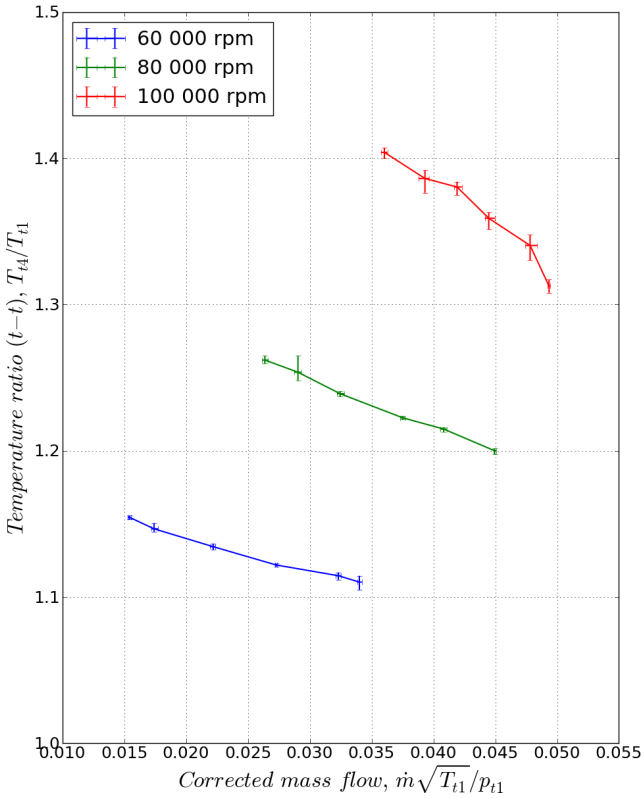

Figure 5.4: Compressor temperature ratio.

An indication of the compressor's stability is presented in Table 5.1 showing the fluctuation of values for three test points namely surge, BEP and choke. For the stability criteria given by Brun and Nored (2006) and ASME (1997), the fluctuations refer to each individual measured set of samples, however for the purposes of this thesis an overall indication of the fluctuations are given by taking the entire data set of four measurements.

Considering the inlet conditions, the fluctuations are all within the prescribed limits of stability for both criteria. However the outlet conditions show an increase in magnitude for the fluctuations. This is especially prevalent at the BEP, where temperature and pressure fluctuations exceed the criteria. This can also be said for the mass flow value fluctuations. The speed value fluctuations are shown to be the quantity of highest instability, being close to 3 % at 100 000 rpm. The fluctuations are lower at 60 000 and 80 000 rpm and increase when operating at 100 000 rpm. The fluctuation values exceed the criteria of ASME (1997) and Brun and Nored (2006). However it should be noted that the operational speeds on which the criteria is based ($< 20\,000$ rpm) are less than what was tested.

Table 5.1: Compressor test bench stability results.

	Speed	60 000		80 000		100 000	
	Criteria	ASME	Brun	ASME	Brun	ASME	Brun
Surge	Inlet temp.	0.3 %	0.6°C	0.5 %	0.7°C	0.3 %	0.4°C
	Outlet temp.	0.3 %	0.5°C	0.2 %	0.4°C	0.7 %	1.3°C
	Inlet press.	1.0 %	0.5 %	1.0 %	0.6 %	0.7 %	0.4 %
	Outlet press.	1.6 %	0.8 %	1.9 %	1.0 %	1.6 %	0.8 %
	Speed	1.6 %	520.0 rpm	2.2 %	1126.0 rpm	2.7 %	1384.0 rpm
	Mass Flow	0.8 %	0.4 %	0.9 %	0.5 %	0.5 %	0.3 %
BEP	Inlet temp.	0.3 %	0.7°C	0.5 %	0.8°C	0.4 %	0.6°C
	Outlet temp.	0.3 %	0.5°C	1.1 %	2.5°C	1.3 %	3.5°C
	Inlet press.	1.0 %	0.5 %	1.1 %	0.6 %	1.2 %	0.7 %
	Outlet press.	2.5 %	1.3 %	2.3 %	1.2 %	2.5 %	1.3 %
	Speed	2.4 %	774.0 rpm	1.1 %	588.0 rpm	2.7 %	1644.0 rpm
	Mass Flow	2.3 %	1.5 %	0.9 %	0.6 %	0.9 %	0.4 %
Choke	Inlet temp.	0.3 %	0.6°C	0.4 %	0.5°C	0.5 %	0.9°C
	Outlet temp.	0.7 %	1.4°C	0.2 %	0.3°C	0.8 %	2.0°C
	Inlet press.	0.9 %	0.5 %	0.8 %	0.4 %	0.6 %	0.4 %
	Outlet press.	1.5 %	0.9 %	1.3 %	0.7 %	1.1 %	0.6 %
	Speed	1.6 %	558.0 rpm	1.1 %	558.0 rpm	2.7 %	1394.0 rpm
	Mass Flow	1.7 %	0.9 %	0.9 %	0.5 %	1.1 %	0.7 %

5.3 Numerical results

The results of the comparative study performed on variations of the impeller geometry as described in §4.2 are presented in Figure 5.5. The computations of the four geometry variations were all performed using non-specific identical atmospheric and initial conditions, ($p_{t1} = 101\,325\,\text{Pa}$, $T_{t1} = 293\,\text{K}$). The results show the total-static pressure ratio and total-total efficiency at the diffuser outlet for the compressor curve at 80 000 rpm.

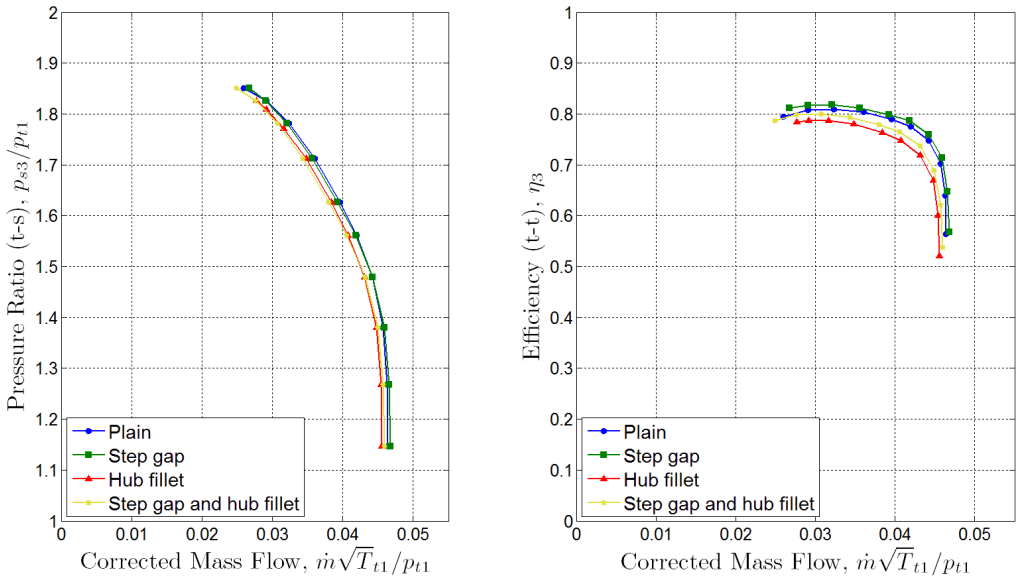

(a) Pressure ratio.

(b) Efficiency.

Figure 5.5: CFD geometry comparison.

The inclusion of the step gap has a minimal effect on the mass flow, pressure ratio and efficiency compared to the plain impeller computation. The efficiency shows an increase of $< 1\,\%$. The inclusion of the hub fillet indicates a more noticeable reduction in mass flow through the impeller which is a logical result due to the decreased flow area caused by the hub fillets. In addition the choke and surge points are reduced. Compared to the step gap computation there is a greater change in efficiency. If the efficiency curve of the hub fillet and plain computations are aligned there is a reduction in efficiency ranging from $2\,\%$ near surge and $4\,\%$ at choke.

From the results the step gap has an insignificant effect on the performance of the impeller in comparison with that of the hub fillet. As mentioned in §4.3.3 the inclusion of the hub fillet does complicate the meshing process by producing lower quality cells. This could have been overcome by increasing the grid size but at the expense of being computationally expensive. It was

therefore decided to use the plain impeller mesh when performing the volute computations.

5.4 Comparison of results

For the comparison of the experimental and numerical data only the results at the volute outlet plane were considered. Presented in Figures 5.6a and 5.6b are the total-static pressure and total-total temperature ratio's of the experimental and numerical data. From a qualitative perspective there is an excellent agreement in terms of curve trends and mass flow range in both figures. The surge and choke mass flows correlate very well especially at 80 000 and 100 000 rpm. However there is a definite offset between the experimental and numerical data in both the pressure ratio and temperature ratio graphs. The offset increases with speed and declines as choke is approached. For the pressure ratio the offset ranges from 6 % at 60 000 rpm to 10 % at 100 000 rpm. For the temperature ratio these values are lower with an offset of 3 % at 60 000 rpm and 5 % at 100 000 rpm. The temperature ratio remains fairly constant at each speed line.

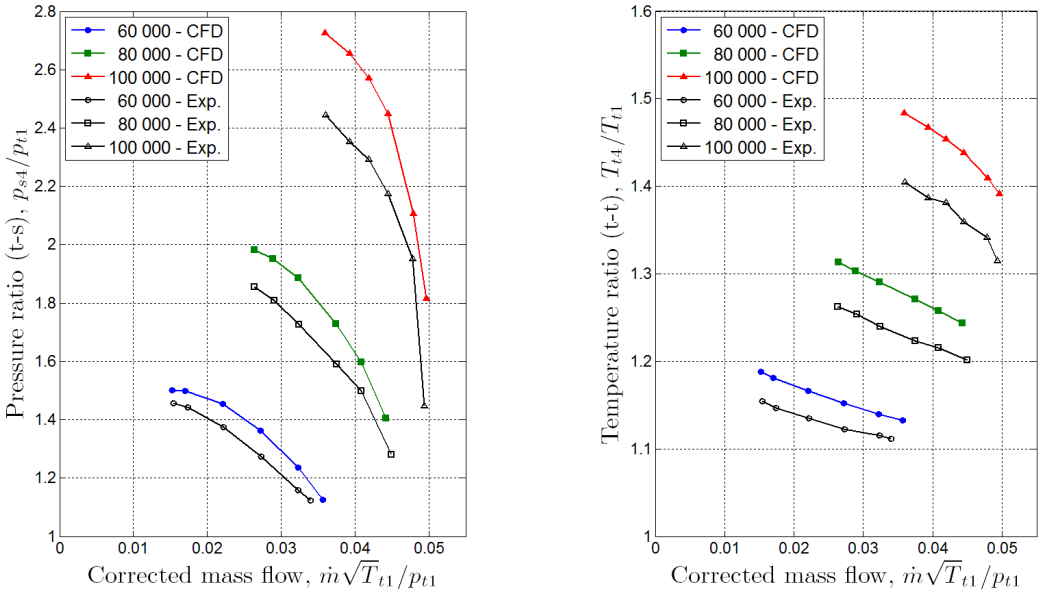

(a) Pressure ratio.

(b) Temperature ratio.

Figure 5.6: Comparison of pressure and temperature ratios.

Figures 5.7a and 5.7b indicate the static density and absolute velocity at the volute outlet plane. The static density and absolute velocity show similar trends to that of the pressure and temperature ratios. Again the curves show good qualitative agreement, but like the pressure and temperature ratio there

is a constant offset between the experimental and numerical data. The difference between the experimental and numerical data remain fairly constant with maximum differences of close to 5 % and 8 % respectively for the static density and absolute velocity.

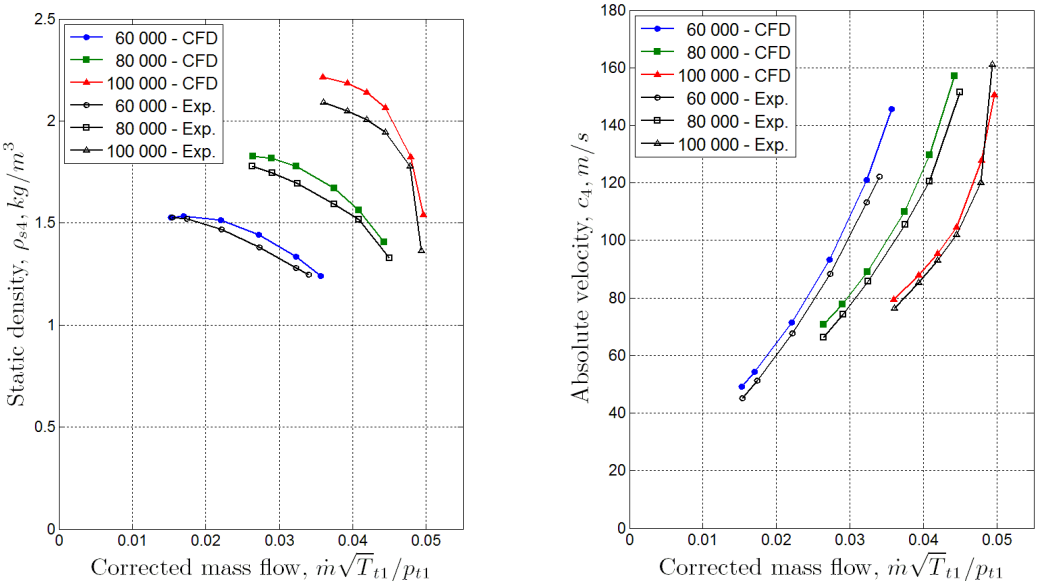

(a) Static density.

(b) Absolute outlet velocity.

Figure 5.7: Comparison of outlet static density and absolute velocity.

The total-total compressor efficiency is shown in Figure 5.8. In spite of the relative quantitative differences between the experimental and numerical data, there is good agreement between the predicted and measured efficiency of the compressor, especially at 80 000 and 100 000 rpm. The possible reason for the better correlation is likely due to the relative deviation between experimental and numerical pressure and temperature ratios. The deviation in efficiency at surge for 60 000 rpm may be explained by the closer correlation in pressure ratio while the deviation in temperature ratio remains constant throughout the curve and therefore results in a higher efficiency for the experimental results. In contrast to this where the measured pressure was substantially lower than predicted values, for example the choke conditions at 100 000 rpm, the experimental efficiency was much lower than the predicted values.

Figures 5.9 to 5.11 shows the effect that the volute has on pressure recovery from the flow exiting the diffuser. For a volute there exists a single optimal mass flow at a given operational speed for which the flow enters the exit cone tangent to the walls of the tongue. Two other flow situations also occur where the flow enters the volute at a negative incidence (higher mass flow) resulting

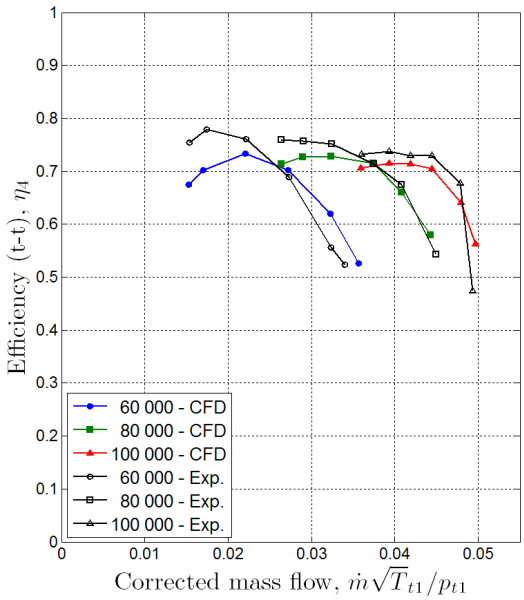

Figure 5.8: Compressor efficiency (t-t).

in a pressure decrease and the other at a positive incidense (lower mass flow) causing a rise in static pressure, (Van den Braembussche, 2006). The point at which the static pressure at the volute exit becomes lower than the diffuser pressure is an indication that the volute is receiving a greater than optimal mass flow rate. After this point there is a sharp drop in efficiency indicated in both the experimental and numerical results. A comparison of the points at which the volute pressure curve intersects the diffuser curve, again reveal good qualitative agreement between the numerical and experimental data in terms of the gradient.

In an attempt to verify the credibility of the results obtained from the study on the KKK K27 compressor impeller, a similar performance test was conducted on the "Optimised Impeller" designed by Van der Merwe (2012). His impeller was fitted to the experimental turbocharger. A spare volute was modified to accommodate the different blade geometry of this impeller design. A spare backplate was also modified so that the circumferential gap which was prevalent in the original configuration was kept to a minimum. The pressure taps to measure the impeller and diffuser outlet static pressure were also made at the correct locations pertaining to the new impeller. Van der Merwe (2012) was only concerned with the pressure ratio delivered by his impeller and therefore only these results are shown, (Figure 5.12). It should be noted that the "Optimised Impeller" was designed for a greater mass flow than what the volute could deliver, which explains the sudden drop in pressure ratio of the experimental data. This coincides with the choke conditions of the K27 impeller.

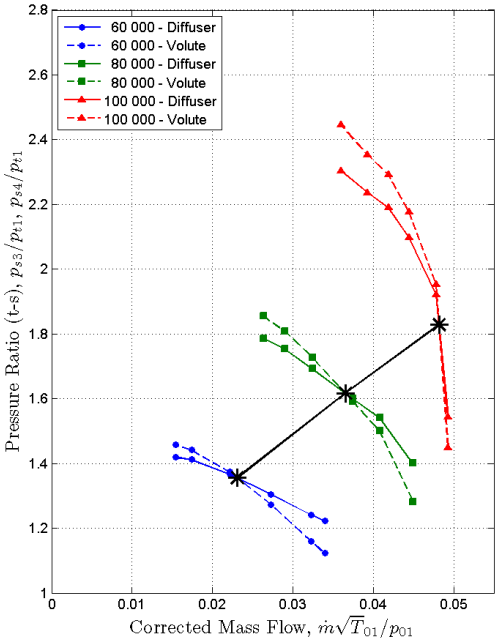

Figure 5.9: Volute pressure recovery (Experimental).

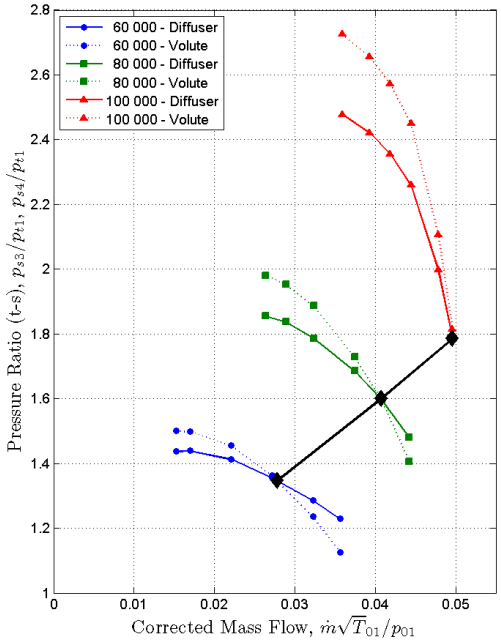

Figure 5.10: Volute pressure recovery (CFD).

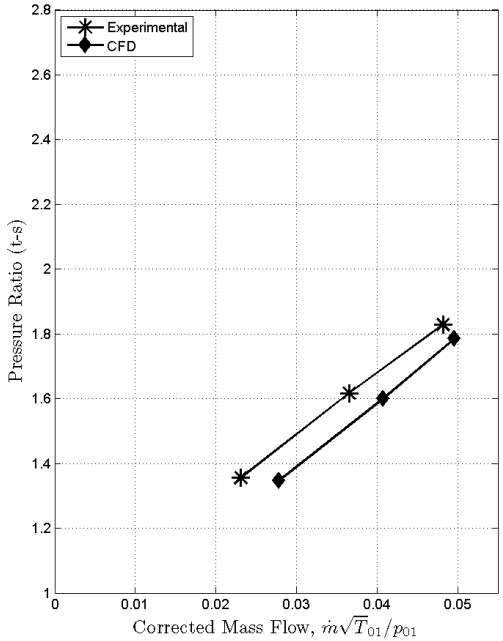

Figure 5.11: Volute pressure recovery (Comparative).

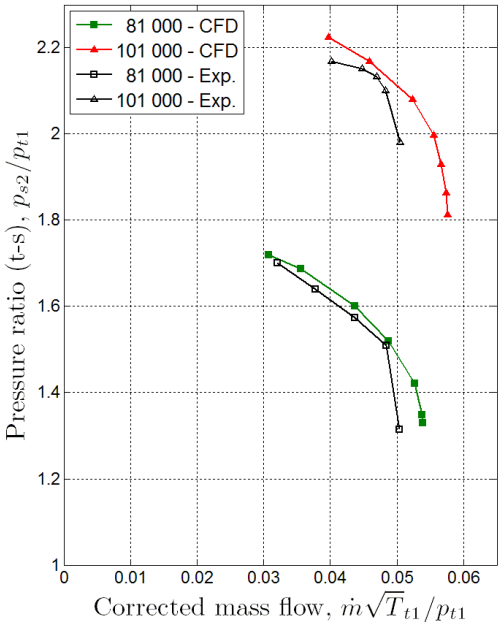

Figure 5.12: Comparative results of the impeller designed by Van der Merwe (2012).

Looking at the data points before choking occurs one notices that there is a good agreement at 81 000 rpm with differences below 2 %. The values at 101 000 rpm are also in good agreement with a maximum difference of 2 % at surge. A possible reason why the results of the "Optimised Impeller" were quantitatively more accurate could be explained by the fact that the geometrical irregularities of the circumferential gap was removed from both the numerical simulation and experimental set-up. In addition the ability of the numerical solver to solve the flow past the step gap, which can be seen as a sudden discontinuity, could be a source of inaccuracy.

Chapter 6

Conclusion and recommendations

6.1 Conclusion

A test bench was built with which to test the performance capabilities of centrifugal compressors to be used for micro gas turbine applications. An investigation was performed to choose the driving mechanism for the test facility. This resulted in the selection of an off-the-shelf turbocharger unit driven by cold compressed air supplied by an existing compressed air generating facility. This provided an easy and convenient way of driving the compressor using a turbocharger set-up. A turbocharger was selected with a compressor impeller of a similar size corresponding to the performance figures provided by Snedden (2010) and study performed by Smith (2010). The test bench was successfully operated and tests were performed on the KKK K27 compressor impeller up to a speed of 100 000 rpm. Testing at a higher speed was disregarded as it proved difficult to maintain stable operating conditions due to the higher discharge rate of the compressed air. In addition a different impeller design by Van der Merwe (2012) was successfully tested. The results from both performance tests confirm the ability of the test facility to accurately measure the performance characteristics of centrifugal impellers to be used in micro gas turbine applications up to a speed of 100 000 rpm.

Data acquisition hardware and measurement sensors were acquired and integrated into a single system with which to acquire the measured data. A graphical user interface was also developed with which the test operator can monitor and save test data. Control and monitoring of the rotational speeds was accomplished by way of an optical tachometer and remote actuation of the flow control valve located before the turbine inlet. The actuation was manually controlled by the operator with push button switches and an Arduino micro-controller. This proved to be very effective up to an operating speed of 80 000 rpm. However at 100 000 rpm the stability of the speed measurement and high rate of supply pressure loss made it more difficult to maintain a con-

stant operational speed.

Achieving the time required for steady-state operation as stipulated by the test codes, proved to be impractical, especially when operating at a speed of 100 000 rpm. In contrast to this reasonable levels of stability could be maintained within a relatively short amount of time and good repeatability was attained for all the tests that were conducted.

In parallel with the design and operation of the test bench a numerical analysis of the compressor was performed. The aim of the numerical analysis was achieved as it gave an acceptable indication of the expected performance of the KKK K27 test compressor. The effects of geometrical features such as the hub fillet and step gap on the performance of the impeller was investigated. The hub fillet had a greater impact on performance than the step gap, but was not included due to unacceptable resulting mesh quality. By including the volute geometry in the numerical study a quantitative comparison could be made with the experimental data.

6.2 Recommendations

To enhance the stability of the compressor speed measurement a more accurate method of detection is needed. It is recommended to stay with optical detection, but to utilise a more precise and intense light source such as a laser to ensure improved reflection and detection. The location of the speed measurement should remain unchanged as this provides flexibility in terms of future modifications. If a new impeller is to be tested provision can be made to allow for rotational measurement from the protruding shaft before the compressor leading edge.

Better control of the compressor operating point can be achieved by implementing feedback control. In addition to the current rotational speed feedback, positional feedback of the flow control valve can be obtained from the actuating motor with the use of rotary encoders on the motor shaft. This control may also be implemented on the throttle valve downstream of the compressor outlet. For a fully autonomous system these valves can be controlled simultaneously. However, two important factors apart from the quality of the feedback signal, affect the control of the compressor operating point namely, the continuous drop in supply pressure and changing load of the turbocharger due to the throttling of the compressor. When controlling the operating point both of these factors will have to be taken into account.

Regarding the numerical analysis any physical features such as hub fillets may be included in the analysis, depending on the relevant importance to

the goals of the study. When testing a new compressor design the seating within the backplate should leave minimal space between the impeller outlet and diffuser inlet in order to avoid any irregularities when comparing numerical and experimental data. To account for the heat loss and ensure a more accurate representation of the actual test conditions, heat transfer through the compressor casing could also be modelled.

Appendices

Appendix A

Instrumentation calibration

A.1 Pressure calibration

This section describes the calibration of the pressure transducers used on the testbench. Presented in Table A.1 are the equations for the pressure transducer calibration curves shown in Figures A.1 and A.2.

Table A.1: Pressure calibration curve equations

Transducer		**Equation**	R^2
Bellmouth	dp	$y = 0.373\,92x - 0.743\,04$	0.999
Compressor inlet	0	$y = 19.782\,86x + 1.539\,62$	0.999
Impeller outlet	1	$y = 50.136\,86x - 5.518\,46$	0.999
Diffuser outlet	2	$y = 49.873\,79x - 3.745\,35$	0.999
Compressor outlet	3	$y = 50.012\,83x - 4.621\,56$	0.999
Orifice inlet	4	$y = 100.234\,76x - 3.261\,14$	0.999
Orifice outlet	5	$y = 100.455\,70x - 5.697\,16$	0.999
Turbine inlet	6	$y = 60.729\,59x - 8.812\,10$	0.999
Turbine outlet	7	$y = 60.566\,28x - 7.997\,92$	0.999
Lubrication oil	8	$y = 91.276\,71x - 16.603\,75$	0.999
Atmospheric	9	$y = 71.997\,75x - 380.951\,43$	0.999

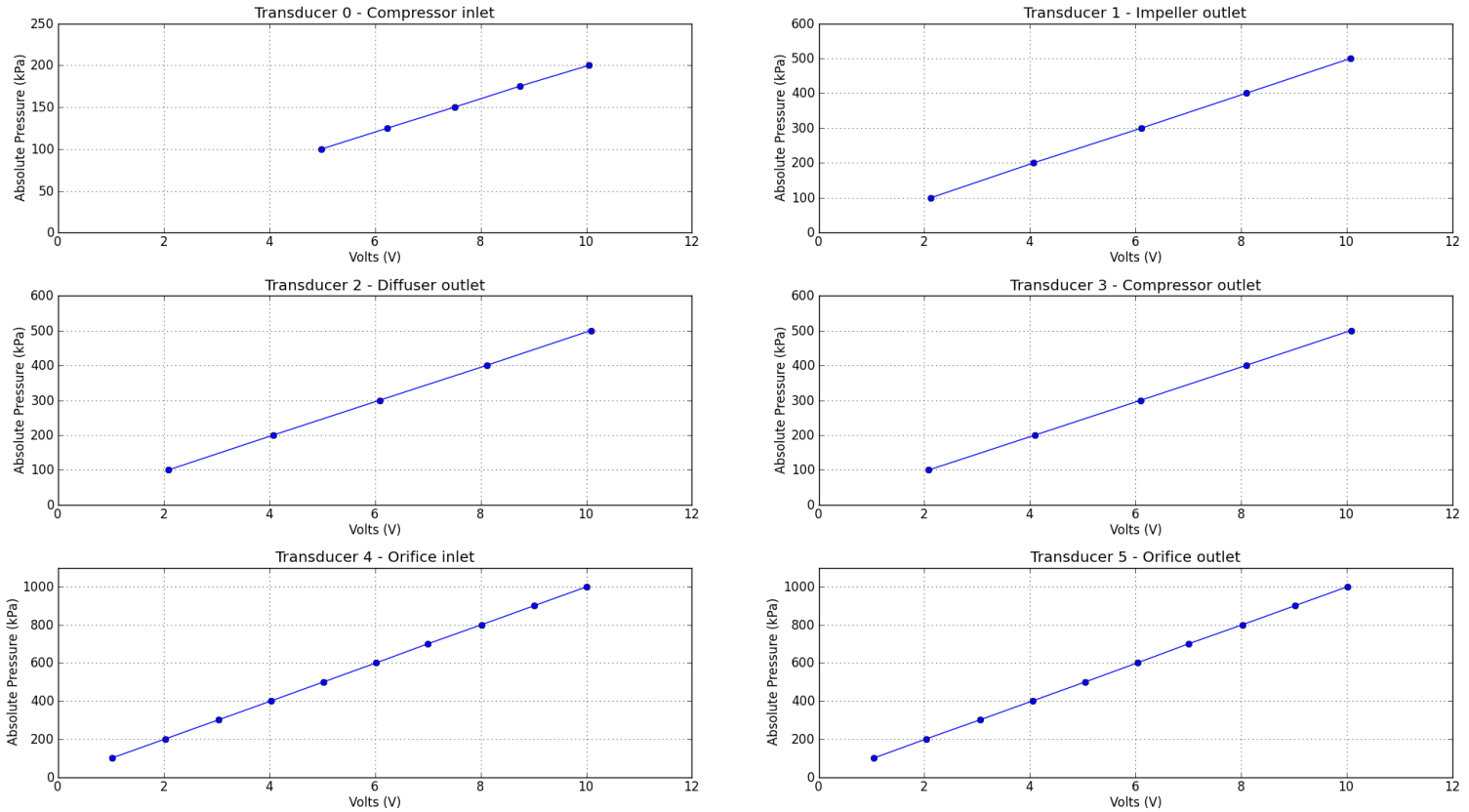

Figure A.1: Pressure calibration curves (Transducers 0 - 6).

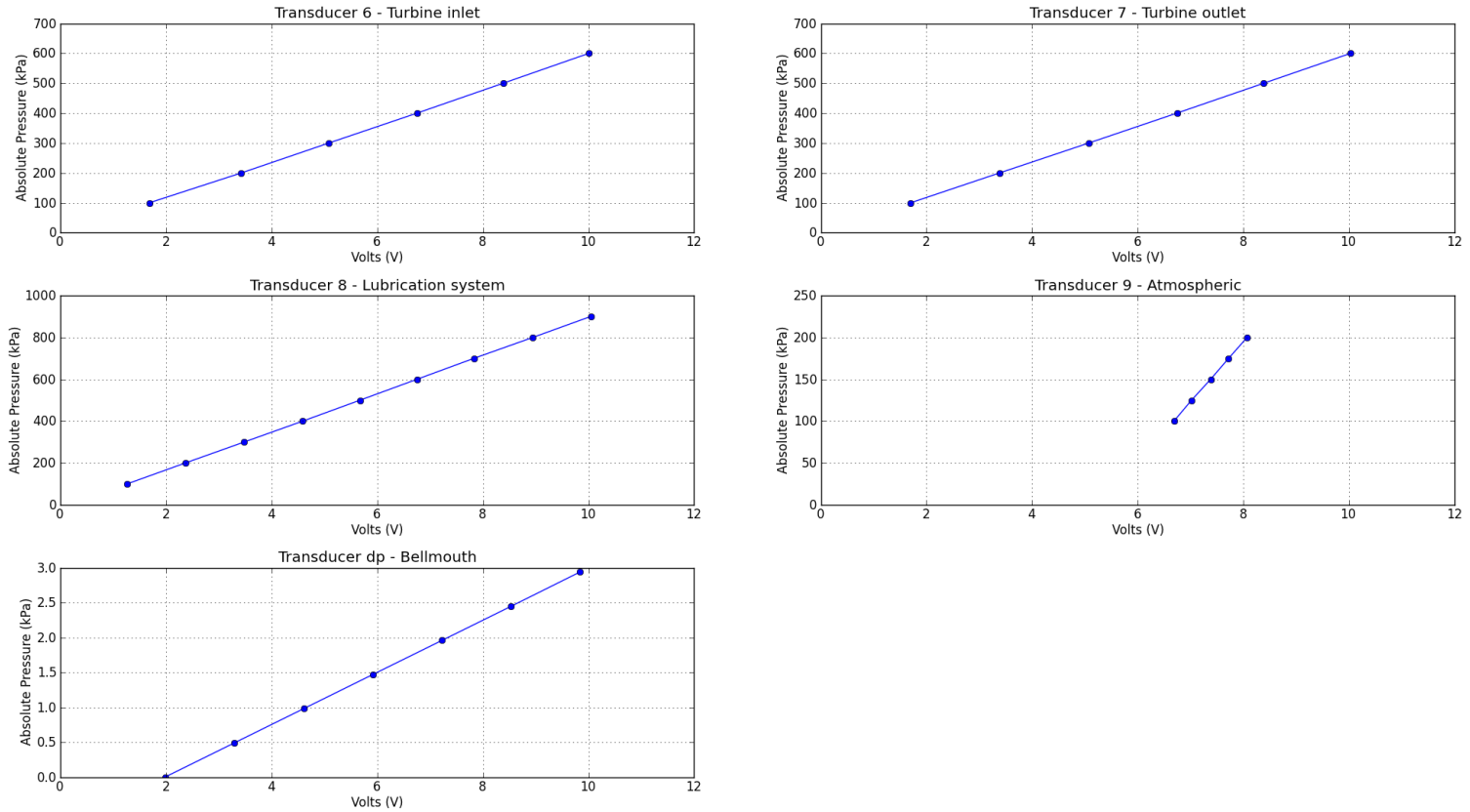

Figure A.2: Pressure calibration curves (Transducers 7 - 9, differential).

Calibration process The pressure transducers were calibrated in the Mechatronics Laboratory of the Mechanical Engineering Department. The Mechatronics Laboratory is fitted with air supply points which deliver a maximum gauge pressure of 600 kPa. The HBM P8AP (strain gauge type) absolute pressure transducers were calibrated with the HBM AE301 resistive instrument amplifiers. When referring to the calibration of the absolute pressure transducers it is in fact referring to the adjustment and fine tuning of the amplifier associated with a specific transducer. Further more all the transducers were calibrated on the cRIO-9073 data acquisition system with the NI-9207 C-Series Analogue Input modules. A 1000 kPa WIKA calibration pressure gauge was used as reference for the pressure measured by the transducers. The differential pressure transducer was calibrated with a Betz manometer.

Prior to calibration of the pressure transducers the nominal measuring range (NMR) of a specific transducer was determined to ensure a maximum measurement resolution. For example, the maximum or part load (PL) at the compressor inlet was taken to be 200 kPa and the part load at the compressor outlet as 500 kPa. This meant that a full-scale measuring range (MR) of 0 - 10 V would be measured for 200 kPa and 500 kPa at the respective locations. The actual pressure measured by a transducer was the combined gauge pressure indicated by the calibration gauge and atmospheric pressure. For example the nominal measuring range is calculated as at the compressor outlet:

$$\begin{aligned} V_{NMR} &= \frac{P_{PL}}{P_{NL}} \cdot \frac{10\ V}{V_{MR}} \cdot V_{sense} \\ &= \frac{500\,\text{kPa}}{1000\,\text{kPa}} \cdot \frac{10\,\text{V}}{10\,\text{V}} \cdot 2\,\text{mV/V} \\ &= 1\,\text{mV/V} \end{aligned} \tag{A.1.1}$$

Once the nominal measuring range had been determined the necessary adjustments were made to the amplifier to scale the load range and ensure a maximum measurement resolution.

In addition a zero-point reading (zero-point voltage) was taken to ensure transducer linearity through the origin. Usually the zero-point indicates where the transducer measurement passes though the origin (0 V). The transducer is either discharged or preloaded to a set zero reference value when determining this point. Theoretically the zero-point, is obtained if an absolute pressure of 0 kPa, a perfect vacuum is measured. However this was not possible with the available equipment. To circumvent this problem the zero-point is determined with reference to atmospheric pressure. The atmospheric pressure is measured, from which the theoretical output voltage is calculated in relation to the expected maximum measured pressure (part load) and output voltage. For example the zero point reading is calculated as follows:

$$\begin{aligned} V_{ZP} &= V_{MAX} \cdot \frac{P_{ATM}}{P_{PL}} \\ &= 10\,\mathrm{V} \cdot \frac{98\,\mathrm{kPa}}{500\,\mathrm{kPa}} \\ &= 1.96\,\mathrm{V} \end{aligned} \tag{A.1.2}$$

Therefore when calibrating the transducer zero-point reading the amplifier is adjusted so such that an output voltage of 1.96 V is measured at current atmospheric pressure.

During calibration, the calibration gauge and transducer were connected in parallel to an air supply point. The transducer was then connected to the instrument amplifiers which in turn was connected to the cRIO DAQ. Once all the pre-calibration adjustments were completed the, air supply was set to respective part load pressure of the transducer. The pressure was manually controlled with a valve at the supply point. Readings were taken in decreasing increments of 100 kPa from maximum to zero gauge pressure from which a straight line graph was plotted. From this graph a linear fit was done to obtain the calibration equation of the respective transducer and amplifier combination.

A.2 Bellmouth calibration

This section describes the preliminary calibration of the inlet bellmouth of the centrifugal compressor test bench.

Calibration process A pitot tube with a head diameter of approximately 2 mm was inserted into the center of the duct connecting the bellmouth to the compressor inlet. The pitot tube was connected to a water manometer, while static pressure tappings in the bellmouth throat were connected to both a Betz micromanometer and a pressure transducer. The probe was inserted approximately 10 diameters downstream of the bellmouth outlet, to ensure fully developed flow. A coarse radial traverse was performed to confirm that the velocity profile was of the expected form for fully developed turbulent pipe flow Figure A.3.

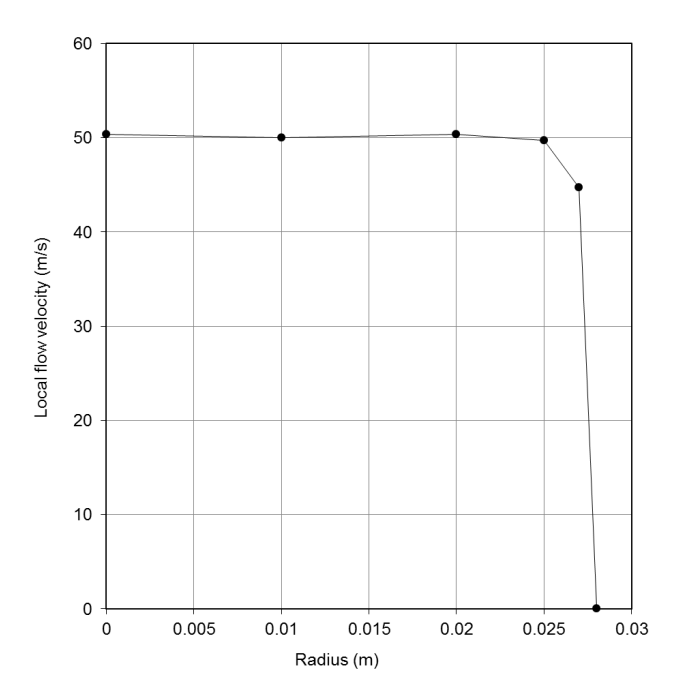

Figure A.3: Velocity profile for duct at Re = 1.7×10^5.

The average flow rate was calculated from the flow rate at the centre of the duct by means of Eq. A.2.1 White (2005):

$$V_{avg} = \frac{V_{max}}{1 \times 1.3 \times f} \tag{A.2.1}$$

where f is the duct friction factor White (2005):

$$f \approx 1.8ln\frac{Re_d}{6.9}Re_d10^5 \tag{A.2.2}$$

The true mass flow rate in the duct is then calculated from the average duct velocity. The ideal mass flow through the bellmouth is calculated by means of Bernoulli's theory, assuming no losses in the bellmouth or duct. The ratio of the duct mass flow and the ideal bellmouth mass flow rate is the discharge coefficient C_d. The compressor was run at speeds from 20 000 rpm to 60 000 rpm in increments of 20 000 rpm, and from 70 000 rpm to 90 000 rpm in increments of 10 000 rpm. More points were desired for higher rotational speeds as these are closer to the design operating range of the compressor, and thus the region in which accuracy is most important.

The throttling valve downstream of the compressor remained fully opened throughout testing, thus reflecting the maximum flow rate through the compressor at each speed. The relationship between the discharge coefficient and the bellmouth-diameter based and duct-diameter based Reynolds numbers, as determined by the calibration, are shown in Figure A.4. An exponential correlation is fitted in each case, thus the value of C_d is asymptotic to 1. The uncertainty as indicated in the plots shows the possible error in the readings of the water manometer attached to the pitot-static tube. The coefficient of discharge for the bellmouth is calculated using the exponential correlation given by Eq. A.2.3:

$$C_d = e^{\frac{-1500}{Re_{bm}}} \tag{A.2.3}$$

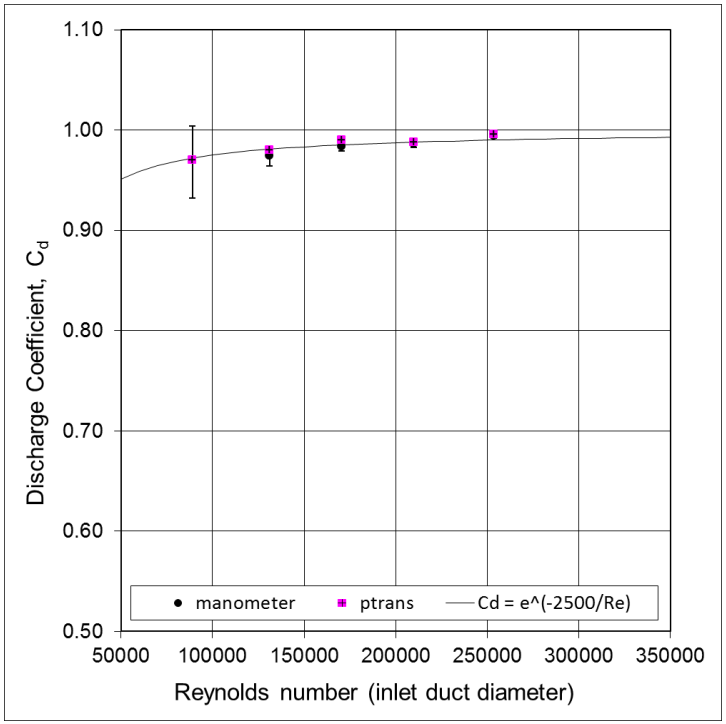

(a) Inlet duct discharge coeffient

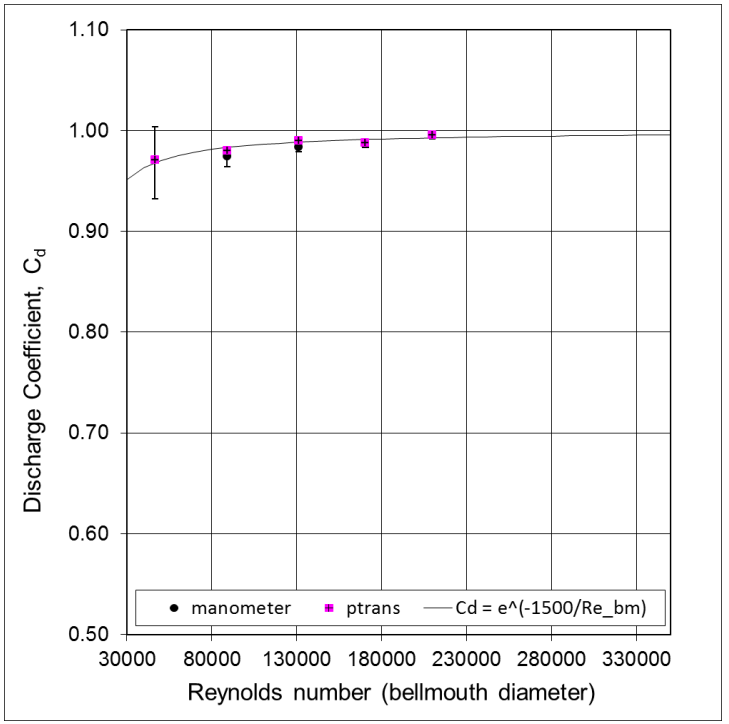

(b) Bellmouth discharge coeffient.

Figure A.4: Flow calibration discharge coefficients.

Appendix B

Lubrication system

B.1 System diagram

Figure B.1 shows the pipeline diagram of the lubrication system.

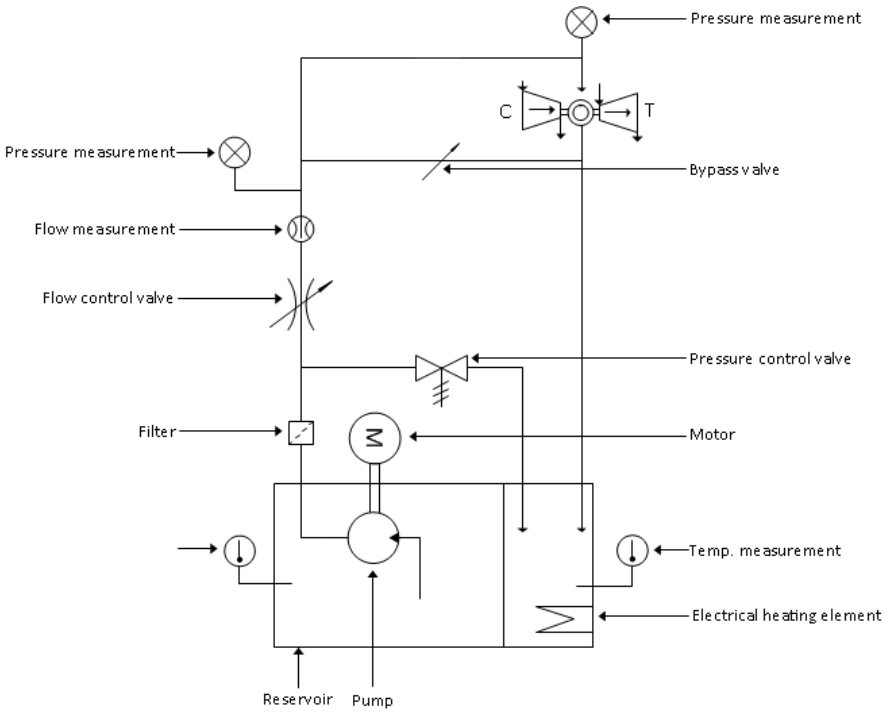

Figure B.1: Lubrication system line diagram (Adapted from Nieuwoudt (1987)).

Figure B.2 shows cross-sectional view bearing and lubrication assembly of a typical turbocharger.

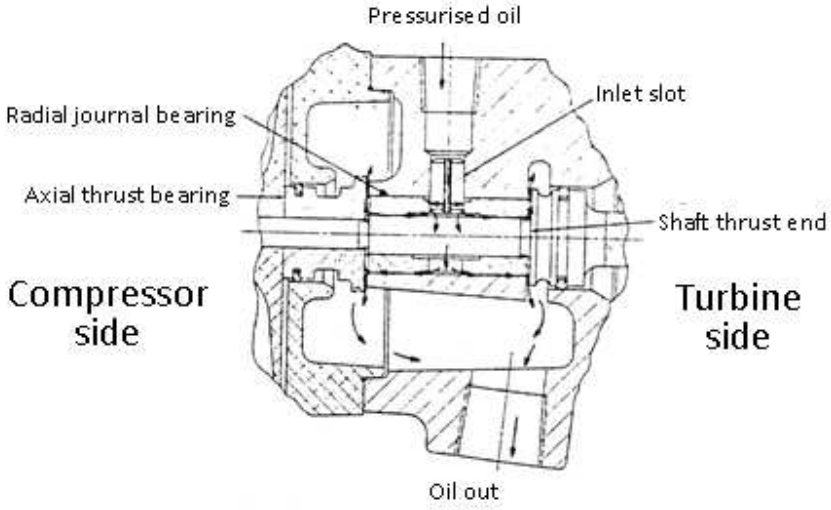

Figure B.2: Lubrication of a turbocharger (Adapted from Nieuwoudt (1987)).

Appendix C

Data acquisition programming

C.1 Virtual instrument block diagrams

The following block diagrams show data flow and manipulation of the measured quantities.

C.1.1 Speed measurement scaling

Figures C.1 and C.2 show the scaling and signal conditioning of the speed sensor (tachometer).

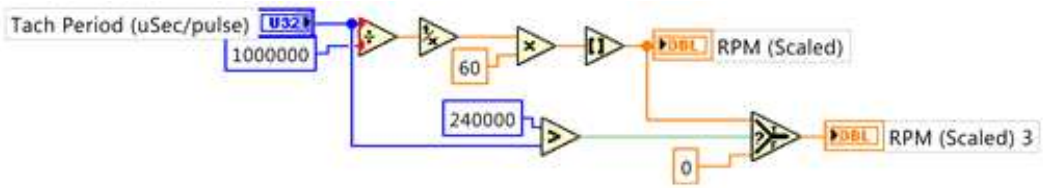

Figure C.1: Speed measurement scaling block diagram.

Figure C.1 shows the block diagram where the conditioned tachometer signal is converted to a rotational speed. On the left side the conditioned tachometer input signal is measured signal period length in $\mu_{sec}/pulse$. This is converted to seconds by dividing by scalar value of $1{\times}10^6$. The signal value is converted from the time domain to frequency domain by taking the reciprocal. The rotational speed in terms of revolutions per minute is obtained by multiplying the frequency by a scalar value of 60. Since there is only one reflective surface no additional scaling was necessary.

Figure C.2 shows how the raw tachometer signal is converted and conditioned. This is done on the FPGA module of the real-time controller. The input is the raw tachometer signal. The signal period is used to determined

the rotational speed as mentioned previously. The period is determined by counting the number of clock cycles (tick counts) with a 32bit counter and shift register between consecutive periods. The counter is triggered either through a "falling" or "rising" edge of the signal. The tick count is then converted to a time value in relation to the FPGA clock speed. The state of the counter changes whenever the threshold and/or hysteresis limits have been crossed/exceeded. These block diagrams are shown in Figures C.3 and C.4. Once the signal has been conditioned it is passed on from the FPGA module to the real-time processor where it is converted to a rotational speed and sent to the host computer.

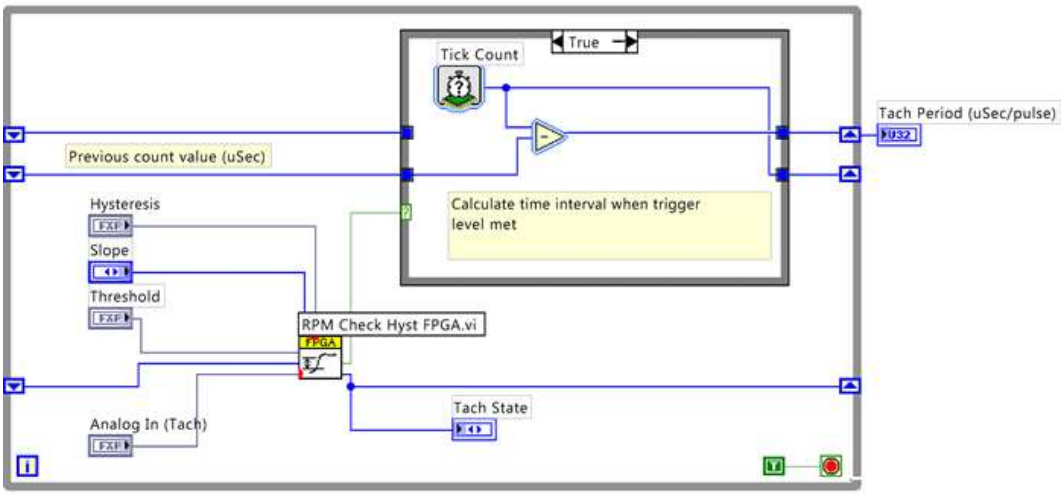

Figure C.2: Speed measurement signal conditioning blockdiagram.

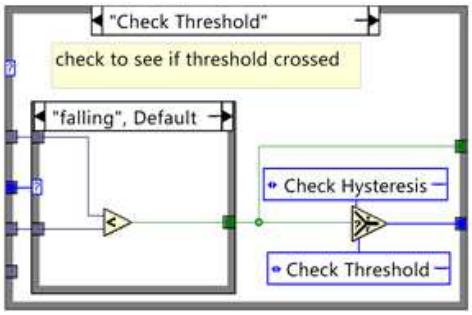

Figure C.3: Speed measurement threshold check blockdiagram.

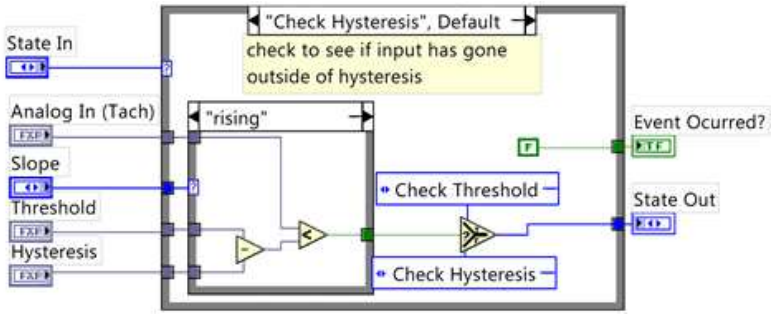

Figure C.4: Speed measurement hysteresis check blockdiagram.

C.1.2 Pressure measurement scaling

Figure C.5 shows the scaling of the measured pressure signals. On the left side raw data (DC voltage) from the FPGA module is expanded to show the individual transducer signal outputs. These signals are then scaled according to the individual transducer calibration curve equations. Once the values have been scaled they are grouped and passed to the real-time interface which sends the data from the to host computer via network communication.

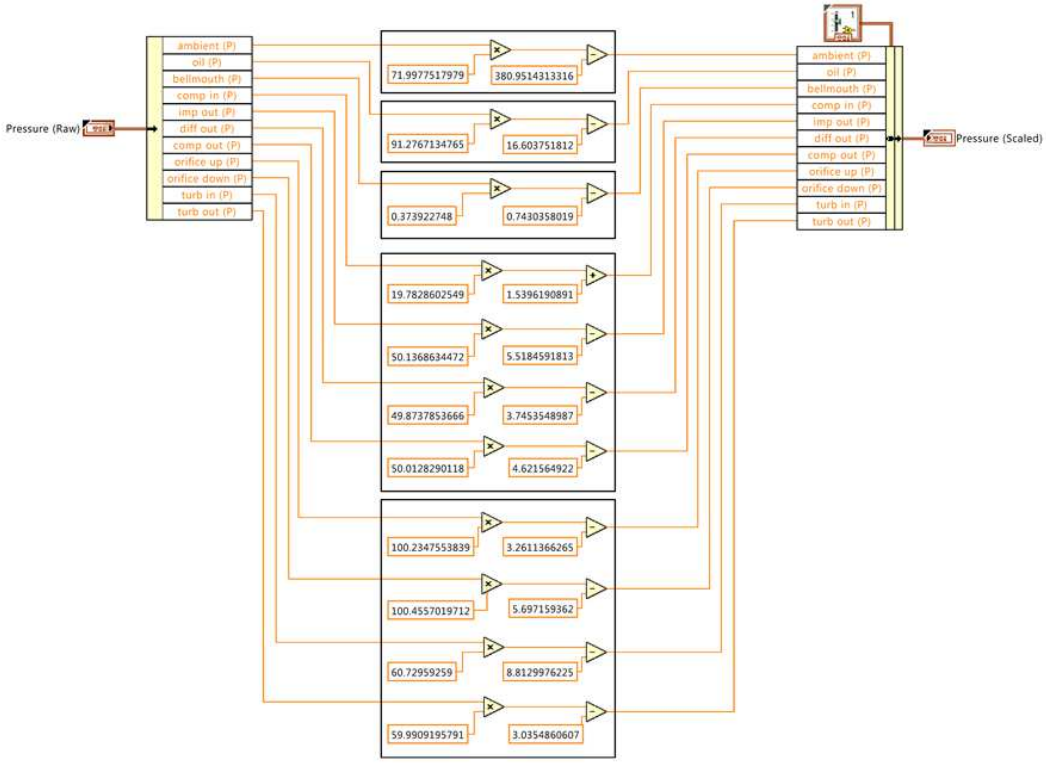

Figure C.5: Pressure measurement scaling blockdiagram.

C.1.3 Temperature measurement scaling

The raw temperature measurements are sampled by the FPGA chip and the scaling is performed on real-time module. All thermocouples are individually sampled and passed to the real-time application. Figure C.6 shows the real-time block diagram where the raw temperature data (μV) are separated into groups corresponding to the type of thermocouple. The raw signals are then converted to an single data array and passed to a for loop. Within this for loop each thermocouple voltage is converted to a temperature value, in units of Kelvin, by means of polynomial equations (Eq. C.1.1 - C.1.3). These equations were included as standard in the LabVIEW™software.

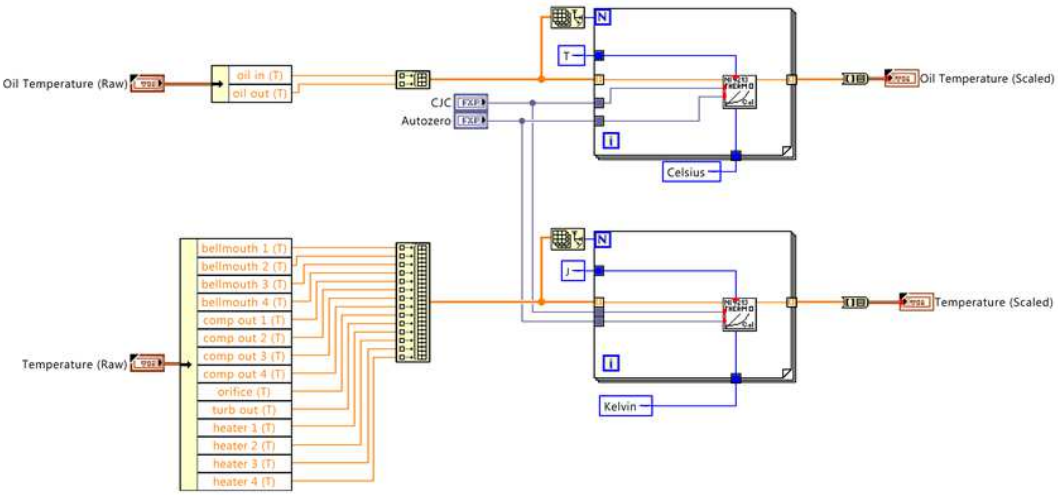

Figure C.6: Temperature measurement scaling blockdiagram.

The polynomial equations used for the J-type thermocouples were: For a temperature range between $-210\,^{\circ}\mathrm{C}$ to $0\,^{\circ}\mathrm{C}$:

$$\begin{aligned} T = {} & V((1.952\,826\,8\times10^{-2}) + V((-1.228\,618\,5\times10^{-6}) + V((-1.075\,217\,8\times10^{-9}) \\ & + V((-5.908\,693\,3\times10^{-13}) + V((-1.725\,671\,3\times10^{-16}) \\ & + V((-2.813\,151\,3\times10^{-20}) + V((-2.396\,337\,0\times10^{-24}) \\ & + V(-8.382\,332\,1\times10^{-29})))))))) \end{aligned} \tag{C.1.1}$$

with an error range of $0.03\,^{\circ}\mathrm{C}$ to $-0.05\,^{\circ}\mathrm{C}$.
For a temperature range between $0\,^{\circ}\mathrm{C}$ to $760\,^{\circ}\mathrm{C}$:

$$\begin{aligned} T = {} & V((1.978\,425\times10^{-2}) + V((-2.001\,204\times10^{-7}) + V((1.036\,969\times10^{-11}) \\ & + V((-2.549\,687\times10^{-16}) + V((3.585\,153\times10^{-21}) \\ & + V((-5.344\,285\times10^{-26}) + V(5.099\,890\times10^{-31})))))) \end{aligned} \tag{C.1.2}$$

with an error range of 0.04 °C to −0.04 °C.

The polynomial equations used for the T-type thermocouples were: For a temperature range between 0 °C to 400 °C:

$$\begin{aligned} T = V((2.592\,800\times10^{-2}) + V((-7.602\,961\times10^{-7}) + V((4.637\,791\times10^{-11}) \\ + V((-2.165\,394\times10^{-15}) + V((6.048\,144\times10^{-20}) \\ + V(-7.293\,422\times10^{-25}))))) \end{aligned} \tag{C.1.3}$$

with an error range of 0.03 °C to −0.03 °C.

C.1.4 Flow measurement

The mass flow is determined from a combination of measured quantities such as the atmospheric pressure and temperature and differential pressure across the bellmouth. Once these have been scaled they are used as input to the mass flow calculation blockdiagram vi (Figure C.7). The various quantities such as throat velocity and Reynolds number are calculated from these inputs and with constants such as the kinematic viscosity and throat area the mass flow is then calculated.

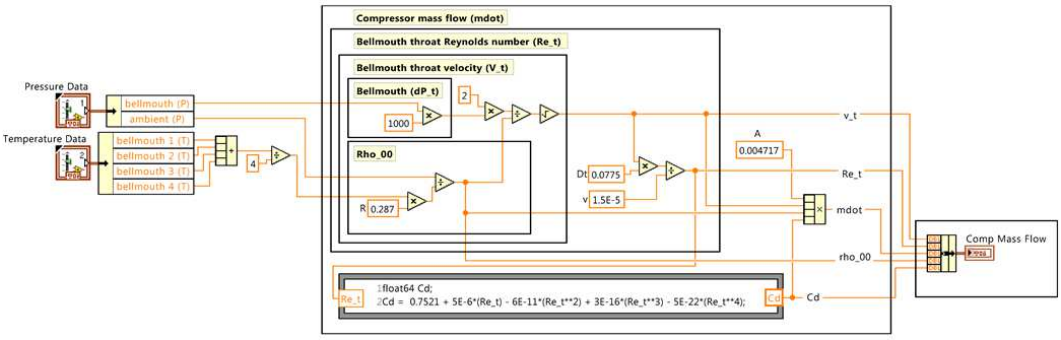

Figure C.7: Mass flow blockdiagram.

Appendix D

Sample data

The following tables shows sample data at $N = 80\,000$ rpm, $\dot{m}$ =0.191 kg/s.

Table D.1: Experimental data for the compressor speed, mass flow and pressure, (samples 1 - 20).

$S\#$ i	N (rpm)	$\dot{m}$ (kg/s)	Δp (Pa)	p_{amb} (kPa)	p_{s1} (kPa)	p_{s2} (kPa)	p_{s3} (kPa)	p_{s4} (kPa)
1	79787	0.191	692.018	99.233	95.722	153.929	168.501	170.904
2	79787	0.191	692.572	99.229	95.702	153.886	168.405	170.647
3	79787	0.191	692.759	99.229	95.702	153.886	168.405	170.647
4	79787	0.191	691.559	99.294	95.721	154.020	168.630	170.826
5	79787	0.191	691.171	99.294	95.721	154.020	168.630	170.826
6	80645	0.191	692.141	99.200	95.722	154.009	168.589	170.779
7	80645	0.191	692.140	99.200	95.722	154.009	168.589	170.779
8	80645	0.191	693.383	99.141	95.720	154.011	168.592	170.932
9	80645	0.191	693.100	99.141	95.720	154.011	168.592	170.932
10	80645	0.191	692.525	99.245	95.710	153.902	168.473	170.802
11	80645	0.191	692.724	99.245	95.710	153.902	168.473	170.802
12	79787	0.191	692.253	99.170	95.707	153.876	168.379	170.683
13	80645	0.191	693.011	99.170	95.707	153.876	168.379	170.683
14	79787	0.191	693.635	99.208	95.708	153.918	168.434	170.643
15	80645	0.191	693.714	99.208	95.708	153.918	168.434	170.643
16	80645	0.191	693.213	99.267	95.709	153.837	168.398	170.712
17	79787	0.191	693.198	99.267	95.709	153.837	168.398	170.712
18	80645	0.191	692.485	99.273	95.740	154.050	168.606	170.966
19	80645	0.191	692.373	99.273	95.740	154.050	168.606	170.966
20	79787	0.191	693.096	99.164	95.728	154.050	168.579	170.799
.	.	.	.	.	.	.	.	.
.	.	.	.	.	.	.	.	.

Table D.2: Experimental data for the compressor speed, mass flow and pressure, (samples 21 - 60).

$S\#$ i	N (rpm)	$\dot{m}$ (kg/s)	Δp (Pa)	p_{amb} (kPa)	p_{s1} (kPa)	p_{s2} (kPa)	p_{s3} (kPa)	p_{s4} (kPa)
.	.	.	.	.	.	.	.	.
.	.	.	.	.	.	.	.	.
21	79787	0.191	693.195	99.164	95.728	154.050	168.579	170.799
22	79787	0.191	693.437	99.215	95.725	153.988	168.491	170.774
23	79787	0.191	693.344	99.215	95.725	153.988	168.491	170.774
24	80645	0.191	693.238	99.242	95.722	153.904	168.425	170.699
25	80645	0.191	693.482	99.242	95.722	153.904	168.425	170.699
26	80645	0.191	692.970	99.203	95.717	153.877	168.418	170.805
27	80645	0.191	692.935	99.203	95.717	153.877	168.418	170.805
28	80645	0.191	693.513	99.219	95.713	153.880	168.303	170.394
29	79787	0.191	693.501	99.219	95.713	153.880	168.303	170.394
30	80645	0.191	692.935	99.205	95.751	153.894	168.420	170.638
31	79787	0.191	692.838	99.205	95.751	153.894	168.420	170.638
32	79787	0.191	692.760	99.230	95.701	153.813	168.391	170.656
33	80645	0.191	692.777	99.230	95.701	153.813	168.391	170.656
34	79787	0.191	693.015	99.183	95.718	153.859	168.431	170.666
35	80645	0.191	692.905	99.183	95.718	153.859	168.431	170.666
36	80645	0.191	692.839	99.207	95.741	153.898	168.430	170.769
37	80645	0.191	692.901	99.207	95.741	153.898	168.430	170.769
38	79787	0.191	692.932	99.207	95.741	153.898	168.430	170.769
39	80645	0.191	692.914	99.189	95.733	153.901	168.476	170.861
40	80645	0.191	693.012	99.189	95.733	153.901	168.476	170.861
41	80645	0.191	692.995	99.206	95.728	153.843	168.371	170.752
42	80645	0.191	692.900	99.206	95.728	153.843	168.371	170.752
43	79787	0.191	692.905	99.220	95.715	153.828	168.400	170.672
44	80645	0.191	692.561	99.220	95.715	153.828	168.400	170.672
45	79787	0.191	692.748	99.231	95.719	153.814	168.387	170.789
46	80645	0.191	692.888	99.231	95.719	153.814	168.387	170.789
47	79787	0.191	693.121	99.178	95.712	153.815	168.345	170.642
48	80645	0.191	693.201	99.178	95.712	153.815	168.345	170.642
49	80645	0.191	692.887	99.194	95.732	153.817	168.337	170.677
50	79787	0.191	693.055	99.194	95.732	153.817	168.337	170.677
51	80645	0.191	692.172	99.203	95.732	153.683	168.183	170.456
52	80645	0.191	691.983	99.203	95.732	153.683	168.183	170.456
53	79787	0.191	694.180	99.138	95.720	153.709	168.188	170.488
54	80645	0.191	693.978	99.138	95.720	153.709	168.188	170.488
55	79787	0.191	692.188	99.292	95.737	153.779	168.249	170.564
56	79787	0.191	692.290	99.292	95.737	153.779	168.249	170.564
57	79787	0.191	692.189	99.187	95.760	153.670	168.153	170.471
58	79787	0.191	693.175	99.187	95.760	153.670	168.153	170.471
59	79787	0.191	692.238	99.176	95.718	153.420	167.883	170.094
60	79787	0.191	693.096	99.176	95.718	153.420	167.883	170.094
.	.	.	.	.	.	.	.	.
.	.	.	.	.	.	.	.	.

Table D.3: Experimental data for the compressor speed, mass flow and pressure, (samples 61 - 100).

$S\#$ i	N (rpm)	$\dot{m}$ (kg/s)	Δp (Pa)	p_{amb} (kPa)	p_{s1} (kPa)	p_{s2} (kPa)	p_{s3} (kPa)	p_{s4} (kPa)
.	.	.	.	.	.	.	.	.
.	.	.	.	.	.	.	.	.
61	79787	0.191	692.054	99.227	95.749	153.597	168.035	170.224
62	80645	0.191	692.092	99.227	95.749	153.597	168.035	170.224
63	80645	0.190	691.424	99.235	95.744	153.477	167.951	170.249
64	80645	0.190	691.131	99.235	95.744	153.477	167.951	170.249
65	79787	0.190	691.103	99.231	95.721	153.454	167.877	170.116
66	79787	0.190	691.493	99.231	95.721	153.454	167.877	170.116
67	79787	0.190	690.962	99.168	95.731	153.491	167.913	170.058
68	79787	0.190	691.572	99.168	95.731	153.491	167.913	170.058
69	79787	0.190	690.817	99.167	95.727	153.462	167.939	170.235
70	79787	0.190	690.941	99.167	95.727	153.462	167.939	170.235
71	80645	0.190	690.802	99.172	95.759	153.380	167.845	170.140
72	79787	0.190	691.019	99.172	95.759	153.380	167.845	170.140
73	79787	0.190	689.872	99.226	95.752	153.431	167.856	170.095
74	79787	0.190	689.452	99.226	95.752	153.431	167.856	170.095
75	80645	0.190	689.989	99.212	95.766	153.549	168.031	170.431
76	79787	0.190	689.891	99.212	95.766	153.549	168.031	170.431
77	79787	0.190	690.202	99.169	95.726	153.259	167.635	169.725
78	79787	0.190	689.618	99.169	95.726	153.259	167.635	169.725
79	80645	0.190	689.299	99.169	95.726	153.259	167.635	169.725
80	80645	0.190	689.236	99.187	95.781	153.458	167.867	170.174
81	79787	0.190	689.492	99.187	95.781	153.458	167.867	170.174
82	80645	0.190	688.818	99.255	95.740	153.346	167.738	169.978
83	79787	0.190	688.670	99.255	95.740	153.346	167.738	169.978
84	79787	0.190	688.290	99.236	95.743	153.431	167.865	170.098
85	80645	0.190	688.343	99.236	95.743	153.431	167.865	170.098
86	79787	0.190	687.686	99.212	95.752	153.455	167.869	170.065
87	79787	0.190	687.691	99.212	95.752	153.455	167.869	170.065
88	79787	0.190	688.419	99.133	95.744	153.325	167.739	169.880
89	80645	0.190	688.264	99.133	95.744	153.325	167.739	169.880
90	80645	0.190	687.992	99.193	95.744	153.283	167.740	170.024
91	79787	0.190	687.049	99.193	95.744	153.283	167.740	170.024
92	80645	0.190	687.864	99.200	95.765	153.436	167.853	169.915
93	79787	0.190	687.666	99.200	95.765	153.436	167.853	169.915
94	80645	0.190	686.810	99.226	95.754	153.390	167.738	169.933
95	80645	0.190	686.082	99.226	95.754	153.390	167.738	169.933
96	79787	0.190	686.266	99.227	95.767	153.349	167.707	169.813
97	79787	0.190	686.240	99.227	95.767	153.349	167.707	169.813
98	79787	0.190	686.591	99.172	95.758	153.399	167.783	170.029
99	79787	0.190	686.647	99.172	95.758	153.399	167.783	170.029
100	79787	0.190	686.260	99.200	95.752	153.303	167.721	169.873

Table D.4: Experimental data for the compressor temperature, (samples 1 - 40).

$S\#$ i	T_{0-1} (K)	T_{0-2} (K)	T_{0-3} (K)	T_{0-4} (K)	T_{5-1} (K)	T_{5-2} (K)	T_{5-3} (K)	T_{5-4} (K)
1	290.562	290.485	290.381	290.257	359.519	359.373	359.248	359.008
2	290.478	290.435	290.315	290.126	359.404	359.341	359.085	358.872
3	290.601	290.447	290.327	290.293	359.446	359.469	359.204	358.977
4	290.516	290.522	290.358	290.234	359.460	359.407	359.261	358.918
5	290.359	290.286	290.237	290.095	359.334	359.306	359.165	358.837
6	290.483	290.352	290.430	290.246	359.434	359.320	359.201	358.931
7	290.563	290.366	290.335	290.246	359.468	359.445	359.249	358.993
8	290.549	290.457	290.439	290.235	359.519	359.534	359.261	359.045
9	290.470	290.362	290.173	290.201	359.345	359.436	359.164	358.820
10	290.461	290.456	290.264	290.283	359.379	359.431	359.218	358.989
11	290.577	290.485	290.423	290.311	359.525	359.479	359.303	359.055
12	290.490	290.339	290.322	290.187	359.464	359.432	359.268	359.048
13	290.455	290.483	290.216	290.237	359.416	359.416	359.283	358.987
14	290.517	290.452	290.372	290.328	359.544	359.605	359.362	359.042
15	290.624	290.504	290.374	290.300	359.518	359.451	359.380	359.054
16	290.552	290.547	290.327	290.222	359.512	359.531	359.417	359.047
17	290.572	290.408	290.349	290.293	359.488	359.410	359.317	359.020
18	290.567	290.547	290.355	290.252	359.542	359.413	359.321	358.962
19	290.527	290.417	290.377	290.213	359.429	359.399	359.274	358.946
20	290.537	290.408	290.286	290.243	359.554	359.422	359.258	358.973
21	290.546	290.421	290.359	290.313	359.642	359.516	359.349	359.067
22	290.484	290.473	290.244	290.214	359.409	359.403	359.245	359.008
23	290.479	290.351	290.281	290.148	359.453	359.421	359.274	358.906
24	290.457	290.429	290.305	290.216	359.496	359.475	359.348	358.979
25	290.552	290.553	290.395	290.315	359.564	359.489	359.378	359.083
26	290.585	290.453	290.342	290.338	359.551	359.498	359.326	359.076
27	290.544	290.447	290.337	290.331	359.435	359.466	359.356	359.103
28	290.577	290.400	290.294	290.319	359.587	359.473	359.245	358.993
29	290.543	290.444	290.398	290.186	359.480	359.462	359.418	359.039
30	290.542	290.448	290.424	290.267	359.573	359.516	359.441	359.104
31	290.561	290.363	290.321	290.274	359.450	359.399	359.308	359.088
32	290.550	290.466	290.379	290.281	359.546	359.545	359.346	359.132
33	290.604	290.508	290.308	290.284	359.534	359.504	359.372	359.075
34	290.533	290.451	290.344	290.231	359.543	359.492	359.363	359.015
35	290.532	290.341	290.319	290.184	359.450	359.400	359.371	359.013
36	290.559	290.449	290.266	290.263	359.571	359.430	359.331	359.027
37	290.575	290.418	290.315	290.332	359.513	359.444	359.300	359.099
38	290.599	290.449	290.337	290.307	359.503	359.574	359.343	359.067
39	290.531	290.470	290.184	290.266	359.465	359.454	359.305	359.066
40	290.537	290.530	290.372	290.178	359.509	359.537	359.325	359.077
.	.	.	.	.	.	.	.	.
.	.	.	.	.	.	.	.	.

Table D.5: Experimental data for the compressor temperature, (samples 41 - 80).

$S\#$ i	T_{0-1} (K)	T_{0-2} (K)	T_{0-3} (K)	T_{0-4} (K)	T_{5-1} (K)	T_{5-2} (K)	T_{5-3} (K)	T_{5-4} (K)
.	.	.	.	.	.	.	.	.
.	.	.	.	.	.	.	.	.
41	290.570	290.482	290.396	290.336	359.590	359.542	359.335	359.082
42	290.580	290.399	290.381	290.266	359.559	359.436	359.306	359.057
43	290.571	290.497	290.398	290.335	359.636	359.526	359.413	359.134
44	290.399	290.349	290.280	290.197	359.449	359.421	359.243	359.114
45	290.556	290.464	290.373	290.280	359.524	359.508	359.350	359.026
46	290.648	290.476	290.408	290.375	359.582	359.526	359.422	359.141
47	290.516	290.522	290.401	290.238	359.555	359.455	359.353	359.132
48	290.572	290.565	290.396	290.279	359.648	359.543	359.383	359.182
49	290.440	290.445	290.291	290.292	359.510	359.562	359.369	359.039
50	290.558	290.546	290.336	290.311	359.578	359.611	359.412	359.190
51	290.563	290.453	290.376	290.206	359.521	359.511	359.331	359.080
52	290.491	290.326	290.211	290.253	359.516	359.482	359.297	359.024
53	290.603	290.455	290.469	290.233	359.548	359.476	359.400	359.138
54	290.502	290.398	290.274	290.248	359.433	359.508	359.387	359.085
55	290.524	290.450	290.229	290.239	359.483	359.511	359.357	359.071
56	290.516	290.504	290.308	290.284	359.439	359.472	359.380	359.070
57	290.533	290.494	290.236	290.167	359.524	359.448	359.330	359.053
58	290.507	290.519	290.499	290.340	359.573	359.518	359.363	359.187
59	290.520	290.347	290.235	290.292	359.398	359.395	359.265	359.028
60	290.526	290.472	290.351	290.264	359.528	359.411	359.303	359.157
61	290.559	290.421	290.415	290.277	359.522	359.560	359.420	359.104
62	290.558	290.456	290.408	290.316	359.487	359.477	359.383	359.122
63	290.647	290.526	290.457	290.307	359.554	359.459	359.428	359.124
64	290.543	290.454	290.276	290.171	359.472	359.405	359.389	359.119
65	290.530	290.382	290.249	290.183	359.463	359.453	359.255	358.998
66	290.634	290.537	290.404	290.425	359.548	359.536	359.462	359.224
67	290.509	290.421	290.396	290.265	359.468	359.422	359.242	359.048
68	290.491	290.414	290.299	290.192	359.510	359.407	359.347	359.048
69	290.511	290.336	290.318	290.171	359.474	359.439	359.246	358.980
70	290.503	290.477	290.327	290.236	359.395	359.469	359.287	359.100
71	290.413	290.447	290.249	290.263	359.463	359.399	359.310	358.996
72	290.510	290.519	290.415	290.292	359.547	359.389	359.351	359.042
73	290.586	290.484	290.333	290.251	359.508	359.489	359.367	359.109
74	290.371	290.291	290.193	290.090	359.353	359.310	359.218	358.909
75	290.543	290.533	290.333	290.287	359.469	359.418	359.396	359.098
76	290.472	290.461	290.329	290.270	359.466	359.407	359.259	359.108
77	290.505	290.514	290.338	290.185	359.450	359.421	359.325	359.078
78	290.568	290.468	290.409	290.336	359.527	359.434	359.270	359.079
79	290.387	290.350	290.266	290.240	359.337	359.397	359.278	358.934
80	290.459	290.440	290.272	290.178	359.443	359.333	359.260	359.026
.	.	.	.	.	.	.	.	.
.	.	.	.	.	.	.	.	.

Table D.6: Experimental data for the compressor temperature, (samples 81 - 100).

$S\#$ i	T_{0-1} (K)	T_{0-2} (K)	T_{0-3} (K)	T_{0-4} (K)	T_{5-1} (K)	T_{5-2} (K)	T_{5-3} (K)	T_{5-4} (K)
.	.	.	.	.	.	.	.	.
.	.	.	.	.	.	.	.	.
81	290.630	290.487	290.386	290.278	359.506	359.436	359.401	359.139
82	290.480	290.386	290.382	290.200	359.460	359.464	359.291	358.984
83	290.373	290.346	290.274	290.206	359.376	359.341	359.258	359.024
84	290.477	290.440	290.319	290.323	359.513	359.464	359.367	359.002
85	290.543	290.429	290.426	290.249	359.461	359.393	359.324	359.116
86	290.568	290.421	290.331	290.154	359.472	359.425	359.312	359.004
87	290.499	290.447	290.222	290.317	359.443	359.408	359.281	359.022
88	290.569	290.483	290.417	290.314	359.419	359.435	359.319	359.174
89	290.482	290.511	290.280	290.249	359.508	359.462	359.347	359.100
90	290.556	290.507	290.378	290.326	359.510	359.426	359.403	359.098
91	290.414	290.374	290.352	290.258	359.387	359.361	359.255	359.060
92	290.529	290.490	290.340	290.282	359.477	359.362	359.373	359.092
93	290.493	290.384	290.295	290.134	359.418	359.328	359.272	359.091
94	290.461	290.354	290.317	290.250	359.393	359.326	359.275	359.043
95	290.430	290.414	290.231	290.299	359.416	359.378	359.228	359.075
96	290.521	290.501	290.322	290.352	359.424	359.502	359.371	359.041
97	290.549	290.453	290.342	290.307	359.505	359.396	359.312	359.087
98	290.509	290.475	290.342	290.276	359.384	359.399	359.315	359.068
99	290.566	290.492	290.348	290.290	359.488	359.444	359.318	358.982
100	290.530	290.364	290.281	290.202	359.366	359.294	359.213	359.015

Appendix E

Sample calculations

In this section sample calculations are given for the design of the orifice plate as well as a single operating point of the compressor. The following constants were used in the calculations.

Universal gas constant of dry air	R	=	$287\,\mathrm{J/kg \cdot K}$
Molar weight of dry air	M	=	$28.96\times10^{-3}\,\mathrm{kg/mol}$
Sutherland temperature for air	S	=	$110.40\,\mathrm{K}$
Reference temperature for air	T_0	=	$297\,\mathrm{K}$
Reference viscosity for air	μ_0	=	$1.71\times10^{-5}\,\mathrm{kg/s \cdot m}$
Viscosity of air at 20 °C	μ	=	$1.80\times10^{-5}\,\mathrm{kg/s \cdot m}$
Specific heat at constant pressure	C_p	=	$1005\,\mathrm{J/kg \cdot K}$
Ratio of specific heats	γ	=	1.4
Temperature probe dynamic correction factor	K	=	0.96
Discharge coefficient parameters	L_1, L_2	=	1,0.47

For the design of the orifice plate a constant specific heat (C_p) value at room temperature was used. For the compressor calculations the specific heat was calculated as a function of temperature. In both cases the air viscosity was calculated using the Sutherland equation.

Specific heat at constant pressure is calculated as a function of temperature (static or total):

$$\begin{aligned} C_p &= (a + bT + cT^2 + dT^3)/M,\ \mathrm{J/kg \cdot K} \\ a &= 28.11 \\ b &= 0.1967\times10^{-2} \\ c &= 0.4082\times10^{-5} \\ d &= -1.966\times10^{-9} \end{aligned} \tag{E.0.1}$$

The viscosity is calculated using the Sutherland equation:

$$\mu \approx \mu_0 \left(\frac{T}{T_0}\right)^{3/2} \left(\frac{T_0 + S}{T + S}\right), \text{ kg/s} \cdot \text{m} \tag{E.0.2}$$

E.1 Orifice plate design

The design of the orifice plate follows from the assumption of the following design parameters:

Maximum supply pressure	p_s	=	1 MPa
Supply air temperature (header pipe)	T_t	=	288 K
Mass flow rate	$\dot{m}$	=	1 kg/s
Design pressure drop	Δp	=	20 kPa
Pipe internal diameter	D	=	0.102 26 m
Pipe internal cross-sectional area	A	=	8.213×10^{-3} m^2

For the given design parameters the air velocity upstream of the primary device (orifice plate) is iteratively calculated. Let the static temperature be equal to the measured supply temperature:

$$T_s = T_t = 288\,\text{K} \tag{E.1.1}$$

Calculate the initial static density:

$$\begin{aligned} \rho_s &= \frac{p_s}{RT_s} = \frac{1\times10^6}{(287)(288)} \\ &= 12.1\,\text{kg/m}^3 \end{aligned} \tag{E.1.2}$$

The initial flow velocity is calculated:

$$\begin{aligned} V &= \frac{\dot{m}}{A\rho_s} = \frac{1}{(8.213\times10^{-3})(12,1)} \\ &= 10.06\,\text{m/s} \end{aligned} \tag{E.1.3}$$

A new static temperature is calculated using the velocity from Eq. E.1.3:

$$\begin{aligned} T_{s\ new} &= T_t - \frac{V^2}{2C_p} = 288 - \frac{10.06}{2(1005)} \\ &= 287.95\,\text{K} \end{aligned} \tag{E.1.4}$$

The static temperature from Eq. E.1.4 is used to calculate a new velocity by repeating Eq. E.1.2 through Eq. E.1.3 until the change in velocity $< 1\times10^{-6}$.

Next the total conditions upstream of the orifice plate are calculated (using isentropic relations) to obtain the design Reynolds number Re_D:

$$\begin{aligned} p_t &= p_s(T_t/T_s)^{\frac{\gamma}{\gamma-1}} \\ &= 1{\times}10^6(287.949/288)^{\frac{1.4}{1.4-1}} \\ &= 1\,000\,612\,\text{Pa} \end{aligned} \tag{E.1.5}$$

$$\begin{aligned} \rho_t &= \rho_s(T_t/T_s)^{\frac{1}{\gamma-1}} \\ &= 12.10(287.95/288)^{\frac{1}{1.4-1}} \\ &= 12.106\,\text{kg/m}^3 \end{aligned} \tag{E.1.6}$$

$$\begin{aligned} \mu_t &\approx \mu_0 \left(\frac{T_t}{T_0}\right)^{3/2} \left(\frac{T_0+S}{T_t+S}\right) \\ &\approx 1.71{\times}10^{-5} \left(\frac{287.95}{288}\right)^{3/2} \left(\frac{287.949+110.04}{288+110.04}\right) \\ &\approx 1.78{\times}10^{-5}\,\text{kg/s}\cdot\text{m} \end{aligned} \tag{E.1.7}$$

$$\begin{aligned} \nu_t &= \mu_t/\rho_t \\ &= 1.78{\times}10^{-5}\ 12.106 \\ &= 1.47{\times}10^{-6}\,\text{m}^2/\text{s} \end{aligned} \tag{E.1.8}$$

The Reynolds number is then calculated as:

$$\begin{aligned} Re_D &= \frac{VD}{\nu_t} = \frac{(10.06)(0.102\,26)}{1.473\,37{\times}10^{-6}} \\ &\approx 7{\times}10^5 \end{aligned} \tag{E.1.9}$$

The diameter ratio is now iteratively calculated by first assuming a value of $\beta = 0.5$ and calculating initial values for the velocity of approach factor (E), expansion factor (ϵ) and flow coefficient (α). The discharge coefficient is calculated from the correlation for orifice plates as per BSI (1981):

$$\begin{aligned} C_d &= 0.5959 + 0.0312\beta^{2.1} - 0.1840\beta^8 + 91.7061\beta^{2.5}Re_D^{-0.75} \\ &\quad + \frac{0.0900L_1\beta^4}{1-\beta^4} - 0.0337\beta^3L_2 \\ &= 0.5959 + 0.0312(0.5)^{2.1} - 0.1840(0.5)^8 \\ &\quad + 91.7061(0.5)^{2.5}(6.9838{\times}10^5)^{-0.75} \\ &\quad + \frac{0.0900(1)(0.5)^4}{1-(0.5)^4} - 0.0337(0.5)^3(0.47) \\ &= 0.61 \end{aligned} \tag{E.1.10}$$

and also

$$\begin{aligned} E &= (1-\beta^4)^{-0.5} = (1-0.5^4)^{-0.5} \\ &= 1.033 \end{aligned} \tag{E.1.11}$$

$$\begin{aligned} \epsilon &= 1 - \left(0.41 + 0.35\beta^4\right) \frac{\Delta p}{\gamma p_{supply}} \\ &= 1 - \left(0.41 + (0.35)(0.5)^4\right) \frac{20{\times}10^3}{(1.4)(1{\times}10^6)} \\ &= 0.994 \end{aligned} \tag{E.1.12}$$

$$\begin{aligned} \alpha &= C_d E = (0.6072)(1.033) \\ &= 0.63 \end{aligned} \tag{E.1.13}$$

A new β is calculated from:

$$\begin{aligned} \beta &= \frac{V^2 \rho_s}{\sqrt{\alpha^2(2\Delta p)}} = \frac{(10.06)^2(12.1)}{\sqrt{(0.63)^2(2(20{\times}10^3))}} \\ &= 0.53 \end{aligned} \tag{E.1.14}$$

The final value for the orifice plate diameter ratio is calculated as:

$$\beta = 0.53$$

E.2 Experimental data sample calculations

In this section a sample calculation is given at an operating condition of 80 000 rpm and $\dot{m} = 0.190\,\text{kg/s}$. The sample data is obtained from the tables given in Appendix D. The mass flow is calculated from the bellmouth calibration and measured differential pressure across the bellmouth. The values in the sample calculations correspond to the average values of all measured data at specific operating points.

Dimensions of the bellmouth:

Inlet diameter (suction side)	D	$\gg$	d
Outlet diameter (discharge side)	d	$=$	$77.3\times10^{-3}\,\text{m}$

Dimensions for the small diameter pipe at the compressor outlet where the static pressure measurements are calculated:

Pipe length	ΔL_4	$=$	$0.31\,\text{m}$
Pipe internal diameter	d_4	$=$	$40.9\times10^{-3}\,\text{m}$
Pipe internal cross-sectional area	A_4	$=$	$1.31\times10^{-3}\,\text{m}^2$
Pipe internal surface roughness	ϵ_4	$=$	$0.046\times10^{-3}\,\text{m}$

From the experimental data the following is averaged quantities were obtained:

Ambient pressure	p_{amb}	$=$	$99\,960\,\text{Pa}$
Ambient temperature	T_{amb}	$=$	$289.68\,\text{K}$
Bellmouth differential pressure	Δp	$=$	$691\,\text{Pa}$
Compressor outlet static pressure	p_{s4}	$=$	$171\,632\,\text{Pa}$
Compressor inlet total temperature	T_{t1}	$=$	$289.68\,\text{K}$
Compressor outlet probe temperature	T_{p5}	$=$	$358.94\,\text{K}$

The ambient air density is calculated from:

$$\begin{aligned}\rho_{amb} &= \frac{p_{amb}}{RT_{amb}} \\ &= \frac{99\,960}{(0.278)(289.68)} \quad = 1.20\,\text{kg/m}^3\end{aligned} \tag{E.2.1}$$

The bellmouth velocity, V_{bm} and corresponding Reynolds number, Re_{bm} is calculated:

$$\begin{aligned} V_{bm} &\approx \left[\frac{2\Delta p}{\rho_{amb}(1-D^4d^4)}\right]^{1/2} \\ &\approx \left[\frac{2(691)}{(1.202)(1)}\right]^{1/2} \\ &\approx 33.9\,\mathrm{m/s} \end{aligned} \tag{E.2.2}$$

$$\begin{aligned} Re_{bm} &= \frac{V_{bm}\rho_{bm}d}{\mu} \\ &= \frac{(33.9)(1.202)(0.0773)}{1.8\times10^{-5}} \\ &= 175\,100 \end{aligned} \tag{E.2.3}$$

The coefficient of discharge is calculated from the bellmouth calibration using equation A.2.3:

$$\begin{aligned} C_d &= e^{\frac{-1500}{Re_{bm}}} \\ &= e^{\frac{-1500}{175\,100}} \\ &= 0.99 \end{aligned} \tag{E.2.4}$$

The mass flow is then calculated from Eq. 3.3.2:

$$\begin{aligned} \dot{m} &= C_dE\epsilon\frac{\pi}{4}d^2\sqrt{2\Delta p\rho_1} \\ &= (0.99)(1)(1)(\pi/4)(0.0773^2)\sqrt{2(691)(1.20)} \\ &= 0.19\,\mathrm{kg/s} \end{aligned} \tag{E.2.5}$$

where $E = 1$ (velocity of approach factor) and $\epsilon = 1$ (expansibility factor)

Now the total-to-static pressure ratio and total-to-total efficiency is calculated. Let the initial static temperature be approximated by the measured probe temperature:

$$\begin{aligned} T_{s4} &= T_{p5} \\ &= 358.94\,\mathrm{K} \end{aligned} \tag{E.2.6}$$

Calculate the initial static conditions at the pressure measurement station:

$$\begin{aligned} C_{p,4} &= \left(a + bT_{s4} + cT_{s4}^2 + dT_{s4}^3\right)/M \\ &= \frac{a + b(358.94) + c(358.94)^2 + d(358.94)^3}{28.96\times10^{-3}} \\ &= 1009.70\ \ \mathrm{J/kg\cdot K} \end{aligned} \tag{E.2.7}$$

$$\begin{aligned}\gamma_4 &= C_{p,s4}/(C_{p,s4} - R) \\ &= 1009.70/(1009.70 - 287) \\ &= 1.39\end{aligned} \tag{E.2.8}$$

$$\begin{aligned}\rho_4 &= p_{s4}/(RT_{s4}) \\ &= 171\,632/((287)(358.94) \\ &= 1.67 \ \text{kg/m}^3\end{aligned} \tag{E.2.9}$$

Compute the absolute gas velocity:

$$\begin{aligned}c_4 &= \dot{m}/(\rho_{s4}A_4) \\ &= 0.19/((1.67)(1.31\times10^{-3}) \\ &= 87.07\,\text{m/s}\end{aligned} \tag{E.2.10}$$

Compute the Mach number:

$$\begin{aligned}Ma_4 &= c_4/\sqrt{\gamma_4 T_{s4} R} \\ &= 87.07/\sqrt{(1.39)(358.94)(287)} \\ &= 0.23\end{aligned} \tag{E.2.11}$$

Compute the total temperature using Eq. 3.3.1:

$$\begin{aligned}T_{t4} &= T_{p5} + \frac{(1-K)c_4^2}{2C_{p,4}} \\ &= 358.94 + \frac{(1-0.96)(87.067)^2}{2(1009.70)} \\ &= 359.09\,\text{K}\end{aligned} \tag{E.2.12}$$

Compute the new static temperature using Eq. 3.5.6:

$$\begin{aligned}T_{s4} &= \frac{T_{t4}}{1 + \frac{(\gamma_4 - 1)M_4^2}{2}} \\ &= \frac{359,09}{1 + \frac{(1{,}39-1)(0.23)^2}{2}} \\ &= 355.36\,\text{K}\end{aligned} \tag{E.2.13}$$

Now the static temperatures from Eq. E.2.6 and E.2.13 are compared. If the difference $|\Delta T_{s4}| > 1\times10^{-6}\,\text{K}$, the static temperature from Eq. E.2.13 is substituted back into Eq. E.2.7:

$$\begin{aligned}\Delta T_{s4} &= |T_{s4} - T_{s4\ new}| \\ &= |358.94 - 355.36| \\ &= 3.58\,\mathrm{K} \gg 1{\times}10^{-6}\,\mathrm{K}\end{aligned} \tag{E.2.14}$$

Equations. E.2.6 through E.2.14 are repeated until $|\Delta T_{s4}| < 1.10^{-6}$ and so that the total pressure is calculated as:

$$\begin{aligned}p_{t4} &= p_{s4}\left[1 + \frac{(\gamma_4 - 1)M_4^2}{2}\right]^{\frac{\gamma_4}{\gamma_4 - 1}} \\ &= 171\,632\left[1 + \frac{(1.39 - 1)(0.23)^2}{2}\right]^{\frac{1.39}{1.39-1}} \\ &= 177\,956\,\mathrm{Pa}\end{aligned} \tag{E.2.15}$$

The static and total conditions were calculated as:

$$\begin{aligned}T_{4s} &= 355.41\,\mathrm{K} \\ C_{p4s} &= 1009.20\,\mathrm{J/kg{\cdot}K} \\ \gamma_4 &= 1.39 \\ \rho_{4s} &= 1.68\,\mathrm{kg/m^3} \\ c_4 &= 86.20\,\mathrm{m/s} \\ Ma_4 &= 0.23 \\ T_{4t} &= 359.09\,\mathrm{K} \\ p_{4t} &= 177\,956\,\mathrm{Pa}\end{aligned}$$

After the total conditions have been calculated at the pressure measurement station of the compressor outlet, the total conditions at the outlet plane of the volute exit cone are calculated from compressible pipe flow theory which includes friction. The Mach number at the volute exit of the measurement station can be determined from:

$$\frac{\bar{f}L^*}{d} = \frac{1 - M^2}{\gamma M^2} + \frac{\gamma + 1}{2\gamma}\ln\frac{(\gamma + 1)M^2}{2 + (\gamma - 1)M^2} \tag{E.2.16}$$

$$\bar{f}\frac{\Delta L}{d} = \left(\frac{\bar{f}L^*}{d}\right)_{vo} - \left(\frac{\bar{f}L^*}{d}\right)_{pm} \tag{E.2.17}$$

where subscripts vo and pm denote the planes at volute outlet and pressure measuring station respectively. For known conditions (Ma_4 and γ_4) the right

hand side of Eq. E.2.16 is calculated at the pressure measurement station:

$$\begin{aligned}\left(\frac{\bar{f}L^*}{d}\right)_{pm} &= \frac{1-(0.23)^2}{(1.39)(0.23)^2}+\frac{(1.397+1)}{2(1.39)} \\ &\quad\times \ln\frac{(1.39+1)(0.23)^2}{2+(1.39-1)(0.23)^2} \\ &= 10.63\end{aligned} \tag{E.2.18}$$

The fluid viscosity is dependent on fluid temperature and calculated from Eq. E.0.2:

$$\begin{aligned}\mu_4 &\approx \mu_0\left(\frac{T_{4s}}{T_0}\right)^{3/2}\left(\frac{T_0+S}{T_{4s}+S}\right) \\ &\approx 1.71{\times}10^{-5}\left(\frac{359.09}{293}\right)^{3/2}\left(\frac{293+110.4}{359.09+110.4}\right) \\ &\approx 2.12{\times}10^{-5}\,\mathrm{kg/ms}\end{aligned} \tag{E.2.19}$$

The friction factor on the left hand side of Eq. E.2.17 is dependent on the average fluid velocity and iteratively calculated. Let c_4 from the measurement plane be taken as the initial average fluid velocity, $\bar{c}_4 = c_4$. The Reynolds number is calculated:

$$\begin{aligned}Re_{d_4} &= \frac{\rho_4\bar{c}_4 d_4}{\mu_4} \\ &= \frac{(1.68)(86.20)(40.9{\times}10^{-3})}{2.13{\times}10^{-5}} \\ &= 2.81{\times}10^5\end{aligned} \tag{E.2.20}$$

The friction factor is calculated using the explicit formula by Halaand and rearranged to give:

$$\begin{aligned}f &= \left[-1.8\log\left(\frac{6.9}{Re_{d_4}}+\left(\frac{\epsilon_4/d_4}{3.7}\right)^{1.11}\right)\right]^{-2} \\ &= \left[-1.8\log\left(\frac{6.9}{2.79{\times}10^5}+\left(\frac{1.13{\times}10^{-3}}{3.7}\right)^{1.11}\right)\right]^{-2} \\ &= 2.11{\times}10^{-2}\end{aligned} \tag{E.2.21}$$

For the known pipe geometry (ΔL and d_4), the right hand side of Eq. E.2.17 is calculated:

$$\frac{\bar{f}\Delta L}{d} = \frac{(0.021)(0.305)}{0.0409} = 0.157 \tag{E.2.22}$$

Rearranging Eq. E.2.17 and solving for the volute outlet:

$$\left(\frac{\bar{f}L^*}{d}\right)_{vo} = \bar{f}\frac{\Delta L}{D} + \left(\frac{\bar{f}L^*}{d}\right)_{pm} = 10.782 \tag{E.2.23}$$

Now the Mach number at the volute outlet plane can be solved by substituting the result from Eq. E.2.23 into Eq. E.2.16. The Mach number is solved iteratively using the method of bisection. It is expected that the Mach number should not exceed 0.5 and therefore the upper limit is chosen to be $M_{up} = 0.5$. The lower limit is set to $M_{low} = 1\times10^{-6}$. Using the midpoint, $M_{mid} = (M_{up} + M_{low})/2$ as an initial value for the Mach number, the right side of Eq. E.2.16 is solved. The iterative process concludes once the difference between the left and right side of Eq. E.2.16 $< 1\times10^{-6}$. At this point the current midpoint value is taken to be the Mach number at the volute exit plane:

$$M_{vo} = M_{mid} = 0.227 \tag{E.2.24}$$

The absolute velocity at the volute outlet is calculated from compressible duct flow critical ratios.

$$\frac{c}{c^*} = \frac{1}{M}\left[\frac{2+(\gamma-1)M^2}{\gamma+1}\right]^{1/2} \tag{E.2.25}$$

$$\begin{aligned} c_{vo} &= c_4\frac{c_{vo}/c^*}{c_4/c^*} = 86.20\frac{0.247}{0.249} \\ &= 85.69\,\mathrm{m/s} \end{aligned} \tag{E.2.26}$$

Equations E.2.20 through E.2.26 are repeated until an error $< 1\times10^{-6}\,\mathrm{m/s}$ is reached. Once convergence has been achieved the total and static conditions at the plane of the volute outlet is calculated from compressible duct flow critical ratios. These may be referenced in White (2005). The final static and total conditions were calculated as:

$$\begin{aligned} T_{s,vo} &= 355.45\,\mathrm{K} \\ p_{s,vo} &= 172\,677\,\mathrm{Pa} \\ \rho_{s,vo} &= 1.69\,\mathrm{kg/m^3} \\ c_{vo} &= 85.69\,\mathrm{m/s} \\ Ma_{vo} &= 0.23 \\ T_{t,vo} &= 359\,\mathrm{K} \\ p_{t,vo} &= 178\,971\,\mathrm{Pa} \end{aligned}$$

The total-to-static pressure ratio and total-to-total efficiency for the compressor is now calculated:

$$PR_{t-s} = \frac{p_{s,vo}}{p_{t1}} = \frac{172\,677}{99\,960} = 1.73 \tag{E.2.27}$$

$$\begin{aligned} \eta_{t-t} &= \left[\left(\frac{p_{t,vo}}{p_{t1}}\right)^{(\gamma-1)/\gamma} - 1\right]\left[\frac{T_{t1}}{T_{t,vo} - T_{t1}}\right] \\ &= \left[\left(\frac{17\,897}{99\,960}\right)^{(1.39-1)/1.39} - 1\right]\left[\frac{289.68}{359 - 289.68}\right] \\ &= 0.75 \end{aligned} \tag{E.2.28}$$

Appendix F

Operating procedure

The following set of instructions were followed every time a test run was to be completed unless otherwise instructed. It was important to strictly adhere to this checklist in order to prevent any possible harm to persons operating the test bench and/or damage to any of the components of the test bench.

Test Briefing

1. Ensure that ear protection is worn for the duration of the test procedure.
2. Check the integrity of all pressure connections and tubing. (Only needed to be checked once for the first set of test runs of the day).
3. Check all data and power connectivity of the instrumentation.
4. Switch on power supply to the DAQ and lubrication system.
5. Check that telemetry readings are correct.
6. Ensure all valves upstream of the turbine are closed. (Flow control butterfly valve, secondary safety ball valve, primary header ball valve.
7. Ensure there is no or possible chance of blockage up- and downstream of the compressor.
8. Open throttle valve completely downstream of the compressor.
9. Set the oil heater thermostat to 65°C for preheating.
10. Ensure that the bypass valve is open. (Oil will bypass the turbocharger)
11. Switch on the lubrication system when the oil temperature has reached 65°C at the inlet measurement point.
12. Allow the oil to circulate and for the temperature to stabilise at 65°C.

13. Shut the oil bypass valve (Oil is now circulating through the turbocharger).
14. Set the oil pressure to 600 kPa on the lubrication system panel (500 kPa at the turbocharger).
15. Open the primary valve.
16. Open the secondary valve.
17. Commence start-up procedure.
18. Idle turbocharger for 2 min at 40 $krpm$, then 1 min at 60 $krpm$.
19. Commence with procedure for test run.

Test Debriefing

1. Commence shut-down procedure.
2. Idle turbocharger for 4 min at 20 $krpm$.
3. Shut primary valve.
4. Allow remaining air to be discharged through the turbocharger.
5. Shut secondary and flow control valve.
6. Open throttle valve completely downstream of compressor.
7. Switch off thermostat.
8. Reduce oil pressure to 200 kPa on the lubrication system panel.
9. Open oil bypass valve.
10. Switch off lubrication system.
11. Switch off the DAQ and oil pump power supply (Only necessary after the last test of the day).

Appendix G

Volute modelling

G.1 CAD modelling

Figures G.1 to G.6 give a graphical representation of the steps that were followed in creating the solid model of the volute.

Figure G.1: K27 volute.

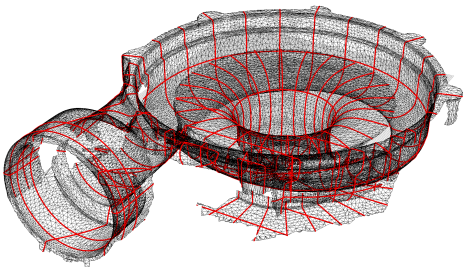

Figure G.2: Volute point cloud and cross-sections model from STL scan.

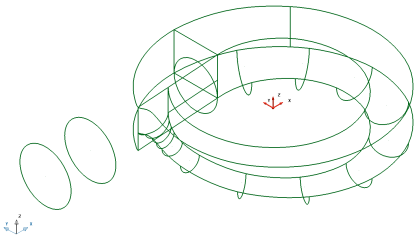

Figure G.3: Volute wire-frame model from PowerSHAPE®.

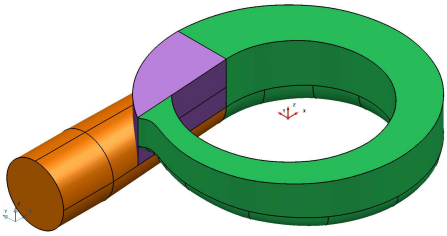

Figure G.4: Volute surface model from PowerSHAPE®.

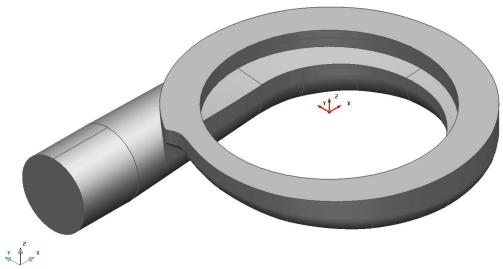

Figure G.5: Volute solid model from Inventor Professional®.

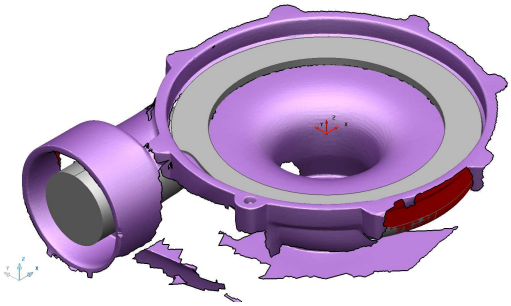

Figure G.6: Comparison of solid and point cloud model.

G.2 Domain faceting

Table G.1: Faceting parameters

Minimum length	0.155×10^{-3} m
Maximum length	0.155 m
Curve chordal tolerance	1×10^{-3} m
Surface plane tolerance	1×10^{-3} m
Curve resolution	2°
Surface resolution	2°

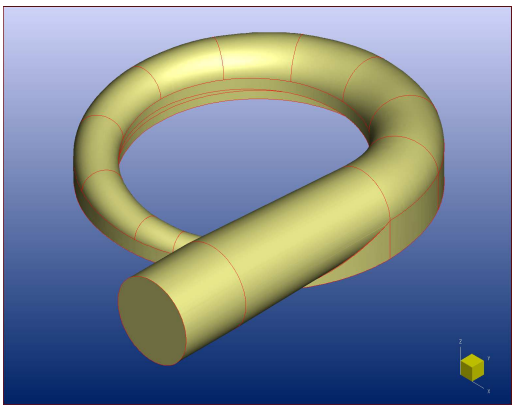

Figure G.7: Volute discretised domain (complex).

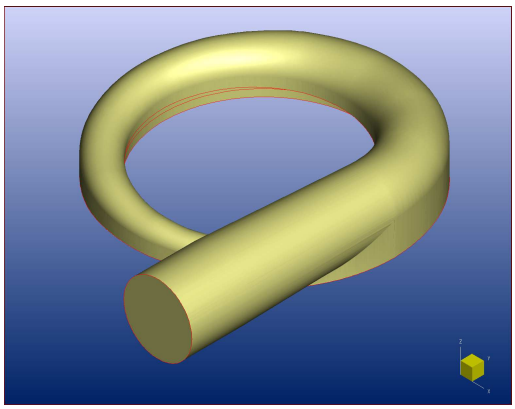

Figure G.8: Volute discretised domain (simplified).

G.3 Volute mesh

Figures G.9 to G.12 give a graphical representation of the steps that were followed in creating the solid model of the volute.

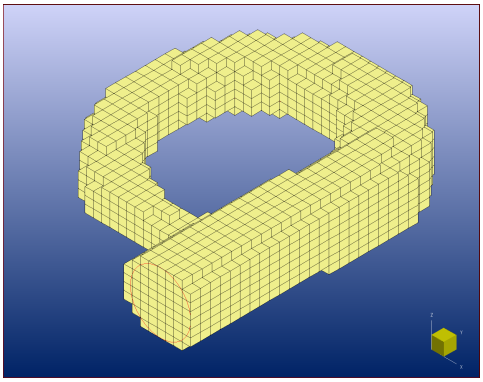

Figure G.9: Volute initial mesh.

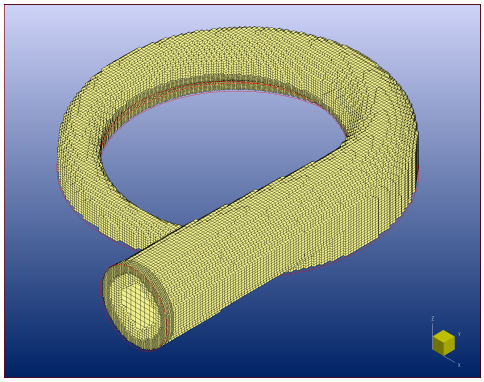

Figure G.10: Volute adapted mesh.

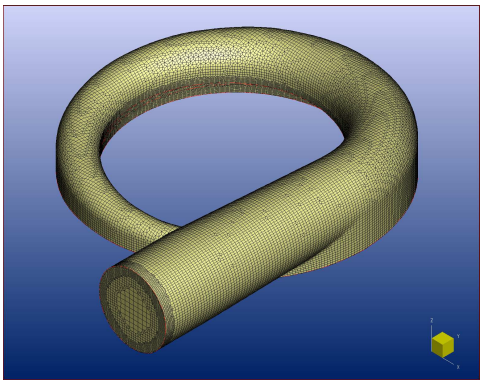

Figure G.11: Volute optimized mesh.

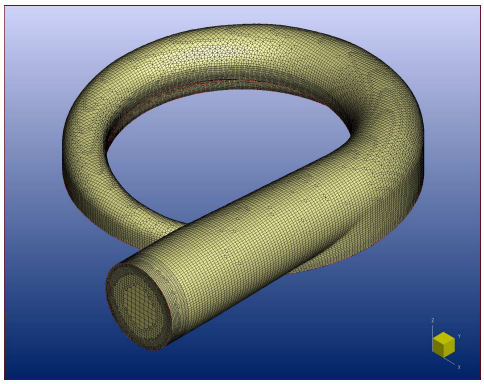

Figure G.12: Volute mesh with viscous layers inserted.

List of References

ASME (1997). ASME PTC 10-1997 Performance Test Code on Compressors and Exhausters. Tech. Rep., New York.

ASME (2005). ASME PTC 22-2005 Gas Turbines Performance Test Codes. Tech. Rep., New York.

Aungier, R.H. (2000). *Centrifugal Compressors A Strategy for Aerodynamic Design and Analysis*. ASME Press.

Aus der Wiesche, S. (2012 June). A Mobile Test Rig For Micro Gas Turbines Based on a Thermal Power Measurement Approach. In: *Proceedings of ASME Turbo Expo 2012*, pp. 1–10. Copenhagen.

Autodesk (2012). Inventor Professional - Student. Build 190, Release:2012 SP1, 64-Bit Edition.
Available at: `http://usa.autodesk.com/autodesk-inventor/`

Benedict, R.P. (1977). *Fundamentals of Temperature , Pressure and Flow Measurements*. 2nd edn. John Wiley & Sons, Inc., Philadelphia.

Benini, E. and Giacometti, S. (2007). Design, manufacturing and operation of a small turbojet-engine for research purposes. *Applied Energy*, vol. 84, no. 11, pp. 1102–1116.

Blazek, J. (2001). *Computational Fluid Dynamics: Principles and Applications*. 1st edn. Elsevier, Baden-Daettwil.

Brun, K. and Nored, M. (2006 August). Guideline For Field Testing Of Gas Turbine And Centrifugal Compressor Performance. Guideline Release 2.0.

BSI (1981). BS 1042: Section 1.1 : 1981 Measurement of fluid flow in closed conduits. Tech. Rep., British Standards Institution.

Cengel, Y.A. and Boles, M.A. (2006). *Thermodynamics: An Engineering Approach*. 5th edn. McGraw HIll.

Chinese Academy of Sciences (2012). Laboratory of Propulsion and Power. viewded 11 July 2012.
Available at: `http://english.iet.cas.cn/research/LaboratoryofPropulsionandPower/`

De Wet, A., Von Backstrom, T.W. and Van der Spuy, S. (2010). The CFD Simulation of a Centrifugal Compressor. In: *Seventh South African Conference on Computational and Applied Mechanics*, pp. 1–16. Pretoria.

Delcam (2012). PowerSHAPE. Version 2012.
Available at: `http://www.powershape.com/`

Dixon, S. (2005). *Fluid Mechanics and Thermodynamics of Turbomachinery.* 5th edn. Elsevier.

Figliola, R.S. and Beasley, D.E. (2006). *Theory and Design for Mechanical Measurements.* 4th edn. John Wiley & Sons, Inc.

Garrett Turbochargers (2012*a*). Compressor Maps | Turbobygarrett. 2012/09/18.
Available at: `http://www.turbobygarrett.com/turbobygarrett/compressor_maps`

Garrett Turbochargers (2012*b*). White Paper No. 2: Burst & Containment: Ensuring Turbocharger Safety. White Paper.
Available at: `http://www.turbobygarrett.com/turbobygarrett/`

Hagelstein, D., Hillewaert, K., Engeda, A., Keiper, R. and Rautenberg, M. (2000). Experimental and Numerical Investigation of the Flow in a Centrifugal Compressor Volute. *Journal of Turbomachinery*, vol. 122, no. January, pp. 22–31.

Japikse, D. and Baines, N. (1994). *Introduction to Turbomachinery.* Concpets NREC.

Kim, S., Park, J. and Baek, J. (2011 December). A numerical study of the effects of blade angle distribution on the performance and loss generation of centrifugal compressor impellers. In: *Proceedings of the Institution of Mechanical Engineers, Part A: Journal of Power and Energy*, vol. 226, pp. 208–217. Sage.

Krige, D. (2012). *Performance Evaluation of a Micro Gas Turbine?s Centrifugal Compressor Diffuser.* Master of Science thesis, Dept. of Mechanical Engieneering, University of Stellenbosch, Stellenbosch.

Lim, K.T., Yoon, S.Y., Goyne, C.P., Lin, Z. and Allaire, P.E. (2011). Design and Characterization of a Centrifugal Compressor Surge Test Rig. *International Journal of Rotating Machinery*, vol. 2011, pp. 1–8.

Ling, J., Wong, K.C. and Armfield, S. (2007). Numerical Investigation of a Small Gas Turbine Compressor. In: *16th Australasian Fluid Mechanics Conference*, December, pp. 961–966. Gold Coast, Australia.

Lobik, D.P. (1995 September). *Unamanned Aerial Vehicles: A Study of Gas Turbine Application.* Master of Science thesis, Dept. of Aeronautical Engineering, Naval Post Graduate School, Monterey, California.

National Instruments (2010 Septembe*a*). *LabVIEW FPGA Course Manual.* National Instruments, september 2010 edition edn.

National Instruments (2010 October*b*). *LabVIEW Real-Time 1 Course Manual*. National Instruments, october 2010 edition edn.

Nieuwoudt, A. (1987 December). Turboaanjaertoetsbank. Final year project, Dept. of Mechanical Engineering, University of Stellenbosch.

NUMECA International (2010 March*a*). *User Manual - AutoGrid5 v8 - Automated Grid Genrator for Turbomachinery*. NUMECA International, march 2010 edn.

NUMECA International (2010 May*b*). *User Manual - FINE/Turbo v8.7 - Flow Integrated Environment*. NUMECA International, may 2010 edn.

NUMECA International (2011 August). *User Manual - FINE/Open v2.11 - Flow Integrated Environment*. NUMECA International, august 2011 edn.

NUMECA Software Support Group (2012). email, n.d., support@numeca.de.

Sayers, A. (). *Hydraulic and Compressible Flow Turbomachines*. Cape Town.

Smith, G. (2010 February). Specifications for a low cost test rig for improving the performance of micro gas turbine components.

Smith, S.C. (1985 February). Airflow Calibratlon of a Bellmouth Inlet for Measurement of Compressor Airflow in Turbine Powered Propulsion Simulators. Tech. Rep., Ames Research Centre, NASA, Moffett Field, California.

Snedden, G. (2010). email, 19 January 2010, gsnedden@csir.co.za.

Sonntag, R., Borgnakke, C. and Van Wylen, G. (1998). *Fundamentals of Thermodynamics*. 5th edn. John Wiley & Sons, Inc.

Soong, W.L., Kliman, G.B., Johnson, R.N., White, R.A. and Miller, J.E. (2000). Novel High-Speed Induction Motor for a Commercial Centrifugal Compressor. *IEEE Transactions of Industry Applications*, vol. 36, no. 3, pp. 706–713.

Southwest Research Institute (2012). Turbocharger Test Facility. 18 September 2012.
Available at: `www.swri.org/3pubs/brochure/d03/Turbo/turbo.htm`

TQC Automation & Test Solutions (2012). Turbocharger Test Equipment. 18 September 2012.
Available at: `www.tqc.co.uk/testmachines/turbocharger_testing.htm`

Turbo Exchange (2012). Professional comunication.
Available at: `http://www.turboexchange.co.za/index.php`

Van den Braembussche, R.A. (2006). Flow and Loss Mechanisms in Volutes of Centrifugal Pumps. *Design and Analysis of High Speed Pumps*, , no. 12, pp. 12–1 – 12–26.

Van der Merwe, B. (2012 December). *Design of a Centrifugal Compressor Impeller for Micro Gas Turbine Application.* Master of Science thesis, University of Stellenbosch, Stellenbosch.

Versteeg, H. and Malalasekera, W. (1995). *An introduction to Computational Fluid Dynamics: The Finite Volume Method.* 1st edn. Longman Scientific & Technical.

Vick, M.J., Heyes, A. and Pullen, K. (2009). Design Overview of a Three-Kilowatt Recuperated Ceramic Turboshaft Engine. In: *Proceedings of ASME Turbo Expo 2009: Power for Land, Sea and Air*, pp. 1–14. American Society of Mechanical Engineers.

White, F.M. (2005). *Fluid Mechanics.* 5th edn. McGraw HIll.

Zangeneh, M., Schleer, M., Ploger, F., Hong, S., Roduner, C., Ribi, B. and Abhari, R. (2004). Investigation of an Inversely Designed Centrifugal Compressor Stage - Part I : Design and Numerical Verification. *Journal of Turbomachinery*, vol. 126, no. January, pp. 73–81.